Applications of radiogenic and transition metal isotopes to the study of metallic mineral deposits

Massimo Chiaradia[a], **Ryan Mathur**[b], **Torsten Vennemann**[c], **and Adam Simon**[d], [a]Department of Earth Sciences, University of Geneva, Geneva, Switzerland; [b]Juniata College, Huntingdon, PA, United States; [c]Stable Isotope Laboratory, University of Lausanne, Lausanne, Switzerland; [d]Earth & Environmental Sciences, University of Michigan, Ann Arbor, MI, United States

This chapter has been reviewed by the section editor Matthew Kohn.

Abstract

This chapter discusses how radiogenic and stable isotopes can be used in the study of metallic mineral deposits. Although the chapter is mostly focused on the radiogenic (Pb, Os) and heavy stable (Fe, Cu, Zn) isotopes of metallic elements, we complement the discussion highlighting also the power of stable isotopes of light elements, which are major to significant components of hydrothermal fluids and rocks (e.g., H, B, C, N, O, S), as well as of radiogenic isotopes of elements (Sr, Nd, Hf) that are useful in tracing fluid/magma sources and their interaction with the host rocks.

https://doi.org/10.1016/B978-0-323-99762-1.00010-3

In the first part of this chapter we discuss general aspects of isotopes clarifying the differences between stable non-radiogenic and stable radiogenic isotopes and, consequently, their different applicability to metallogenic studies. Due to their properties, stable non-radiogenic isotopes record mass-dependent fractionation that occur in many reactions associated with the formation of mineral deposits. Mass-dependent fractionation of stable non-radiogenic isotopes occurs both under equilibrium and non-equilibrium (kinetic) conditions of the reactions leading to ore mineral deposition and is controlled by various physico-chemical parameters, like, among the principal ones, temperature, oxygen fugacity, and biological activity. Therefore, stable non-radiogenic isotopes can inform us about the physico-chemical and, eventually, biological processes that control ore mineral deposition and also on the sources of some metals (e.g., transition metal isotopes of elements like Fe, Cu, Zn) or of the fluids (e.g., H, C, O, N, S isotopes) and even of metal ligands (e.g., S, Cl). We conclude the first part of the chapter providing some hints on the strategy of sampling and on the instrumentation related to isotopic studies.

In the second part we discuss radioactive-radiogenic isotope systems and their applications in metallogenic studies of metallic mineral deposits. Stable radiogenic isotopes are characterized by relative variations that are controlled, in each geological system, by the addition of a radiogenic component of an isotope, derived from the decay of a radioactive parent, to the same radiogenic isotope already present in the Earth since its formation ~4.55 Gyr ago. This relative variation is usually expressed as the ratio of a radiogenic isotope of an element to a non-radiogenic isotope of the same element. The ratio of these two isotopes has increased since the Earth formation and the magnitude of its variations depends on the radioactive/radiogenic isotope ratios in different geological systems and on the time elapsed since the system has formed. The Earth is ~4.55 Gyr old and has evolved from an initially homogeneous isotopic composition to reservoirs (e.g., mantle, crust) and crustal rocks with very variable radioactive/radiogenic isotope ratios due to magmatic, metamorphic, weathering, atmospheric and biologic processes, among others. This has resulted in extremely large variations of radiogenic isotopes in rocks and reservoirs of the Earth which can track various geological processes. In ore geology, stable radiogenic isotopes are best suited for tracing metal (e.g., Pb, Os) sources from different rocks and reservoirs (e.g., mantle, upper crust, lower crust), fluid-rock interactions (i.e., the hydrothermal plumbing system), or magma-host rock interactions (e.g., host rock assimilation by magmas associated with magmatic-hydrothermal deposits).

Radioactive-radiogenic isotope systems allow us to determine also absolute ages of suitable minerals that are found in mineral deposits. This is an essential information in metallogeny that allows us to link the formation of a mineral deposit to a specific geological process and/or to specific periods of the Earth's history. We discuss various dating methods that are extensively applied to date mineral deposits. These methods can be subdivided into those that allow a direct dating of ore minerals (e.g., Re—Os dating of molybdenite, U—Pb dating of cassiterite) and those that allow dating of minerals that are demonstrably related with the mineralization (e.g., U—Pb dating of zircon from magmatic rocks associated with magmatic-hydrothermal deposits; Ar/Ar dating of K-bearing minerals resulting from alteration associated with various types of mineral deposits). We discuss pros and cons of using these various methods and also mention methods that are less used (because potentially less accurate and precise), but sometimes represent the only possibility to provide an age to deposit types that are notoriously difficult to date (e.g., MVT and Carlin-type deposits).

We highlight the power of both stable radiogenic and non-radiogenic isotopes in unravelling the genesis of metallic mineral deposits through a series of conceptual and real examples applied to a broad range of mineral deposit types such as porphyry systems (i.e., porphyry deposits, high- and intermediate-sulfidation epithermal deposits, skarn, carbonate replacement deposits, sediment-hosted Au deposits), low-sulfidation epithermal deposits, IOCG deposits, ortho-magmatic deposits, volcanic-hosted massive sulfide deposits (VHMS), sediment-hosted deposits (stratiform copper, MVT), and supergene deposits.

In the third part of the chapter, we discuss the use of transition metal stable non-radiogenic isotopes to mineral deposits. Although in its infancy, the application of transition metal isotopes to mineral deposit investigation is quickly growing because these isotopes allow us to address different aspects of the formation of mineral deposits compared to radiogenic isotopes. In particular, isotopes of transition metals (like stable isotopes of light elements) undergo mass-dependent fractionation processes that may be associated with different types of equilibrium and non-equilibrium chemical, physical and biological reactions occurring during the formation of mineral deposits. We focus on the applications of the isotopes of Cu, Fe and Zn to various deposit types, because isotopes of these transition metals are those that have been most extensively used in mineral deposit studies. Mass-independent fractionation may also occur for isotopes of some elements and could be a developing field that has not yet been extensively explored in the study of mineral deposits.

Keywords

Copper; Iron; Lead; Light stable isotopes; Mineral deposits; Osmium; Oxygen; Radiogenic isotopes; Sulfur; Transition metal stable isotopes; Zinc

Key points

- We discuss the uses of stable radiogenic (Pb, Os) and non-radiogenic (Fe, Cu, Zn) isotopes of metals to the study of metallic mineral deposits.
- Stable radiogenic isotope variations depend on time and on the relative abundances of the parent radioactive isotope and the daughter radiogenic stable isotope.

- Stable radiogenic isotopes are ideally suited to track sources of metals (Pb, Os) in mineral deposits and to derive information on the hydrothermal plumbing systems.
- In conjunction with their radioactive parents, stable radiogenic isotopes allow accurate and precise absolute dating of metallic mineral deposits.
- Stable non-radiogenic isotopes of transition elements (Fe, Cu, Zn), like light stable isotopes (H, B, C, N, O, S), record mass-dependent fractionation that occurs in many reactions associated with the formation of mineral deposits.
- Stable non-radiogenic isotopes of transition metals (Fe, Cu, Zn), like light stable isotopes (H, B, C, N, O, S), are ideally suited to track physico-chemical processes that lead to mineralization (e.g., fO_2 changes), low-temperature ore processes (Fe, Cu, Zn), and to some extent the sources of metals (e.g., Fe, Cu, Zn).

Introduction

Economic metallic mineral deposits are anomalous accumulations of metals which have been concentrated above average rock contents, either in their native form or, more commonly, in other mineralogical forms that make them exploitable (e.g., Skinner, 1997). Such metal concentration can be due to purely magmatic processes (e.g., orthomagmatic Ni—Co—PGE deposits associated with mafic magmatic complexes), to aqueous fluids that leach, carry and precipitate metals in various geological environments (magmatic-hydrothermal, metamorphic, sedimentary, supergene), to hydrologic or eolian concentration at the Earth's surface of certain ore minerals previously formed (placer deposits), and to weathering processes that remove selectively elements of a rock resulting in the residual concentration of metals (residual deposits; e.g., laterite, bauxite). In most mineral deposit types, metals are precipitated from aqueous solutions under a wide range of physico-chemical conditions (e.g., Seward and Barnes, 1997). These aqueous solutions may originate from the same source as the metal of interest in the mineral deposit, for example via the exsolution from a magma, or may be modified seawater, meteoric or connate water, basinal brines, metamorphic fluids, or even a mixture thereof, sometimes with a distinct origin compared to the economic metals of interest in the mineral deposit (e.g., Giggenbach, 1997; Scott, 1997; McKibben and Hardie, 1997). Precipitation of metals from these aqueous solutions is accompanied by exchange between fluid and rocks, resulting in distinct alteration patterns of the host rock adjacent to the fluid path (e.g., Reed, 1997; see also Steele-MacInnis, this volume and Lecumberri-Sanchez and Steele-MacInnins, this volume). This overall process results in the precipitation of metal-bearing ore minerals, e.g., sulfides and/or oxides, but also of the so-called gangue minerals, e.g., carbonates, sulfates, or silicates that do not contain economic elements.

Large-scale geologic processes are required as ultimate drivers for the formation of mineral deposits and include magmatism, metamorphism, orogeny, basin formation and sediment compaction, climatic changes, as well as accompanying changes in biological activity. All these processes are linked throughout the Earth geological history to major changes in geodynamic, atmospheric, astronomic, and biologic processes. As such, mineral deposits are an integral part of Earth's evolution through time and their occurrence is an expression of complex interactions between the different spheres of our planet.

Isotopes (derived from the two Greek words "iso", same, and "topos", place) are nuclides of the same element and are therefore characterized by the same number of protons but different numbers of neutrons (Fig. 1), resulting in different masses. In the Earth there are both stable and unstable natural isotopes. Unstable isotopes are radioactive and decay naturally, with variable decay rates, to other isotopes, that may be, in their turn, either radioactive or stable. Stable isotopes are either radiogenic, when they derive from the decay of a radioactive isotope, or non-radiogenic when they have been produced by nucleosynthetic processes in stars and supernovae or by cosmic ray spallation of interstellar dust prior to the solar system formation. Stable radiogenic isotopes are generated by primordial radioactive isotopes with decay rates much slower than the age of the Earth (e.g., ^{232}Th, ^{238}U, ^{235}U, ^{187}Re, ^{176}Lu, ^{147}Sm, ^{87}Rb, ^{40}K), which have been incorporated in the Earth at the time of its formation because they were previously formed in stars and supernovae. These primordial radioactive nuclides have produced stable radiogenic isotopes (e.g., ^{208}Pb, ^{206}Pb, ^{207}Pb, ^{187}Os, ^{176}Hf, ^{143}Nd, ^{87}Sr, ^{40}Ar) that have been added throughout Earth's history to the amounts of the same stable non-radiogenic isotopes incorporated in the Earth at the time of the solar system formation. Some primordial radioactive isotopes have gone extinct early in the Earth's history and may be used to infer early Earth processes (e.g., ^{146}Sm decayed to ^{142}Nd, ^{182}Hf decayed to ^{182}W).

Some rare nuclides are also generated continuously on rocks and soils of the Earth's surface as well as in the Earth's atmosphere by cosmic rays interacting with primordial isotopes. Such cosmogenic nuclides can be both stable and radioactive and some of them have important geological applications (e.g., ^{14}C generated by interaction of cosmic rays with ^{14}N is used for dating of C-bearing materials younger than ~40 ky; ^{10}Be is used to track the input of subducted sediments into subduction-related magmas and the sources and circulation of marine water masses, while ^{7}Be is used to track atmospheric circulation).

The majority of naturally existing isotopes in the Earth are stable non-radiogenic, so have not been further produced by radioactive decay of other nuclides since the time of the solar system formation. Therefore, considering the bulk Earth as a closed system, the absolute abundances of non-radiogenic stable isotopes are fixed and correspond to those of the chondritic material that formed the Earth. However, distinct reservoirs and geological materials of the Earth at different scales, ranging from rocks to minerals and sub-grains, may be characterized by a redistribution of non-radiogenic stable isotopes of the same element that results in different ratios of these isotopes. The fundamental reason for this isotopic redistribution is that, while the isotopes of the same

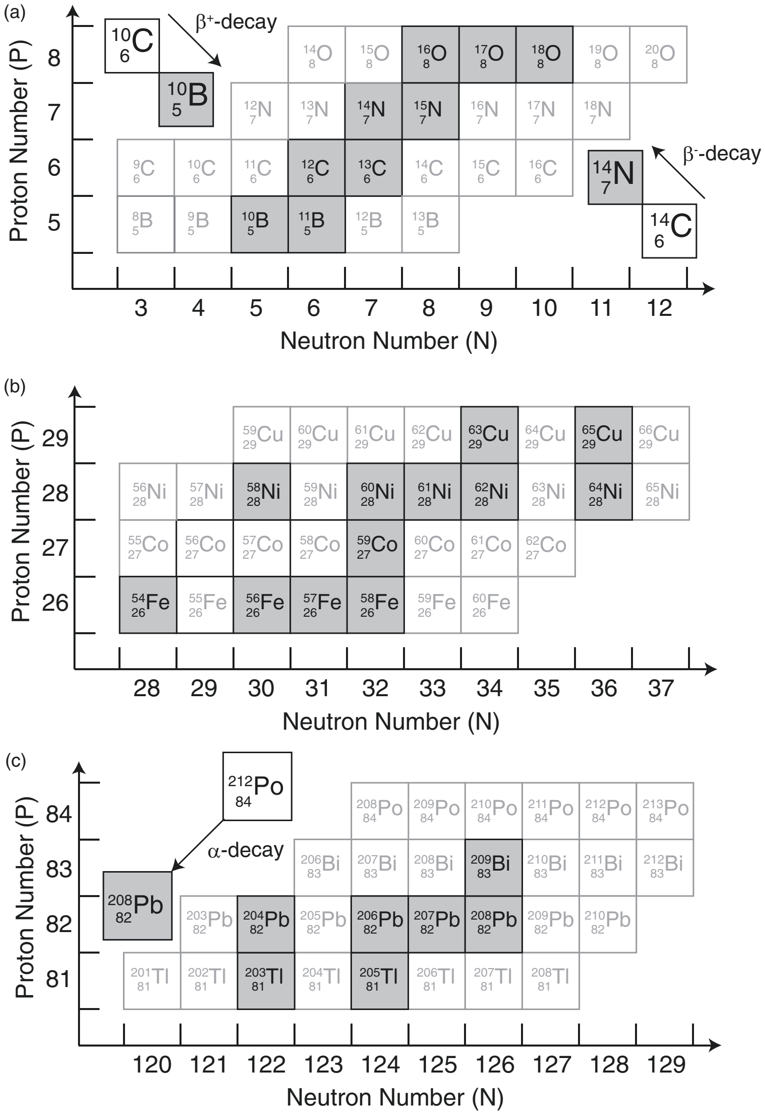

Fig. 1 Graphic examples of stable (grayed cases) and radioactive (white cases) isotopes and of the α and β decay processes in the pertinent portions of the nuclide table. (a) Example of light stable non-radiogenic and radiogenic isotopes (B, C, N, O). (b) Example of transition metal non-radiogenic stable isotopes (Fe, Co, Ni, Cu). (c) Example of heavy stable non-radiogenic (Tl) and radiogenic (Pb) isotopes, as well as of radioactive isotopes (Bi, Po).

element have the same electronic configuration and hence the same geochemical behavior, the different masses of their nuclei, related to the different number of neutrons, make them behave differently in a range of physico-chemical processes (for more details see for example O'Neil, 1986). Because the main parameter controlling the behavior of different isotopes of the same element is their mass (mass-dependent fractionation or MDF), isotopic effects are much more important for isotopes with larger relative mass differences: for instance, the fractionation between ^{2}H and ^{1}H is larger than that between ^{16}O and ^{18}O during water evaporation. For a specific mass difference, in general the higher is the atomic mass of an element the lesser will be the fractionation effects between its isotopes. However, elements of biogeochemical importance and/or those that can occur in phases with different chemical oxidation states (valency) may still show measurable isotopic fractionations despite having a high masses (e.g., Hg, Mo, Cr, Fe, Cu, Zn).

Both equilibrium and kinetic MDF between the compounds containing and competing for the isotopes in question can occur. For equilibrium fractionation, the reactions occur slowly enough to allow a continuous thermodynamic equilibration between reactants and products. Mass-dependent equilibrium fractionations at any given temperature between two compounds are predictable based on molecular thermodynamics (e.g., Schauble et al., 2009). This thermodynamic preference for the heavier or lighter isotopes can also be noted if two different elements containing two or more stable isotopes are bonding within the same molecule. The recently discovered "clumping" of two heavy isotopes of different elements, that occurs as a molecular anomaly within a reaction product and where that clumped molecule also has stronger bonds compared to non-clumped molecules, is also thermodynamically predictable. Similar to the normal fractionation factor (α), the clumped anomaly is favored at lower temperatures compared to higher temperatures of reaction (e.g., Schauble et al., 2006; Eiler, 2007). Such "clumping" of the heavy isotopes, that expresses itself as an anomalous concentration of the heavy isotopes of two different elements (^{13}C and ^{18}O in carbonates or CO_2, for example) on a molecular basis in the product phase compared to a random, stoichiometric distribution of the heavy isotopes of both elements based on their total abundance, offers a new single mineral thermometer for isotope fractionation (Eiler, 2007).

In mass-dependent equilibrium fractionation, products may be characterized by either lighter or heavier isotope compositions depending on parameters including the strength of the chemical bonds of products versus reactants, their density and/or their physical state (solid vs. liquid vs. vapor, crystallography), and/or changes in the oxidation state of the element concerned. In contrast, mass-dependent kinetic fractionation, related to the speed of the movement of the isotopes, will result in products of a reaction that are isotopically lighter compared to the reactants, which may either enhance the magnitude of the predictable equilibrium fractionation or may lead to a reversal in the sign of the equilibrium fractionation factor (O'Neil, 1986; Schauble et al., 2009; Hoefs, 2015; Sharp, 2017). Kinetic fractionation may also be important for diffusive processes, rapid precipitation of minerals under conditions of oversaturation, and/or for reactions that are mediated by biological activity (e.g., Zn isotope fractionation by phytoplankton and Cu isotope fractionation by bacteria: Maréchal et al., 2000; Mathur et al., 2005; Bermin et al., 2006). In all these cases, the lighter isotopes of the reactants are preferentially used to form the products because they are less tightly bound compared to the heavier isotopes. In addition, biologically mediated reactions are often associated with a change in valency, which also has a strong influence on the vibrational frequency shifts for the bonds of the element of interest and hence on the magnitude of fractionation.

It should be noted that some elements containing more than two stable isotopes (e.g., Hg, S, O) may also be subjected to mass-independent fractionation (MIF), a fractionation that does not scale with mass differences between the isotopes and is often related to photochemistry and the impacts of certain wavelengths of cosmic radiation on the vibrational frequencies of bonds in particular isotopologues (Thiemens and Lin, 2021). Although MIF has important applications in geology, like in the study of the Hg geochemical cycle (Bergquist and Blum, 2007) or in the detection of the Great Oxidation Event thanks to MIF of sulfur isotopes (Farquhar et al., 2000), we will not deal with MIF in this chapter because, at this time, there are not yet extensive mineral deposit studies that have used MIF.

Mass-dependent (and mass-independent) isotopic variations can be used for geological interpretations only for non-radiogenic stable isotopes. Radiogenic stable isotopes cannot be used to track mass-dependent (and mass-independent) fractionation processes because their abundances in natural systems are heavily affected by radioactive decay. This interferes with any potential isotope variability due to mass-dependent (and mass-independent) processes, because stable radiogenic isotopes have been continuously produced within Earth's reservoirs (e.g., mantle, crust) and materials (e.g., rocks, minerals) since the Earth's formation. Therefore, the distribution of radiogenic isotopes is no longer dependent only on reaction conditions but also, and overwhelmingly, on the time span of their accumulation by radioactive decay of the parents and on the relative abundances of the parent radioactive isotope and the daughter radiogenic stable isotope.

Isotope studies allow addressing broad questions in mineral deposit research, such as: (i) what are the sources of hydrothermal fluids and/or those of the metals?; (ii) which were the features of the fluid plumbing system?; (iii) what were the physico-chemical conditions and also the inorganic and biological factors under which hydrothermal fluids transported and deposited the metals?; (iv) what was the timing and the age of ore formation?

The ability of isotopes to address the above range of questions derives from their power of coupling element geochemical information with the response of the different isotopes of an element to changes in physico-chemical processes and the time factor that is implicit in radioactive-radiogenic isotope pairs. Under this point of view, non-radiogenic stable isotopes are able to track physico-chemical processes related to mineralization, such as temperature, fO_2 conditions, equilibrium versus kinetic fractionation during mineral precipitation, low-temperature remobilization of metals (Fe, Cu, Zn), besides tracking sources of the aqueous fluid phase (O, H), of ligands (e.g., Cl, S), and to some extent of metals (e.g., Zn, Cu, Fe). In contrast, stable radiogenic isotopes are ideally suited to track sources of metals (Pb, Os) in mineral deposits, to derive information on the hydrothermal plumbing systems (e.g., variably homogeneous mixing or heterogeneous mixing implying long-lived hydrothermal cell convection, versus unidirectional flow paths), and, in conjunction with the radioactive parent (e.g., U—Pb, Re—Os, K—Ar systems), to date magmatic and hydrothermal activity.

Because a number of reviews have already been published on applications of classical light stable isotope compositions (e.g., H, B, C, N, O, and S) to mineral deposit research (e.g., Ohmoto, 1986; Taylor, 1987; Ohmoto and Goldhaber, 1997; Taylor Jr, 1997; Seal et al., 2000; Seal, 2006; Taylor, 2007; Shanks III, 2014), this chapter focusses on radiogenic stable metal isotopes (e.g., Pb, Os) and on transition metal stable, non-radiogenic isotopes (e.g., Fe, Cu, Zn). Where appropriate, the case studies discussed here also refer to classical light stable isotope compositions (mostly H, C, O, S) to highlight the power that the combined use of various isotope systems have, notably in refining the answers to questions (i) to (iii) above. Similarly, other radiogenic isotopes (e.g., Sr, Nd) are briefly discussed in some cases to complete information derived from Pb and Os isotopes. Another important part of the chapter is dedicated to the dating of mineral deposits by various methods (e.g., U—Pb, Re—Os, Ar/Ar).

Although we discuss some basic concepts of isotope geochemistry, we cannot address all details of such a vast topic in this chapter, that is essentially focused on the application of isotopes to metallic mineral deposits. Therefore, we invite the readers to consult more specialized works on isotope geochemistry cited in various places of this chapter (e.g., general text books like Faure and Mensing, 2005; Dickin, 2005; Johnson et al., 2004), should they want to deepen their understanding of those details.

Sampling and analytical strategy in isotope investigations

Isotope investigations can be carried out at different scales, i.e., from the single crystal and parts of it (i.e., millimeter to μm scale) to hand-size samples. Additionally, samples can be collected at the outcrop scale, at the deposit scale, or at the mineral district and regional scales. The number of samples to be analyzed depends on the scope and the scale of the investigation (the reader may consult Richards and Noble, 1998 for useful information about sampling methodologies and strategies depending on the goal and isotopic technique used). In any case several samples should be analyzed for each single deposit to track homogeneity or heterogeneity of isotope compositions at various scales of the deposit. Heterogeneity can eventually be linked to the 2D geographic (if only surface samples are investigated) or 3D (if also drill core samples are investigated) positions of the samples to detect the presence of zoning that can inform us about the plumbing hydrothermal ore system, the hydrothermal fluid path and its interaction with host rocks, differences in fluid properties, and precipitation mechanisms.

Homogeneity and heterogeneity can also be detected at the μm scale of single crystals. Mineral deposits form in geologically short but non-instantaneous time intervals, and physico-chemical conditions and sources may change. Analyzes of tiny zones of single crystals may provide valuable information about the temporal evolution of the ore system (e.g., Li et al., 2018, 2022), but require a method that samples small volumes of single crystals in a texturally controlled environment (see below). Analysis of a bulk sample (i.e., rock, multigrain mineral separate, bulk single crystal) represents a time-integrated sum of all the processes that a sample has undergone, i.e., it is a time-averaged signal of a series of processes. Analyzes of the tiny volumes in a zoned crystal deconvolve the integrated signal by representing snap shots of the crystal's evolution. Two microanalytical techniques are widely used: (i) microdrilling of texturally constrained minerals, with spatial scales of several hundred μm or $\sim 10^6$ μm^3; (ii) in situ spot analyzes via either a laser ablation system (LA-MC-ICPMS) or with ion probe (SIMS), with spatial scales of only a few tens of μm or $\sim 10^3$–10^4 μm^3. Normally there is a trade-off between spatial and analytical resolution such that smaller analytical volumes yield larger errors. Depending on research scope, either bulk rock/mineral or in situ analyzes (or both) can be collected. Temporal evolution at mineral deposits may also be investigated at larger scales, e.g., through cross-cutting or stratigraphic relationships.

Another possible approach is the analysis of the isotopic composition of fluids instead of minerals. Minerals, during their growth by precipitation from a hydrothermal fluid, invariably trap inclusions of those fluids, which can be analyzed directly through in situ techniques (Pettke et al., 2010; see below) or by bulk crushing and leaching of the fluids (e.g., Chiaradia et al., 2004; Rottier, 2017). In the latter case a problem is that different fluid generations (even not related to the primary mineralization but to later events that have cracked and re-sealed the minerals trapping "exotic" fluids) are possibly analyzed. Finally, fluids from active geothermal systems associated with potentially forming mineral deposits can also be analyzed for their isotopic compositions (e.g., de Ronde et al., 2011; Chiaradia et al., 2018).

All types of isotope studies (i.e., light stable isotopes, heavy stable isotopes, radioactive-radiogenic isotopes) make large use of both bulk rock, single grain to subgrain, and in situ analytical approaches.

Instrumentation

Isotope compositions of geological solid and liquid materials are measured by mass spectrometry (the reader may consult Faure and Mensing, 2005; Dickin, 2005 for more detailed introductions to mass spectrometry). A mass spectrometer consists of three main parts: (i) an ion source that ionizes the element whose isotopes need to be measured; (ii) a mass analyzer where isotopes are separated from each other according to their mass/charge ratio; (iii) a detection system which allows to quantify the amounts of the different isotopes of the sample arriving at the detector and to convert them into ratios of those isotopes. In the most commonly used mass spectrometers the mass analyzer and detection system are similar, but the ion source changes depending on the type of elements analyzed. Currently the following types of mass spectrometry techniques are the most used for determination of isotope compositions:

1. Thermal ionization mass spectrometry (TIMS). In this technique the ionization of the element to be analyzed is achieved thermally by heating a pure separate of the element (usually in the form of a salt) loaded onto a high work function metal filament (e.g., Re, Pt, Ta) which is heated under vacuum at temperatures between 1000 °C and >2000 °C depending on the element. An activator is usually added to increase the ionization efficiency. This technique is routinely used for U—Pb, Re—Os, Rb—Sr and Sm—Nd isotope determinations, among others. To avoid interferences of isobars and ionization suppression, bulk rocks, single grains or their portions, are dissolved in acids and the elements of interest are separated from each other through column chemistry before being measured on a thermal ionization mass spectrometer. A spike solution, usually made with one or two isotopes of the element to analyze, is added to the sample when a high-precision determination of the concentration of the element is needed, e.g., for high-precision Isotope Dilution (ID)-TIMS dating of zircon and molybdenite. No spike addition is needed for "routine" isotope ratio determinations.
2. Noble gas mass spectrometry. In this technique ionization of a noble gas (e.g., Ar) is achieved under vacuum by a flux of electrons from a heated filament. Prior to ionization the gas is extracted from the sample (e.g., a pure mineral separate) through heating with a furnace or laser or also through mechanic decrepitation. This is the technique used, among others, for $^{40}Ar/^{39}Ar$ dating (see below). In situ dating of portions of minerals using a laser coupled to the mass spectrometer is also possible with this technique.

3. Gas isotope ratio mass spectrometry (GIRMS). For the conventional light stable isotope analyzes, new variants of the classical "Nier-type" gas-source mass spectrometer (Nier, 1940) are most commonly used. For this approach, an analyte gas is produced for the isotopic system of interest (e.g., H, C, N, O, S) using either offline vacuum extraction lines or more recently online carrier-gas (He) based preparation devices such as Elemental Analyzers (EA's), automatic carbonate preparation lines or laser fluorination lines. The analyte gas of interest (H_2, CO_2, CO, N_2, O_2, SO_2 or SF_6) is prepared by high temperature (>1000 °C) oxidation (CO_2, N_2, SO_2) or reduction (H_2, CO), low-temperature (25, 50 to 90 °C) acidification of carbonates (CO_2), or fluorination of silicates, oxides, and/or sulfides (O_2 or SF_6, respectively) for a complete conversion of solids and liquids to the analyte gas. This is followed by either a vacuum distillation (offline) or gas chromatographic clean-up of the analyte gas (online, carrier-gas systems) prior to the mass spectrometric measurement of the analyte gas. The analyte gas is measured for its isotopic composition, calibrated against a pure reference gas of the same elemental composition but of known isotopic composition, that is introduced in parallel to the analyte gas. The whole preparation, extraction, as well as measurement procedure is normalized by standard liquids or solids, ideally of the same elemental composition as the samples of interest (e.g., Coplen et al., 1996). More recent advances in cavity-ring-down mass spectroscopy have developed new ways of "optically" measuring the isotopic composition of analyte gasses.
4. Laser Ablation-(Multi-Collector)-Inductively Coupled Plasma Mass Spectrometry (LA-(MC-)ICPMS). Element ionization in this technique is achieved in an argon plasma which reaches temperatures of up to ~8000 °C. Virtually all elements are ionized and can be analyzed with this technique, in particular transition elements which are notoriously difficult to ionize. Sample preparation is the same as that carried out for TIMS analyzes, i.e., acid dissolution and column chemistry to separate the element of interest from the matrix. A great advantage of MC-ICPMS is also the possibility to be coupled with a laser ablation system, which allows the determination of in situ isotopic compositions. Laser ablation coupled to a multi- (LA-MC-ICPMS) or single (LA-ICPMS) collector mass spectrometer is routinely used for dating zircons and other minerals (e.g., titanite, cassiterite, monazite, hematite, calcite). However, this versatile technique can also be applied to in situ isotopic determination of many other elements on various minerals (e.g., Sr isotopes on plagioclase, Pb isotopes in fluid inclusions, Hf isotopes in zircons). The material analyzed is ablated by a laser inside an ablation cell and transferred to the mass spectrometer where it is ionized and isotope ratios are measured. The ablated material corresponds usually to circular pits of 30–60 μm in diameter and a few μm in depth for a total ablated volume in the order of 10^3–10^4 μm^3 compared to minimum volumes of ~10^5–10^6 μm^3 for TIMS analyzes (Sylvester, 2008) (Fig. 2). MC-ICPMS of the last generation are equipped with filter and collision cell technologies that allow the separation of isobars inside the mass spectrometer (Dauphas et al., 2022), which heavily affect isotope measurements of the ablated aerosol in MC-ICPMS, on which previous chemical separation cannot obviously be carried out. Isotopic measurements of minerals using LA-MC-ICPMS require always a careful consideration of isotope fractionation occurring in the plasma and ablation cell through the use of standards that match mineralogically the investigated mineral (matrix-matched standards).

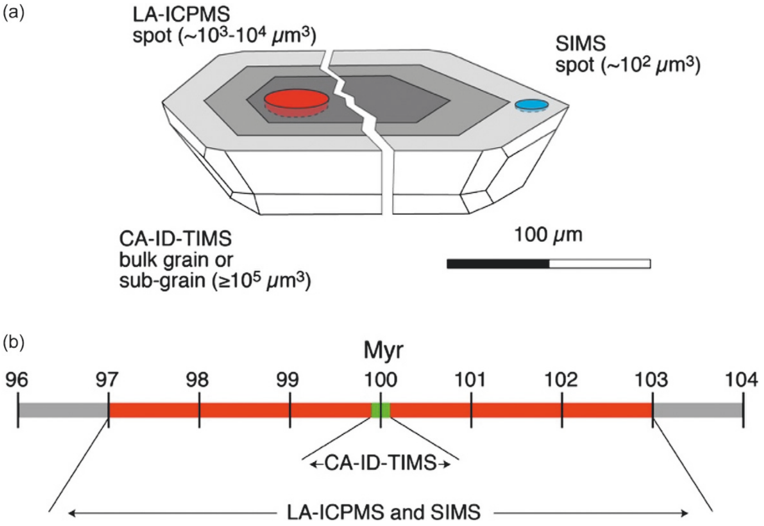

Fig. 2 Analytical techniques of high-precision U—Pb geochronology. (a) CA-ID-TIMS: Chemical-Abrasion, Isotope-Dilution Thermal Ionization Mass Spectrometry can be applied to bulk single grains or portions of them. LA-ICP-MS (Laser Ablation Inductively Coupled Plasma Mass Spectrometry) and SIMS (Secondary-Ion Mass Spectrometry) are in situ techniques allowing a much higher spatial resolution but a smaller volume of analyzed material. (b) Different precisions of the CA-ID-TIMS versus the in situ LA-ICPMS and SIMS methods resulting from the different volumes of zircon analyzed by these methods. The 2SD error bars refer to single spot or single grain/fraction of a zircon 100 Myr old assuming typical precisions associated with the two methods (i.e., 0.1% for CA-ID-TIMS and 3% for LA-ICPMS and SIMS). See text for further discussion. From Chiaradia M (2023) Radiometric dating applied to ore deposits: Theory and methods. In: Huston DL and Gutzmer J (eds.), *Isotopes in Economic Geology, Metallogensis and Exploration*. Springer: Berlin (in press); Modified from Schaltegger U, Wotzlaw JF, Ovtcharova M, Chiaradia M and Spikings R (2014) Mass spectrometry in Earth sciences: The precise and accurate measurement of time. *Chimia International Journal for Chemistry* **68**(3): 124–128.

5. Secondary Ion Mass Spectrometry (SIMS) is used to determine in situ isotope ratios of various elements for tracing studies (e.g., H, Li, B, C, O, Mg, S) as well as for in situ U—Th—Pb dating of minerals. This technique is conceptually similar to LA-(MC-)ICPMS but differs in the way by which the analyzed elements are extracted from the mineral. In SIMS an ion beam (usually of oxygen or cesium ions, depending on the element to be analyzed) hits the mineral surface and sputters it producing secondary ions that are accelerated and focused into the mass spectrometer. The beam size can be as small as 15 μm thus providing the highest spatial resolution of all isotope measurement techniques, but also resulting in smaller volumes of analyzed material ($\sim 10^2$ μm^3; Sylvester, 2008) (Fig. 2). Like for LA-(MC-)ICPMS, also SIMS requires the use of standards that match mineralogically the investigated mineral (matrix-matched standards) to monitor and correct fractionation effects.

The in situ analytical techniques (4 and 5 above) allow a better resolution (10–40 μm; Fig. 2), a better textural control (better optical microscopy coupled with the LA-ICPMS and SIMS than with a microdrill), and a much faster analytical acquisition, i.e., a larger data output. However, by virtue of the smaller amounts of material analyzed, precision is not as high as with the bulk methods (1, 2, 3 above; Fig. 2) and accuracy relies on control of matrix effects through the analyzes of matrix-matched standards (e.g., Miliszkiewicz et al., 2015).

The "bulk" minerals (1,2,3) and in situ (4 and 5) methods should be viewed as complementary and the choice of one or the other depends on the actual goals of the isotopic analysis. For instance, high precision dating by ID-TIMS is the only technique to constrain the timescales of hydrothermal events where minerals can be dated precisely and accurately by high-precision U—Pb and Re—Os techniques, whereas in situ techniques are the choice for regional studies (requiring the analysis of higher numbers of samples without the need for a high precision) and for dating minerals with complex textures indicating several growth episodes (e.g., Chiaradia et al., 2013, 2014). High precision ID-TIMS dating of zircon may also benefit from previous dating of the same zircons by in situ methods in order to allow a selection of the most appropriate zircon grains to be subsequently dated by the more labor-intensive ID-TIMS technique (e.g., Chelle-Michou et al., 2014; Chiaradia et al., 2014).

Radioactive-radiogenic isotope systems

Bases of radioactive-radiogenic isotope systems

As discussed in the Introduction, radioactive parents and their stable radiogenic isotopes allow the identification of potential metal sources in mineral deposits, the characterization of the plumbing system (e.g., homogeneous vs. heterogeneous mixing), the likelihood of fluid-rock interactions during the transport of the fluid from the source to the depositional site, and also the dating of the absolute time and duration of mineral deposit formation. Before discussing more in detail individual radioactive-radiogenic isotopic systems and their applications to different types of mineral deposits, it is useful to introduce some general concepts that are applicable to all radioactive-radiogenic isotope systems.

Radioactivity is the process through which naturally occurring unstable isotopes of various elements emit sub-atomic particles and energy resulting in changes of the number of protons and neutrons: this leads to the transformation of an initial isotope into an isotope of another element (Rutherford and Soddy, 1902a, 1902b) (Fig. 1). As mentioned in the Introduction, some radioactive isotopes present in the solar nebula have been incorporated into the Earth when the latter formed and still exist today due to their slow decay rates (e.g., ^{232}Th, ^{238}U, ^{235}U, ^{187}Re, ^{176}Lu, ^{147}Sm, ^{87}Rb, ^{40}K: Table 1). Over ~4.55 Gyr of Earth's history they have continuously produced the corresponding stable radiogenic daughter isotopes (e.g., ^{208}Pb, ^{206}Pb, ^{207}Pb, ^{187}Os, ^{176}Hf, ^{143}Nd, ^{87}Sr, ^{40}Ar), which have been added to the primordial (i.e., occurring at the time of Earth's formation) amounts of the same isotopes.

Several types of radioactive decay exist, the most common (i.e., those of the above-mentioned elements; Table 1) being β^-, β^+, electron capture, and α decays (Fig. 1; see specific literature for more details, e.g., Faure and Mensing, 2005; Dickin, 2005). The radiogenic products of radioactive decay may be stable (i.e., non-radioactive) daughter isotopes (a typical example is the decay of ^{187}Re to stable ^{187}Os by β^- decay or the decay of ^{147}Sm to ^{143}Nd by α decay) or daughter isotopes that are themselves radioactive parents and decay to another daughter isotope. For example, in Fig. 1, ^{212}Po is the radioactive daughter of ^{212}Bi (through a β^- decay) and decays through α decay to stable ^{208}Pb, i.e., the last step of the decay chain of ^{232}Th to ^{208}Pb.

The decay rate of a large population of a particular radioactive isotope is statistically constant (and for this reason it is called the decay constant, identified by the Greek letter λ), can be measured and quantified, and does not change significantly with variations of physico-chemical parameters like temperature, pressure and composition of the phase hosting the radioactive isotopes (e.g., Faure and Mensing, 2005). Different radioactive parent isotopes have rates of decay encompassing >10 orders of magnitude (Table 1). Thus, an increasing number of radiogenic isotopes are produced by the decay of the radioactive parent through time. Time, rate of decay and atomic abundances of parents and daughters are linked together through a simple exponential equation

$$D^* = N_0\left(e^{\lambda t} - 1\right) \tag{1}$$

where D^* and N_0 are the numbers of radiogenic daughter and radioactive parent isotopes, respectively, measured in the system today, λ is the decay constant, and t is the time since the system (e.g., mineral, rock, geological reservoir) has formed incorporating the radioactive parent isotope.

Table 1 Decay schemes and applications to dating mineral deposits of selected radioactive isotopes.

Decay scheme	*Decay constant*	*Decay process*	*Half-life (y)*	*Types of datable minerals*	*Datable minerals*	*References*
$^{238}U \rightarrow {}^{206}Pb$	1.55125×10^{-10}	α and β^-	4.468×10^9	Magmatic and hydrothermal ore-associated minerals ± ore minerals (e.g., cassiterite)	zr, tit, rt., bd, xen, mon, all, cs, gar	1
$^{235}U \rightarrow {}^{207}Pb$	1.54993×10^{-10}		4.472×10^9			2
	9.8485×10^{-10}		0.7038×10^9			1
	9.8569×10^{-10}		0.7032×10^9			2
$^{232}Th \rightarrow {}^{208}Pb$	4.9475×10^{-11}	α and β^-	14.010×10^9	Magmatic and hydrothermal ore-associated minerals ± ore minerals	all, mon	1
$^{187}Re \rightarrow {}^{187}Os$	1.666×10^{-11}	β^-	4.161×10^{10}	Ore minerals (sulfides)	mol, various sulfides	3
	1.6668×10^{-11}		4.159×10^{10}			4
$^{40}K \rightarrow {}^{40}Ar$	5.755×10^{-11}	Electron capture	1.204×10^{10}	Gangue hydrothermal minerals ± fluids contained in ore and gangue minerals	K-bearing minerals (e.g., micas, amph, Kf, al) and fluids	5
$^{87}Rb \rightarrow {}^{87}Sr$	1.42×10^{-11}	β^-	4.881×10^{10}	Gangue hydrothermal minerals ± fluids contained in ore and gangue minerals	micas, Kf, sl, and Rb-bearing fluids (as inclusions in, e.g., quartz)	6
$^{147}Sm \rightarrow {}^{143}Nd$	6.54×10^{-12}	α	1.060×10^{11}	Certain gangue and ore minerals (e.g., scheelite)	cpx, gar, sch	7
$^{176}Lu \rightarrow {}^{176}Hf$	1.94×10^{-11}	β^-	3.57×10^{10}	Certain gangue minerals	gar	7
$^{234}U \rightarrow {}^{230}Th$	2.829×10^{-6}	α	2.45×10^5	Young zircons and carbonates	zr, carbonates	8
$^{230}Th \rightarrow {}^{226}Ra$	9.1929×10^{-6}	α	7.54×10^4	Young zircons and carbonates	zr, carbonates	8

Decay constant and half-life values are from the mentioned references. However, the reader should be aware that continuous refining of these values is proposed in the literature. al, alunite; all, allanite; amph, amphibole; bd, baddeleyte; cpx, clinopyroxene; cs, cassiterite; gar, garnet; Kf, K-feldspar; mol, molybdenite; mon, monazite; rt., rutile; sch, scheelite; sl, sphalerite; tit, titanite; xen, xenotime; zr, zircon. References for decay constants and half-lives: 1—Steiger and Jaeger (1977); 2—Schoene et al. (2006); 3—Smoliar et al. (1996); 4—Selby et al. (2007); 5—Renne et al. (2010); 6—Neumann and Huster (1974); 7—Faure and Mensing (2005); 8—Lide and Frederikse (1995).

Modified from Chiaradia M (2023) Radiometric dating applied to ore deposits: Theory and methods. In: Huston DL and Gutzmer J (eds.), *Isotopes in Economic Geology, Metallogensis and Exploration*. Springer: Berlin (in press).

In the greatest majority of geological systems, a significant amount of daughter radiogenic isotope (accumulated from decay of the parent prior to the system formation) may be also incorporated from the surrounding environment at the time of the system formation. This makes that the number of radiogenic isotopes present in the system after a certain time t will be

$$D = D_t + D^* \tag{2}$$

where D is the total amount of daughter isotope resulting from the sum of the daughter isotope incorporated from the surrounding environment at the time t of formation of the system (D_t) plus the daughter isotope produced within the system after its formation at time t by decay of the incorporated radioactive parent (D^*), of which today remains a number of atoms equal to N_0 (Eq. 1).

Thus, Eq. (2) above becomes, by substituting Eq. (1) into it,

$$D = D_t + N_0\left(e^{\lambda t} - 1\right) \tag{3}$$

In geological terms, this would be the case, for example, of a mineral crystallized from a magma or precipitated from a hydrothermal fluid at time t. This mineral incorporates a certain number of the daughter radiogenic isotope present in the magma or fluid at time t (D_t) and also a certain number of isotopes of the radioactive parent (N) present in the magma/fluid, of which the number remaining today is N_0 in Eq. (3). The proportion in which parent and daughter isotopes are incorporated is different from mineral to mineral crystallized from the same magma or precipitated from the same fluid, because it depends on the different mineral-melt or mineral-fluid partition coefficients of the parent (N) and daughter (D) isotopes.

D_t in turn is the result of the decay of the radioactive parent N added to another initial amount of D (e.g., D_T) between an older time T and the time t when the mineral under consideration formed, so that

$$D = \overbrace{D_T + N_t\left(e^{\lambda T} - e^{\lambda t}\right)}^{D_t} + \overbrace{N_0\left(e^{\lambda t} - 1\right)}^{D^*} \tag{4}$$

where the first two terms on the right-hand side of the equation are D_t and the third is the amount of radiogenic isotope (D^*) produced within the mineral since the time (t) of its crystallization.

In mass spectrometry it is analytically easier (see above) and more convenient for data interpretation to measure isotope ratios instead of absolute amounts of isotopes, although absolute amounts of isotopes, obtainable adding a spike solution (isotope dilution method: see Faure and Mensing, 2005 for further details), are needed when we want to date minerals with Eq. (1) above. Therefore, Eqs. (2) and (4) can be transformed by dividing each member by a reference isotope, which is usually a stable non-radiogenic isotope of the same element, e.g., for Eq. (3)

$$\frac{D}{D_{ref}} = \frac{D_t}{D_{ref}} + \frac{N_0}{D_{ref}}\left(e^{\lambda t} - 1\right) \tag{5}$$

When more than one stable non-radiogenic isotopes are available for normalization, the choice is for the one with the abundance closer to that of the radiogenic isotope, which corresponds to the best precision obtainable on the isotope ratio measurement with a mass spectrometer (see also Richards and Noble, 1998). Eq. (5) shows that the variability of the ratio D/D_{ref} in geological materials, assuming the same value of D_t/D_{ref} (i.e., a homogeneous magma or fluid from which the mineral forms), depends on two main parameters: the time t and the ratio N_0/D_{ref}. When a mineral crystallizes from an isotopically homogeneous magma or hydrothermal fluid the radiogenic to non-radiogenic stable isotope ratio (D_t/D_{ref}) is the same as that of the reservoir (magma or fluid) from which it has formed. This is so because the proportion in which D_t and D_{ref} are taken by the mineral is the same as that of the magma or fluid from which the mineral has crystallized/precipitated, because both D_t and D_{ref} are isotopes of the same element and therefore have a very similar geochemical behavior. Potential subtle changes due to kinetic and equilibrium fractionation effects are overwhelmingly masked by the much larger changes due to the effect of radioactive decay through time and the decoupling between parent and daughter isotopes (N_0/D_{ref}) in different geological materials, highlighted by Eq. (5).

Eq. (5) shows that each mineral (or geological material, like a bulk rock or Earth's reservoir) preserves a memory of its initial isotopic composition (D_t/D_{ref}), i.e., the isotopic composition that it had at a certain time t in the past that corresponds to a significant geological event, like the crystallization of a mineral from a magma or a fluid. Examining more in detail Eq. (5) we can distinguish three end-case scenarios:

(i) Systems in which $D_t/D_{ref} \sim 0$. In such a case Eq. (5) reduces to

$$\frac{D}{D_{ref}} = \frac{N_0}{D_{ref}}\left(e^{\lambda t} - 1\right) \tag{6}$$

i.e., the amount of radiogenic isotope measured today corresponds entirely to the amount formed in situ by radioactive decay. This equation, in the form of Eq. (1), can be used to determine the absolute age of a mineral

$$t = \frac{1}{\lambda}\ln\left(\frac{D^*}{N_0} + 1\right) \tag{7}$$

Typical examples of systems that have such a behavior are zircon and molybdenite, which incorporate from the surrounding environment significant amounts of a radioactive parent (U and Re respectively) but virtually no radiogenic daughter isotopes (i.e., Pb and Os, respectively). Such systems are ideal for dating because Eq. (7) can be easily solved for t by measuring D^* and N_0 and knowing the constant λ:

$$t = \frac{1}{\lambda^{238}}\ln\left(\frac{^{206}Pb_0}{^{238}U_0} + 1\right) \tag{8}$$

$$t = \frac{1}{\lambda^{187}}\ln\left(\frac{^{187}Os_0}{^{187}Re_0} + 1\right) \tag{9}$$

where the indices "0" indicate the number of atoms measured in the zircon and molybdenite at present time and λ^{238} and λ^{187} are the decay constants of ^{238}U and ^{187}Re respectively.

(ii) Systems in which $N_0/D_{ref} \sim 0$. In such a case Eq. (5) reduces to

$$\frac{D}{D_{ref}} = \frac{D_t}{D_{ref}} \tag{10}$$

i.e., the ratio of radiogenic to non-radiogenic isotopes measured today is the same as that of the reservoir from which the mineral/rock/reservoir has formed at time t. This is the case of minerals like galena (PbS) for Pb isotopes, osmium-iridium alloys, Os-rich laurite (RuS_2) and chromite ($FeCr_2O_4$) for osmium isotopes, and apatite ($Ca_5[PO_4]_3[OH,Cl,F]$) for Sr isotopes, because in these minerals the ratio N_0/D_{ref} (i.e., $^{238}U/^{204}Pb$, $^{187}Re/^{188}Os$, and $^{87}Rb/^{86}Sr$) is virtually 0. The same situation also occurs for all geological materials (i.e., minerals, rocks, reservoirs) recently formed ($t \approx 0$), since there has not been enough time to allow the growth of the radiogenic isotope from the decay of its parent and the second term on the right-hand side of Eq. (5) reduces to 0.

(iii) Systems which incorporated both parent and daughter elements in measurable amounts at the time of their formation. In such a case Eq. (5) must be considered in full. This represents by far the most common case for minerals and applies to all rock types and Earth's reservoirs (e.g., mantle, crust).

Radiogenic isotopes as tracers of fluid-rock interactions

For source tracing, characterization of the fluid plumbing system and fluid-rock interaction, only radiogenic to non-radiogenic isotope ratios corresponding to the time of the mineralization formation must be considered, because only these reflect the isotopic composition of a certain element when the ore mineral formed. In order to do this, we have two options: (1) either analyze minerals that behave like systems (ii) above, i.e., have N_0/D_{ref} equal to 0, or (2) correct minerals that behave like systems (iii) above for the time-integrated decay of the parent ($N_0 \neq 0$). The preferred solution between the two above (1 and 2) is the first one (1) because it avoids the need to measure the concentrations of parent and daughter isotopes and the age of the mineralization (t), and, most of all, avoids uncertainties in the calculated age-corrected value that are related with potential open-system behavior. The latter is quite common, especially for older mineralization that may have undergone different geological events. If no minerals with $N_0/D_{ref} \sim 0$ are available, then minerals with the lowest possible values of N_0/D_{ref} should be utilized to reduce the uncertainties due to time-integrated corrections discussed above (see examples below for Pb isotopes).

It is important to point out that any isotope composition (radiogenic or stable) of a mineral deposit is the outcome of various metallogenetic processes. In fact, any mineral deposit formed by a hydrothermal fluid (i.e., the greatest majority of primary mineral deposits, except those of orthomagmatic origin) is the result of three main steps (Fig. 3): (i) a source region of fluid and/or metal(s); (ii) a fluid path through which physico-chemical properties of the fluid may change due to fluid-rock interactions and metals can be either lost (precipitated) or gained (leached from the rocks) by the fluid; (iii) a deposition site where the metals are precipitated from the fluid in economic concentrations due to various physico-chemical and even biological reactions. The volumes of the regions involved in steps (i) and (ii) are usually much larger than the volume into which the final mineralization is confined (Fig. 3). In some cases, the flow path may be very short, with the deposition site being very close to the source (e.g., porphyry deposits), or metals can be directly precipitated within their source without the need of a fluid transport (orthomagmatic deposits). Isotope compositions will be affected by each one of these steps and their final composition is the integrated signal of all the three steps. This means that a sound interpretation of isotopes (radiogenic, light and heavy stable non-radiogenic) as metal and fluid tracers and of fluid-rock interactions is possible only if based on a well-established geologic and metallogenetic model applied to specific mineral deposit types (see below).

Below we discuss the Pb and Os isotopic systems and their ability to track sources, hydrothermal fluid plumbing and fluid-rock interaction in mineral deposit studies, because these isotope systems are the most used for metallogenetic applications, due to the fact that, among various potential radiogenic isotope tracers, only Pb and Os are incorporated at significant levels into metallic ores. However, it should be mentioned that other radiogenic isotope tracers, like Sr, Nd and Hf, are used in metallogeny. These elements are incorporated in various minerals, both hydrothermal and magmatic, that are associated with different mineralization types and can provide additional information on fluid sources, plumbing systems, and evolution of magmas intimately associated with specific types of mineral deposits (e.g., porphyry systems). A short reference to these isotope systems will be made where appropriate. Similarly, although this section is focused on radiogenic isotopes, in places we integrate the discussion with information derived from light stable isotopes (e.g., H, O, S). These elements compose a significant (S) to major (H, O) proportion of the hydrothermal fluids and also of the rocks (O), and therefore provide essential information about fluid sources and fluid-rock interactions.

Lead isotopes

The lead-lead isotope system is the most widely used for tracing metal sources, fluid paths, and fluid-rock interactions (Richards and Noble, 1998; Tosdal et al., 1999). The success of this system stems from three features: (i) Pb is a base metal which is a primary commodity in many mineral deposits and is often associated with other base metals like Zn and/or Cu, e.g., in volcanic-hosted massive sulfide (VHMS), sediment-hosted massive sulfide (SHMS) deposits, porphyry and skarn deposits, and also with precious metals Ag and Au, e.g., in epithermal deposits; (ii) Pb has the property, among radiogenic isotopes, to have two radiogenic isotopes (^{206}Pb and ^{207}Pb) derived from two isotopes of the same parent element (^{238}U and ^{235}U, respectively), and a third radiogenic isotope (^{208}Pb) derived from the isotope of another element (^{232}Th), besides one stable non-radiogenic isotope (^{204}Pb). This provides the unique opportunity to evaluate lead isotope data in a tridimensional isotope space (^{206}Pb/^{204}Pb-^{207}Pb/^{204}Pb-^{208}Pb/^{204}Pb) as compared to the unidimensional isotope space of the Re—Os, Rb—Sr, Sm—Nd, and Lu—Hf systems; (iii) the Pb—Pb system has been one of the first to be investigated in detail during the 20th century (e.g., it was used to determine the age of the Earth as we know it nowadays; Patterson, 1956) and therefore it has a long and consolidated

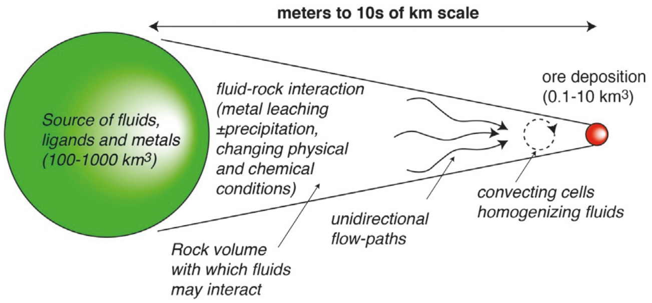

Fig. 3 Simplified sketch of the formation processes of a mineral deposit (see text for discussion).

tradition among isotope geochemists. Because of these reasons we will dwell more on Pb isotope systematics related to mineral deposits, but it will appear that many of the concepts applied to the Pb isotope interpretation of ore systems also apply to other radiogenic (and stable) isotope systems. There are so many studies of Pb isotopes applied to mineral deposits, and with such variable and deposit-dependent interpretations that we have chosen to provide a more conceptual approach to the use of Pb isotopes in metallogeny rather than describing a series of real case applications. In the frame of conceptual interpretations of a number of deposit types we mention studies on specific deposits or mineral belts and shortly illustrate a few of them.

Since the formation of the Earth about 4.55 Gyr ago from the accretion of chondritic material, which had a specific Pb isotope composition inherited from the solar nebula and identified by the isotopic composition of the troilite of the Canyon Diablo meteorite (Tatsumoto et al., 1973), the ratios of radiogenic Pb isotopes (^{206}Pb, ^{207}Pb, ^{208}Pb) to the primordial non-radiogenic isotope (^{204}Pb) have continuously increased due to the presence of initial amounts of primordial U and Th in the chondrite and the fact that ^{238}U, ^{235}U and ^{232}Th have long half-lives (i.e., they decay very slowly and are still present nowadays in the Earth: Table 1). Various models have been proposed for the Pb isotope evolution of the silicate Earth through time, which have considered either the silicate Earth as a homogeneous material with fixed U/Pb and Th/Pb ratios (single-stage Holmes-Houtermans model: Holmes, 1946; Houtermans, 1946), or with changing U/Pb and Th/Pb ratios through time (two-stage model and continuous change model: Stacey and Kramers, 1975; Cumming and Richards, 1975). In these models, the rates of increase of the various isotope ratios differ to accommodate observed isotopic compositions of galenas associated with stratiform deposits (e.g., VHMS-type and SHMS-type deposits) of known age, that were supposed to represent the Pb isotope evolution of the bulk Earth. Lead in galenas is only initial (common) lead (Eq. 10) and therefore reflects the lead isotope composition of the Earth's system frozen at the time of the deposit formation: the aim of the model evolution curves is to fit the model Earth's evolution to that of the stratiform galenas. The common lead of galenas that falls on the model evolution curves is called ordinary. It was soon realized that other galenas, however, contained common lead that did not fall on the model evolution curves but rather along linear trends and this was defined anomalous lead (see below), suggesting that it was derived from a more complex evolution than that of a single-stage, two-stage, or continuous change models (e.g., Kanasewich, 1962; Kanasewich and Farquhar, 1965). Lead of galenas from certain deposits also had very radiogenic values falling significantly to the right of the end-points of the Earth's evolution models, suggesting the occurrence in the Earth of reservoirs with extremely high U/Pb ratios (see below).

Subsequently, other models have been developed to approximate the Pb isotope evolution of different Earth's reservoirs (mantle, upper and lower crust, orogen) on a global or regional scale (e.g., Zartman and Doe, 1981; Zartman and Haines, 1988; Kramers and Tolstikhin, 1997). These models address the more realistic and complex evolution of Pb isotopes through time in the different layers into which an initially uniform Earth has differentiated (e.g., oceanic crust, upper and lower continental crust, mantle). It is common practice to plot lead isotope compositions of ore and rock samples in two isotope plots (uranogenic, i.e., ^{207}Pb/^{204}Pb-^{206}Pb/^{204}Pb and thorogenic, i.e., ^{208}Pb/^{204}Pb-^{206}Pb/^{204}Pb) together with reference curves from any of the model evolution curves of the Earth (Fig. 4). The model curves allow us to better visualize the distribution of the analyzed samples in the lead isotope space with respect to known evolution models of the bulk Earth or of its different reservoirs. All model curves are variably concave downwards in the uranogenic plot and nearly straight lines in the thorogenic plot (Fig. 4). The shapes of the curves in these two plots are controlled by the different decay rates of the radioactive parents (^{235}U and ^{238}U: Table 1) and by the fact that a very little amount of primordial ^{235}U remains in the Earth today so that there has been very little growth of radiogenic ^{207}Pb since ~400 Myr (Fig. 4). Curves displaced towards higher ^{207}Pb/^{204}Pb values in the uranogenic plot are associated with evolutions through higher U/Pb ($\mu = {}^{238}\mathrm{U}/{}^{204}\mathrm{Pb}$) values of the reservoir. Curves displaced towards higher ^{208}Pb/^{204}Pb values in the thorogenic plot are due to higher Th/U ratios of the reservoir. Therefore, the broad isotopic variability of lead in Earth's materials is the coupled result of the time at which the geological material formed and the U/Pb and Th/U compositions of the reservoir from which this material was ultimately derived.

The evolution curves of the plumbotectonics model (Zartman and Doe, 1981) are particularly useful to extract general information about the main reservoir(s) (e.g., upper or lower crust, mantle) from which a magmatic rock or ore lead is derived. In the uranogenic plot, for instance, upper crustal rocks plot at high ^{207}Pb/^{204}Pb values, whereas mantle-derived and lower crustal rocks plot at significantly lower ^{207}Pb/^{204}Pb values for similar ^{206}Pb/^{204}Pb values (Fig. 4a). In the thorogenic plot, the distinction between upper crustal and mantle rocks is less evident whereas the lower crust imprint is clearly shown by higher ^{208}Pb/^{204}Pb at similar ^{206}Pb/^{204}Pb values (Fig. 4b). However, more detailed information on source(s) and plumbing hydrothermal system can only be obtained by analyzing potential source rocks in the region of the mineralization and compare them with the ore lead signature, as explained below.

Principles and general uses of lead isotopes in metallogeny

Let us imagine that we analyze a certain number (e.g., $N = 10$) of ore samples from a certain type of mineral deposit (see Richards and Noble, 1998 for strategies about the number of samples to be collected). The first question to address is whether the isotopic compositions measured are those of the lead carried by the fluid from which the analyzed ore samples formed or not. In fact, we can extract metallogenetic information, e.g., about the source of the lead and the fluid-rock interaction, only from the lead isotope composition of the fluid at the time of the deposit formation, as already discussed above. Ideally, we should use minerals that behave like systems (ii) above (Eq. (10)), e.g., galena (PbS), Pb-sulfosalts (e.g., boulangerite $Pb_5Sb_4S_{11}$), cerussite ($PbCO_3$), anglesite ($PbSO_4$).

If such minerals are unavailable, then Eq. (5), which for Pb can be rewritten as

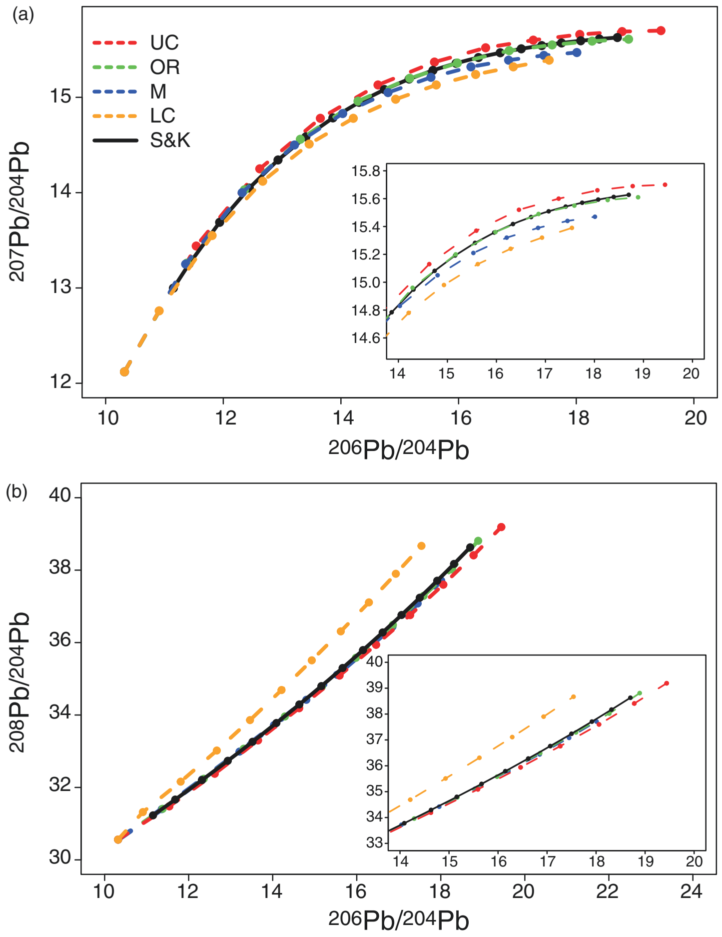

Fig. 4 Pb evolution curves for the plumbotectonics model (Upper Crust UC, Lower Crust LC, Orogene OR, Mantle M) (Zartman and Doe, 1981) and for the second stage of the Stacey and Kramers (1975) model in the uranogenic (^{207}Pb/^{204}Pb vs. ^{206}Pb/^{204}Pb) and thorogenic (^{208}Pb/^{204}Pb vs. ^{206}Pb/^{204}Pb) plots (a and b respectively). Tick marks represent 400 Myr periods of evolution in the models. Insets represent a zoomed view of the evolution curves starting at ^{206}Pb/^{204}Pb values of ~14 to better appreciate differences among the different reservoirs.

$$\frac{^{206}Pb}{^{204}Pb}_{today} = \frac{^{206}Pb}{^{204}Pb}_{initial} + \frac{^{238}U}{^{204}Pb}_{today}\left(e^{\lambda^{238}t} - 1\right) \qquad (11)$$

tells us that the lead isotope composition of any geological Pb-poor ore sample analyzed today is the result of an initial amount of Pb (also called initial or common Pb), incorporated by the sample at the moment of its precipitation from the fluid, plus the amount of lead produced by the decay of the parent isotope within the sample until the time of measurement (^{238}U/^{204}Pb$_{today}$($e^{\lambda 238t}$−1): also called radiogenic lead). The isotopic composition of the initial common lead incorporated (^{206}Pb/^{204}Pb$_{initial}$) will be that of the fluid from which the mineral has precipitated. Different Pb-poor ore samples from the same mineral deposit may have different present-day lead isotope compositions, because they incorporated U and Pb in variable proportions, which will result in different present-day isotopic compositions (Eq. (11)), despite having the same initial lead isotope composition, i.e., that of the lead that was carried by an isotopically homogeneous fluid at the time of the ore formation (Fig. 5a). Conversely, they could have not only different present-day lead isotope compositions, but also different initial lead isotope compositions if the fluid that precipitated these minerals was isotopically not homogeneous (Fig. 5b). It is therefore essential to correct the measured isotope compositions of Pb-poor ore minerals by removing the radiogenic lead that has formed after the precipitation of the mineral itself to give sound interpretations to the lead isotope data (Fig. 5).

Luckily, many Pb-poor ore minerals are sulfides and/or sulfosalts (e.g., pyrite, chalcopyrite, pyrrhotite, tetrahedrite, arsenopyrite) that incorporate Pb in much higher amounts than radioactive parents (U and Th). Fig. 6 shows simulations of the amount of correction that is required for typical Pb-poor sulfides, which may contain Pb at ppm level and U at ppb level. It is evident that for Pb-poor sulfides up to 100 Ma old the correction is insignificant even for relatively elevated μ (^{238}U/^{204}Pb) values (up to 2), but for increasingly older ages the correction becomes significant depending on the U/Pb of the mineral. Therefore, for these older Pb-poor samples (>100 Ma old) it would be safer to apply a correction for time-integrated decays of U and Th. This requires knowledge of the age of the mineralization, measurement of the U, Th and Pb concentrations of the ore sample and the assumption of a closed

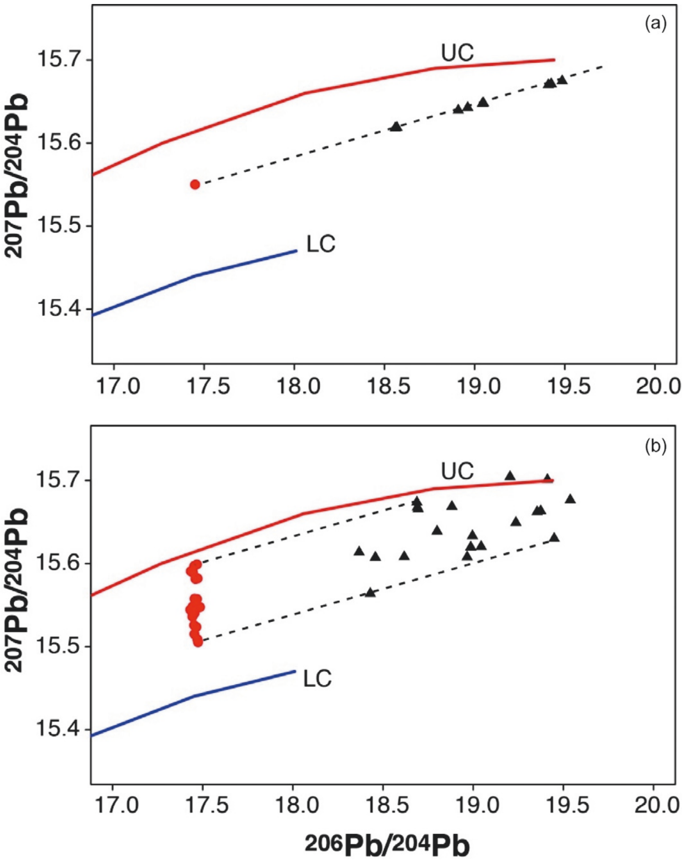

Fig. 5 Examples of the effects of in situ growth of radiogenic ^{206}Pb and ^{207}Pb in minerals (black triangles) with an initial same isotopic composition (red circle in a) and initial different compositions (red circles in b). The examples correspond to radiogenic growth during 650 Myr and for μ values ranging randomly ($N = 20$) between 8 and 20. UC = Upper Crust; LC = Lower Crust.

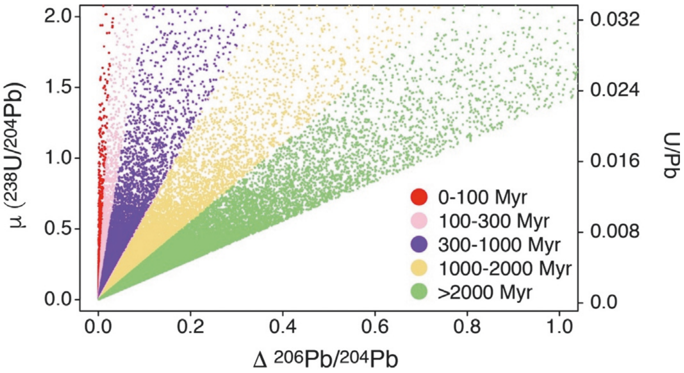

Fig. 6 Simulations of the amount of correction for growth of radiogenic ^{206}Pb depending on age and μ values. The simulations show that for up to 100 Myr old samples with μ values up to 2 a correction for in situ growth of radiogenic ^{206}Pb (from ^{238}U) is not necessary. However, corrections are needed for older ages depending on the μ values of the samples.

system. It is important to notice that Pb-poor ore minerals may sometimes contain microinclusions of U-rich minerals that can result in extremely radiogenic bulk-mineral Pb isotope compositions. This could be the cause of the very radiogenic Pb isotope compositions of sulfides and Fe-oxides associated with IOCG-type mineralization (e.g., Requia et al., 2003).

Once the initial Pb isotope compositions of the minerals have been obtained by either one of the two methods above, these will correspond to the isotope compositions of the fluid from which those minerals have been precipitated because there is no quantifiable fractionation between fluid and mineral for radiogenic isotopes (see above). These isotope compositions can therefore be used for metallogenetic interpretations.

Three end-member situations may occur regarding the topological distribution of lead isotope compositions of ore samples from the same deposit, from the same mineral district, or at the regional scale, in the 2-dimensional Pb isotope spaces (^{208}Pb/^{204}Pb-^{206}Pb/^{204}Pb and ^{207}Pb/^{204}Pb-^{206}Pb/^{204}Pb):

1. Ore samples have homogeneous Pb isotope compositions (within analytical uncertainty or slightly beyond) clustering in a narrow bivariate isotope space field.
2. Ore samples have heterogeneous Pb isotope compositions (well beyond analytical uncertainty) and define linear arrays in bivariate isotope spaces.
3. Ore samples have heterogeneous Pb isotope compositions (well beyond analytical uncertainty) with a distribution that can be enclosed into a polygonal space in bivariate plots.

These topological arrangements correspond to distinct situations to which a general metallogenetic explanation can be attached. Let us examine them separately, considering, for the sake of simplicity, only the uranogenic 2-dimensional plot (^{207}Pb/^{204}Pb-^{206}Pb/^{204}Pb).

Homogeneous Pb isotope compositions

When a representative number of samples from the same mineral deposit, district or at the regional scale have the same or very similar isotopic compositions this implies that the fluid that precipitated the ore was isotopically homogeneous. However, isotopic compositions of ore minerals alone do not allow us to further our understanding of the potential lithological sources and the fluid-rock interactions in the hydrothermal plumbing system. To do so we need the additional analysis of potential source rocks (i.e., magmatic, sedimentary, metamorphic) in the area of the deposit, in order to compare their isotopic compositions with those of the ores.

Different from sulfide and sulfosalts, the U/Pb and Th/Pb ratios in rocks are much higher (in most cases $\mu > 8$) and therefore isotopic compositions of all rocks of non-0 age should be corrected for time-integrated decay of U and Th at the time of ore formation in order to be comparable with the ore. This is especially true for magmatic rocks, because magmatic fluids have the same radiogenic isotope composition as the magma from which they have exsolved at the time of magma crystallization. In the case of fluids leaching rocks, the situation may be more complex, because radiogenic and common lead in rocks behave differently during leaching, depending on the mineralogy of the rock (Chiaradia and Fontboté, 2003). This may result in more complex isotopic systematics of the leached fraction of the rocks that do not correspond to their time-corrected values at the age of the mineralization (see Chiaradia and Fontboté, 2003, for a discussion on this matter).

If the homogeneous Pb isotope composition of the ores falls within the isotopic field of one of the lithologies of the area (or its leachates) then it is likely that the Pb contained in the fluid was derived entirely from that lithology (Fig. 7a). Of course, this interpretation must be done in the light of the knowledge of the type of the mineral deposit (see examples below). If the homogeneous ore isotopic composition falls between two potential end-member sources (Fig. 7b), or within a triangle or even polygon defined by three or more potential sources (Fig. 7c), then it is likely that ore lead is the result of homogenized mixing in fixed proportions of those 2, 3 or more potential sources. Homogeneous ore isotopic compositions could also result from the fact that the potential source rocks have identical (Fig. 7d) or very similar (Fig. 7e–f) isotopic compositions. Simple 2- and 3-end-member mixing equations can be used to quantify the proportions of Pb contributed from each source. The Pb isotope system allows quantification of up to 4 different potential sources (A, B, C, D) because of its 3 radiogenic isotopes, which result in three independent isotope mixing equations

$$\frac{^{206}Pb}{^{204}Pb}_{mix} = \frac{^{206}Pb}{^{204}Pb}_{A} + \frac{^{206}Pb}{^{204}Pb}_{B} + \frac{^{206}Pb}{^{204}Pb}_{C} + \frac{^{206}Pb}{^{204}Pb}_{D} \tag{12}$$

$$\frac{^{207}Pb}{^{204}Pb}_{mix} = \frac{^{207}Pb}{^{204}Pb}_{A} + \frac{^{207}Pb}{^{204}Pb}_{B} + \frac{^{207}Pb}{^{204}Pb}_{C} + \frac{^{207}Pb}{^{204}Pb}_{D} \tag{13}$$

$$\frac{^{208}Pb}{^{204}Pb}_{mix} = \frac{^{208}Pb}{^{204}Pb}_{A} + \frac{^{208}Pb}{^{204}Pb}_{B} + \frac{^{208}Pb}{^{204}Pb}_{C} + \frac{^{208}Pb}{^{204}Pb}_{D} \tag{14}$$

and a fourth one

$$A + B + C + D = 1 \tag{15}$$

which is the mass balance equation of the 4 different sources, where A, B, C, D are the fractional Pb contributions of each source (i.e., we have a system of 4 independent equations that allows its solution for 4 unknowns). In comparison, Os, Sr, Nd and Hf isotope systems, having just one radiogenic isotope, allow the quantification of mixing between only two sources.

From a hydrothermal plumbing or fluid-rock interaction perspective, homogeneous Pb isotope compositions suggest different possible scenarios: (i) the fluid has not interacted significantly with rocks outside its isotopically homogeneous source region because the precipitation site was very close to or even within the source region (Figs. 3 and 7a); (ii) all rocks involved in the ore process had very similar isotopic compositions (Figs. 3 and 7d–f); (iii) the rocks with which the hydrothermal fluid interacted outside its source region had very low Pb contents compared to the source, so that even if they were more or less heavily leached by

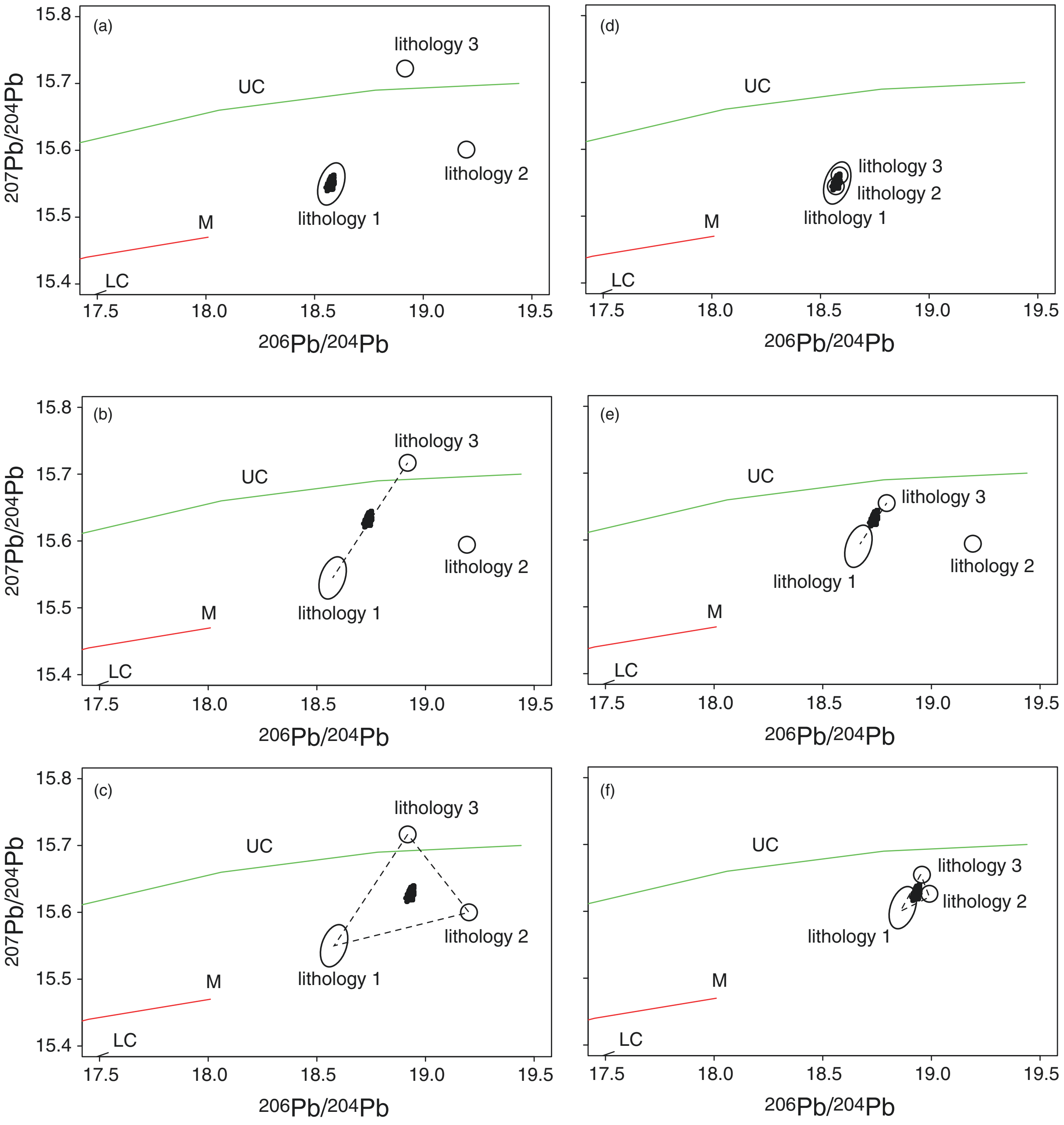

Fig. 7 Hypothetic examples of possible interpretations of the geological meaning of homogeneous Pb isotope compositions of ores (black dots) from a mineralization compared to hypothetic lithologies (1, 2, 3) occurring in the area of the mineralization. In (a) the ore Pb isotope composition overlaps the compositional field of lithology 1 suggesting that all Pb could be sourced from this lithology. In (b) ore Pb falls on a line joining lithologies 1 and 3 suggesting that it could be the result of a homogeneous mixture of Pb from isotopically different leads of the two lithologies. In (c) ore lead is comprised within a triangle having as apexes the three lithologies suggesting the it could be the result of homogeneous mixing of isotopically different leads from the three lithologies. Panels (d), (e), (f) show the same situations for lithologies 1, 2, 3 that are isotopically very similar.

the fluid they could not contribute any significant Pb (Figs. 3 and 7a); (iv) the fluid of the source region did not carry significant Pb and all Pb present in the ore minerals was inherited from the isotopically homogeneous rock along the flow path and/or at the precipitation site (Figs. 3 and 7a); (v) fluids from isotopically different sources and or interacting with isotopically different lithologies along their paths have been efficiently homogenized through some process before the ore precipitation (Figs. 3 and 7b and c). It is clear that a multi-isotope approach, i.e., combining radiogenic with light and heavy element stable isotopes, would allow us to further narrow down the different possible scenarios above and to develop a more realistic model.

Heterogeneous Pb isotope compositions

When lead isotope compositions of ore samples of a deposit (or also of different deposits at the district or regional scales) are heterogeneous and define linear trends in the isotope space (Fig. 8a) this means that they are the result of mixing between two relatively homogeneous sources (although another possibility is that they correspond to secondary isochrons defined by the Pb isotope evolution of a single source: see below). Cloudy distributions indicate variable contributions from three or more isotopically distinct sources (Fig. 8b and c). Also in this case the proportions of lead from the two (or more, up to four) sources can be quantified and will be different from sample to sample, opposite to the case above of a homogeneous mixing between two or more sources.

From the perspective of the hydrothermal plumbing system and fluid-rock interaction, this topological configuration tells us that fluid homogenization was incomplete at the mineral, deposit, district or regional scale, depending on the scale of sampling. This

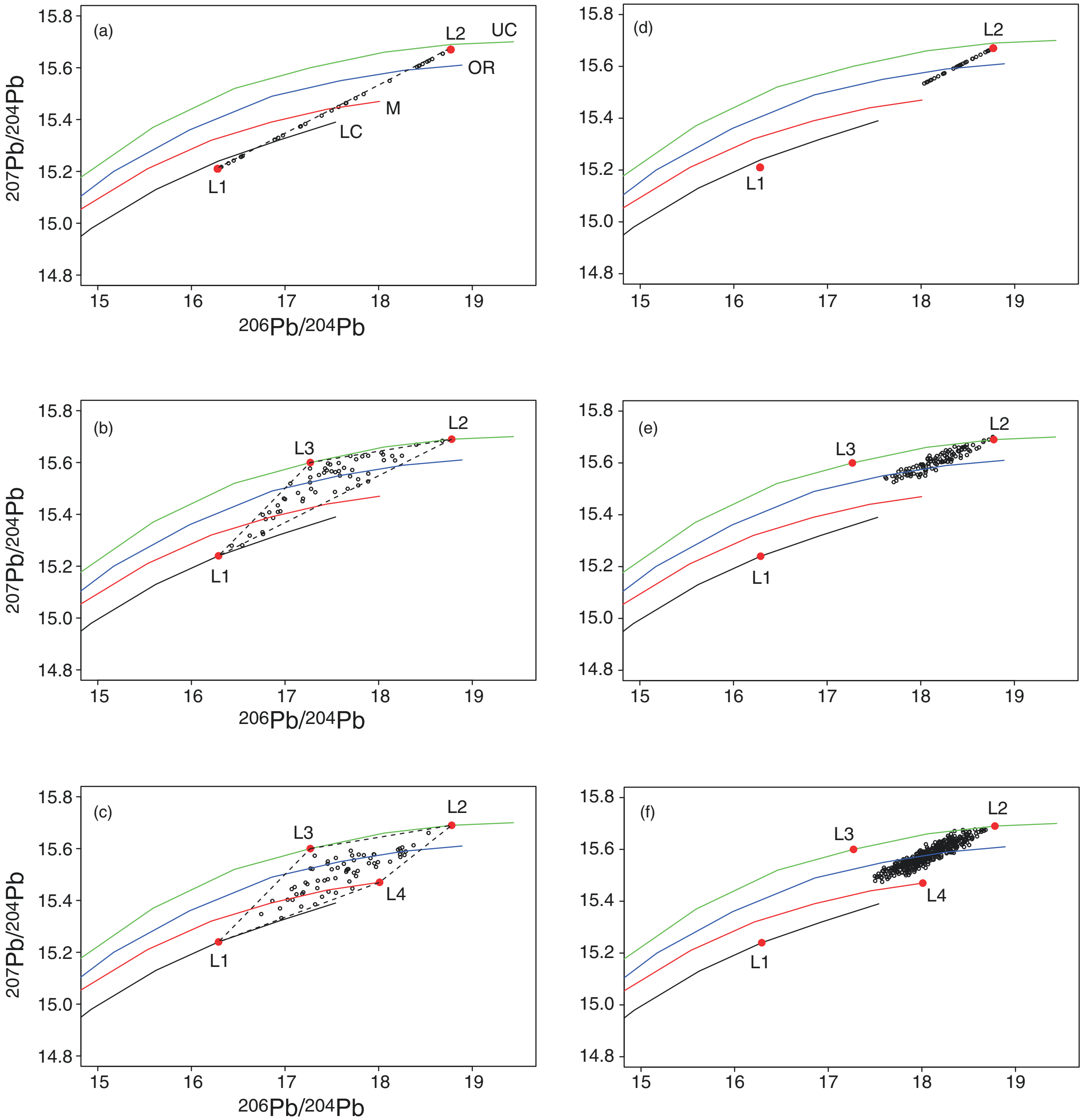

Fig. 8 Examples of heterogeneous Pb isotope signatures of ore samples from a hypothetic mineralization. In (a), (b) and (c) ore samples are the result of binary, ternary and quaternary mixing of lithologies L1, L2, L3 and L4 (red circles), with random potential contributions between 0% and 100% for each source. In (d), (e) and (f) ore samples are the result of binary, ternary and quaternary mixing of lithologies L1, L2, L3 and L4 (red circles), with random potential contributions between 0 and 100% for L2 and between 0 and 30% for L1, L3 and L4. Evolution curves for Upper Crust (UC), Orogen (OR), Mantle (M) and Lower Crust (LC) are from Zartman and Doe (1981).

requires, therefore, specific conditions in the hydrothermal plumbing and/or fluid-rock interaction processes. The differences in isotopic compositions and, therefore, in proportions of lead contributed from the two (or more) sources in relation with the spatial distribution of the samples and/or with their temporal position in the paragenetic sequence may reveal patterns of fluid flow and/or fluid-rock interactions changing through space and/or time that will help to understand the causes of the incomplete mixing. The end points of these mixing trends do not necessarily correspond to the isotopic compositions of the source rocks. Fig. 8d–f illustrate cases in which the contributions from one or more of the potential sources are subordinate, due to a lower fluid interaction with these rocks or to their lower Pb content. In such cases the mixing trends do not cover the entire isotopic variability defined by the sources. These examples show the importance of the measurement of the isotopic compositions of potential source rocks associated with a mineral deposit to quantify fluid-rock interactions and the contributions from different sources. Below we illustrate some conceptual and real examples that correspond to homogeneous and heterogeneous Pb isotope compositions for different types of mineralization, namely porphyry systems, VHMS deposits, stratiform Cu deposits and MVT deposits and complement the discussion with information derived from light stable isotopes.

Porphyry systems

Porphyry systems include different types of mineralization distributed within and around the shallow (1–6 km depth) porphyry intrusive complex associated with deeper (5–15 km depth) parental magma chamber at convergent margins (Sillitoe, 2010). The mineralization types include porphyry deposits, high- and intermediate-sulfidation epithermal deposits, skarn, carbonate replacement deposits, sediment-hosted Au deposits at increasing lateral distances from the porphyry fingers and high- to intermediate sulfidation deposits above the porphyry complex at shallower levels than the porphyry deposit mineralization (Fig. 9). Low-sulfidation epithermal deposits could also be inserted in this model, at greater distance from the magmatic source (Fig. 9; e.g., Hedenquist et al., 2000), although porphyry systems form preferentially in compressive settings whereas low-sulfidation epithermal deposits form preferentially in extensional settings, resulting in the rare spatial and temporal coexistence of the two mineralization styles (Cooke and Simmons, 2000).

In the porphyry metallogenetic environment there are two main types of fluids: magmatic fluids (green arrows in Fig. 9), emanating from the cooling parental magma chamber and transferred through the porphyry complex into the adjacent wall rocks, as well as non-magmatic fluids, circulating through the wall rocks but also infiltrating and exchanging with the magmatic rocks and fluids (blue arrows in Fig. 9). The non-magmatic fluids may be chemically and isotopically different from the magmatic ones, as they have fully or partially equilibrated with rocks that can be variably older and lithologically (and therefore also isotopically) different from the intruding magma. In porphyry systems such non-magmatic hydrothermal fluids are in most cases chemically and isotopically exchanged meteoric fluids (e.g., Sillitoe, 2010). However, depending on the location and emplacement depth, basinal brines, and/or also metamorphic fluids derived from dehydration or decarbonatization of the country rocks hosting the intrusion, either during contact metamorphism related to skarn formation and/or regional metamorphism, may also be important (Shanks III, 2014). As all these fluids have distinct hydrogen and oxygen isotope compositions (e.g., Sheppard, 1986), measurements of the stable isotope compositions of H- and O-bearing gangue and, more rarely, ore minerals (e.g., oxides, hydroxides) are commonly used to estimate the origin of the fluids responsible for ore and associated gangue mineralization (c.f., Ohmoto, 1986, Taylor Jr, 1974, 1997; Shanks III, 2014).

The sketch of Fig. 9 highlights the spatial difference of the dominant fluid type within porphyry systems, i.e., dominant magmatic fluid in the deposit types formed close to the porphyry complex (proximal positions) and increasing contributions from non-magmatic fluid in the deposit types formed at farther distances from the porphyry complex (distal positions). However, we must also consider the change in fluid proportions during the lifetime of the porphyry systems. Magmatic fluids occur for geologically short-lived periods because they are associated with the relatively rapid saturation and cooling of a magmatic pulse. In contrast, external, non-magmatic fluids may have much longer lifetimes. This results in fluctuating proportions of magmatic to non-magmatic fluids in various positions of porphyry systems, with an overall increasing contribution of non-magmatic fluids, even in proximal positions, in the late stages of the mineralization, when the magmatic pulses and the associated magmatic fluids wane out. Li et al. (2018), using in situ O isotopes on quartz (measured by SIMS), have shown a fluctuating proportion of magmatic to non-magmatic fluids in the porphyry Cu—Mo deposit of Qulong (Tibet, China) through time, reflecting the pulsed nature of the magmatic fluid which, during the waning stage, is overtaken by the meteoric fluid.

The sketch of Fig. 9 shows that porphyry Cu—Mo—Au deposits, proximal skarn deposits and high-sulfidation lode Cu—Au deposits are formed close to the magmatic system, i.e., they are formed by dominant magmatic fluids (fluid paths 1, 2), except, possibly, for the late waning stages of magmatic activity, as discussed above. It can be expected that the Pb isotope composition of these deposits, considering the relatively elevated Pb contents of magmatic-derived fluids in the porphyry environment (Kouzmanov and Pokrovski, 2012) and the relatively high-temperature deposition of ore minerals (i.e., from dominant magmatic fluids during the early-middle stages of the mineralization), will coincide with that of the magmas associated with the mineralizing system. Therefore, these deposits should correspond to the Pb isotopic topology of Fig. 7a above, in which lithology 1 is the magma. This is supported by various lead isotope studies that have been carried out on porphyry systems of the Andes, e.g., El Salvador (Zentilli et al., 1988; Tosdal et al., 1995) and Rio Blanco-Los Bronces (Tilton et al., 1981; Tosdal and Munizaga, 2003; Kurtz et al., 1997), which are characterized by homogeneous Pb isotope signatures coinciding with those of the associated magmatic rocks (see summary in Tosdal et al., 1999). Field et al. (2005) and Rye (2005) concluded that also the range of sulfur isotope compositions of sulfide minerals is largely compatible with a magmatic origin of the sulfur in porphyry systems.

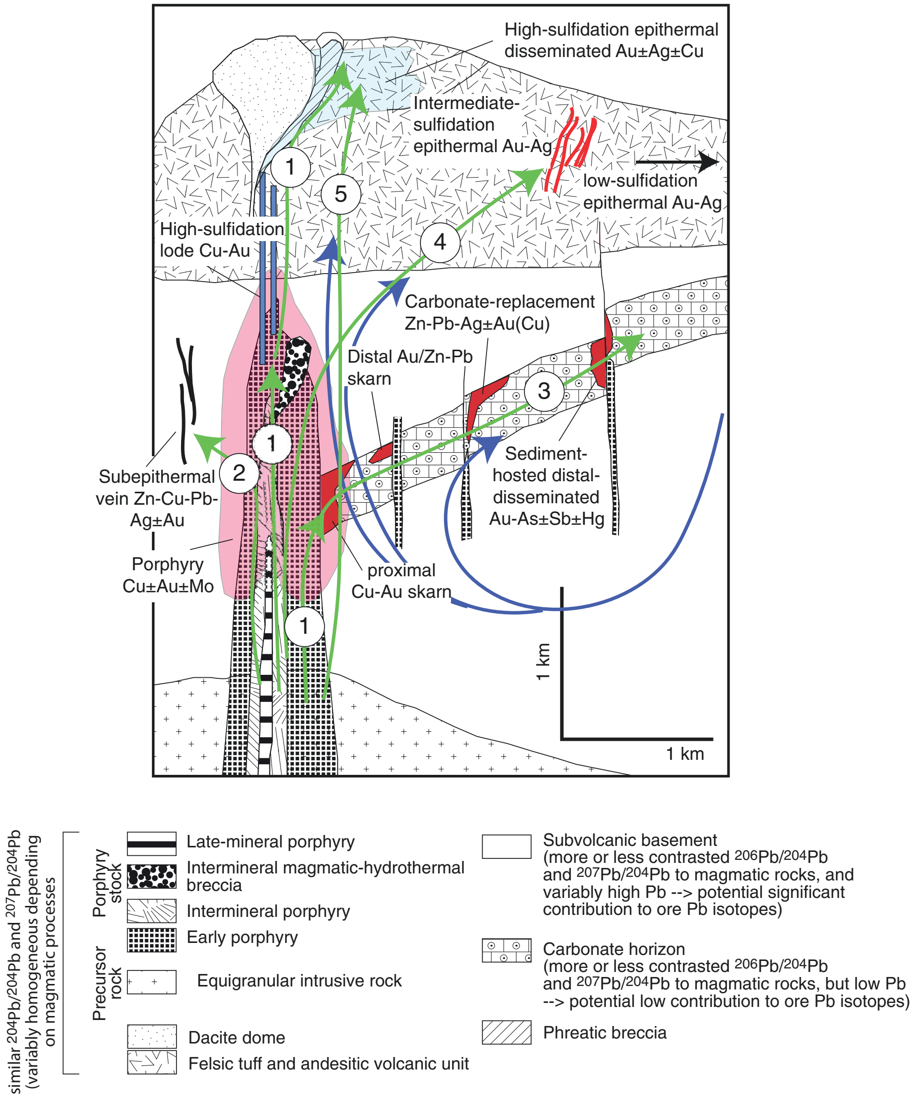

Fig. 9 Schematic model of a porphyry system, showing different mineralization styles occurring in this environment. The blue and green arrows illustrate possible paths of magmatic (green) and non-magmatic (blue) fluids. The circled numbers correspond to scenarios discussed in the text. Modified from Sillitoe RH (2010) Porphyry copper systems. *Economic Geology* **105**: 3–41.

The isotopic compositions of the magmas may be more or less homogeneous depending on the petrogenetic processes that usually consist of the interaction of mantle-derived magmas with crustal rocks in a subduction-related environment. Therefore, an accurate petrological, geochemical and isotopic study of the magmatic rocks (also including Sr, Nd and Hf isotopes) can provide additional constraints on the metallogenetic processes in porphyry systems. In particular, radiogenic isotope studies of magmatic rocks associated with porphyry systems may help us to evaluate the importance of continental or oceanic crust assimilation by the magmas (e.g., Chiaradia et al., 2009; Chiaradia and Fontboté, 2001; Chiaradia, 2009) and subducted sediment incorporation in the mantle source (Sillitoe and Hart, 1984; Chiaradia and Fontboté, 2001; Chiaradia, 2009). Besides the conventional light stable isotope compositions, studies of other transition metal stable isotopes on magmatic rocks potentially associated with porphyry systems could also be of potential interest (e.g., Wang et al., 2021a, 2021b; see also the section on transition metal stable isotopes).

High-sulfidation epithermal disseminated Au—Ag—Cu deposits, formed more distally to the porphyry complex, may also be characterized by homogeneous, dominantly magmatic, Pb isotope compositions as highlighted by the path of fluids forming these deposits that occurs mostly if not entirely within magmatic rocks associated with the mineralizing system (fluid path 1 in Fig. 9). For instance, both Pb- and S-isotope compositions for the enigmatic El Mochito (Honduras) epithermal carbonate replacement Zn-Pb ± Ag skarn deposit support a magmatic origin for both S and Pb, despite the fact that there is no known igneous intrusion in the vicinity of this mineral deposit (Ault and Williams-Jones, 2004). The ore mineralization at El Mochito is structurally controlled, occurring together with garnet and pyroxene skarns, as a high temperature Pb—Zn mineralization along faults or lithologic boundaries between shales and carbonates (Vazquez et al., 1998). Because the Pb-isotope compositions of the sulfide ore, as well as that of the recrystallized wall-rock limestones, are very similar to those of nearby ignimbrites, it is proposed that the intrusive equivalent of these ignimbrites ultimately represents the magmatic source of the metals and also of the sulfur. The C- and O-isotope compositions of the carbonates, which are strongly zoned towards the ore mineralization, together with the garnet and pyroxene O-isotope compositions, as well as the H- and O-isotope compositions of fluid inclusions within sulfides and garnet, support mixed meteoric-magmatic fluids as the transporting solutions for the ore minerals (Vazquez et al., 1998).

Mineral deposits of the porphyry systems that are increasingly distal and lateral with respect to the mineralizing magmatic system (e.g., distal skarns, carbonate-replacement, sediment-hosted distal disseminated, intermediate sulfidation epithermal deposits: fluid paths 3, 4, 5 in Fig. 9) as well as low-sulfidation epithermal deposits are generally characterized by a decreasing contribution of magmatic fluid and an increasing proportion of non-magmatic fluids. This is commonly best characterized by conventional stable isotope measurements of ore and gangue minerals and their included fluids (Shanks III, 2014), which often indicate the presence of significant amounts of meteoric fluids in the more distal parts and/or the later stages of ore mineralization (Sillitoe, 2010; Taylor Jr, 1997; Shanks III, 2014). Both the S and the O-isotope composition of sulfates, often present in the later stages of mineralization, also suggest crustal sulfur sources with higher values of $\delta^{34}S$. This may either reflect assimilation of wall rocks having higher but diverse $\delta^{34}S$ values in sulfide or sulfates, or a post-magmatic origin for the late-stage sulfate mineralization crystallizing in the presence of meteoric fluids (see also Field and Gustafson, 1976; Bowman et al., 1987; Vennemann et al., 1993; Ohmoto and Goldhaber, 1997; Ault and Williams-Jones, 2004; Field et al., 2005; Shanks III, 2014). The H- and O-isotope compositions thus suggest that late-stage, meteoric fluids may often recrystallize pre-existing ore mineralization, resetting the gangue minerals and refocusing the ore mineralization in porphyry systems, albeit meteoric water is not necessarily introducing new metals to the ore (Sillitoe, 2010).

In the distal positions of the porphyry system (Fig. 9), the ore Pb compositions may deviate more or less significantly from the magmatic composition depending on the Pb isotope and Pb content contrast between magma (supplier of the Pb to the magmatic fluid) and host rocks (suppliers of Pb to the meteoric and/or basinal fluids) (Fig. 9). Additionally, even if these deposits were dominated by a magmatic fluid, the latter unavoidably interacts with host rocks before reaching the distal sites of metal deposition and may therefore leach variable amounts of non-magmatic lead depending on the paths followed and the geological environment of the deposit (see Ault and Williams-Jones, 2004 in the case of a Pb—Zn carbonate replacement skarn). Therefore, these deposits may be characterized by heterogeneous isotopic compositions following linear trends (2-end member mixing: Fig. 8a and d) or cloudy distributions (3 or more end-member mixing: Fig. 8b, c, e and f).

The different degrees of mixing illustrated by the different isotopic compositions of samples from the mineralization in Fig. 8 could correspond to different spatial positions of the samples within the deposit (e.g., more proximal or distal, reflecting different degrees of magmatic fluid-host rock interaction and/or different degrees of mixing between magmatic and meteoric fluids). However, they could also be related to samples belonging to different periods of mineralization within the paragenetic sequence. Under this point of view, ore minerals may be characterized by different proportions of magmatic versus non-magmatic lead through time, as well as gangue minerals (e.g., quartz) may be precipitated by fluctuating proportions of magmatic and non-magmatic fluids as inferred from O isotopes (see above). For instance, an increase of the non-magmatic Pb component could occur in the final stages of the mineralization when a thermal collapse of the magmatic-hydrothermal system occurs, or in the very initial stages when magmatic fluids have not yet been exsolved and the only fluid present is the meteoric fluid in the wall rock lithologies, or be cyclic (see above). Another possible scenario is that there is an increase of the magmatic Pb contribution through time if the magmatic fluid follows a path in which its contact with the non-magmatic host rock has been sheltered by an alteration halo formed by previous passages of the magmatic fluid (Fig. 10).

There are several examples in the literature of heterogeneous Pb isotope signatures in more or less distal mineralization types of the porphyry system and in low-sulfidation epithermal deposits (Richards et al., 1991, see also Richards and Noble, 1998) that imply a mixing between magmatic and non-magmatic (host rocks) Pb sources. Tosdal et al. (1999), for instance, highlight that ore minerals of the Bagdad porphyry Cu—Mo deposit (Arizona) display isotopic differences depending on their occurrence within broadly *syn*-mineral granitoid magmatic rocks ($^{206}Pb/^{204}Pb = 18.40–18.51$) or in Proterozoic host rocks ($^{206}Pb/^{204}Pb = 18.58–20.0$). Peripheral deposits of the same system display also more radiogenic signatures ($^{206}Pb/^{204}Pb = 18.80–18.95$) than the granitoid-hosted ones. In this case the isotopic differences are enhanced by the strong isotopic contrast between Cretaceous magmatic Pb ($^{206}Pb/^{204}Pb \sim 18.4–18.5$) and significantly more radiogenic Pb of Proterozoic host rocks ($^{206}Pb/^{204}Pb = 19.21–20.16$). This is in contrast with the above mentioned homogeneous and entirely magmatic signatures of giant porphyry deposits of the Andes (El Salvador, Rio Blanco-Los Bronces). One may raise the question whether an external (host rock) contribution of Pb in the latter deposits could have been masked by the fact that host lithologies are magmatic rocks broadly coeval with the deposit formations and therefore of very similar isotopic compositions to that of the magmatic rocks associated with the mineral deposit (e.g., Fig. 7d–f).

Another example is provided by Pb isotope compositions of pyrites and galenas from the Miocene high-sulfidation epithermal deposit of Yanacocha, Peru (Merino, 2009). Despite the dominant magmatic origin of fluids in high-sulfidation mineralization types (Hedenquist, 1987), a part of the Yanacocha ore minerals displays Pb isotope signatures suggesting mixing of magmatic Pb and Pb leached by the (magmatic?-)hydrothermal fluids from Cretaceous and/or Paleozoic basement rocks (Fig. 11). Light stable isotopes would be useful in this case to elucidate whether dominant magmatic fluids leached Pb from Cretaceous and/or Paleozoic basement rocks or whether magmatic fluids mixed with non-magmatic fluids equilibrated with those host rocks.

Another approach in porphyry system studies is the analysis of Pb (and Sr as well as Cl) isotopes in fluid inclusions from hydrothermal quartz associated with ore minerals, using the bulk crush-leach method (e.g., Pérez, 2012; Rottier, 2017).

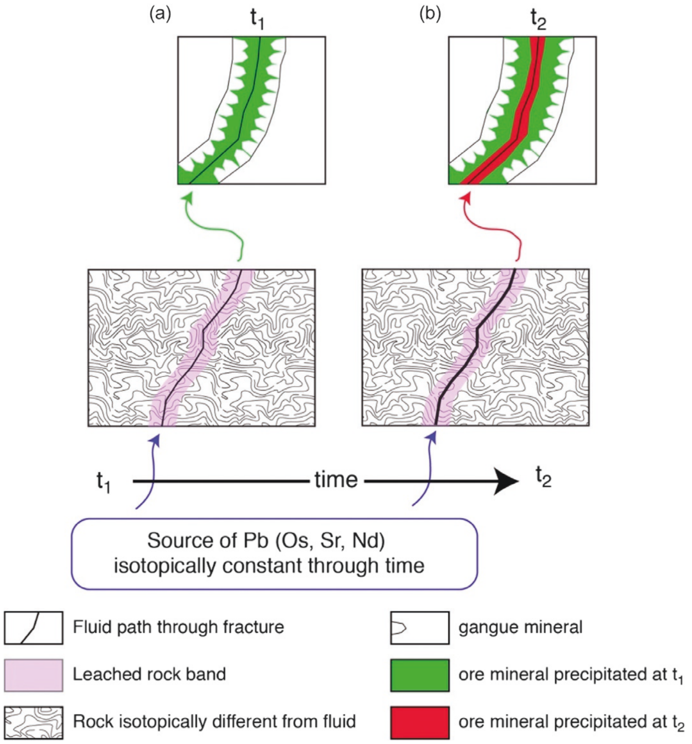

Fig. 10 Schematic representation of a fluid flowing through a rock that is isotopically different from the fluid itself. The t1 and t2 stages represent subsequent events of mineral deposition. Ore minerals deposited during t1 (a) may be more affected by the fluid-rock interaction with respect to ore minerals deposited during t2 (b), because in the latter case the fluid is sheltered from significant interaction with the host rock by the reaction bands formed during the previous t1 fluid flow event.

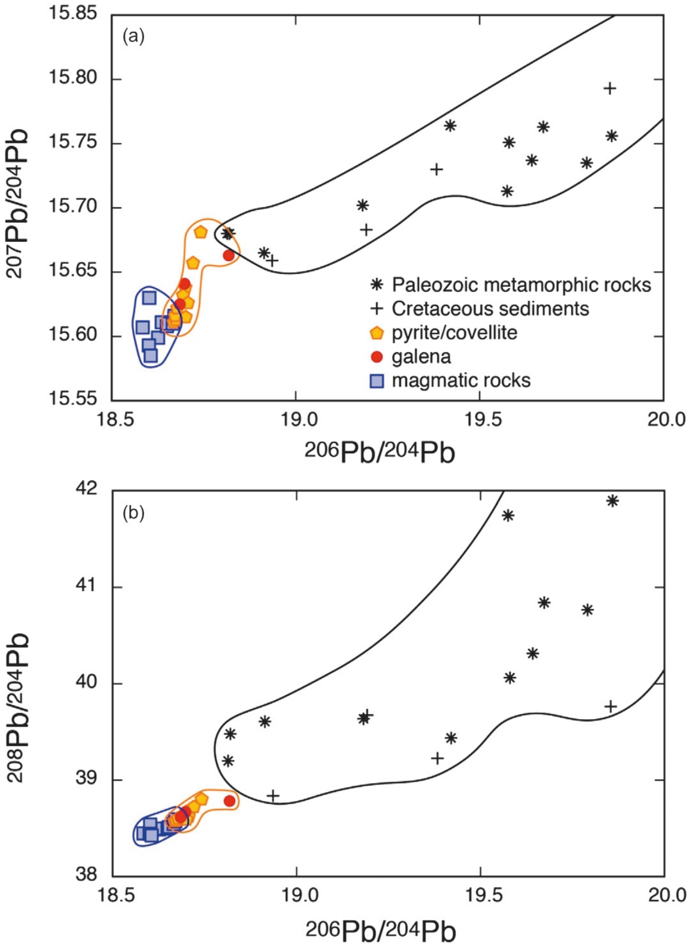

Fig. 11 Lead isotope compositions of ore minerals, magmatic rocks and basement rocks from the Yanacocha high-sulfidation epithermal gold deposit (Northern Peru). *Data from Merino ND (2009) Petrology, geochemistry and geochronology of intrusive rocks from the Yanacocha gold district, Northern Peru (Unpublished MSc. Thesis). pp. 1–136, University of Geneva, Switzerland.*

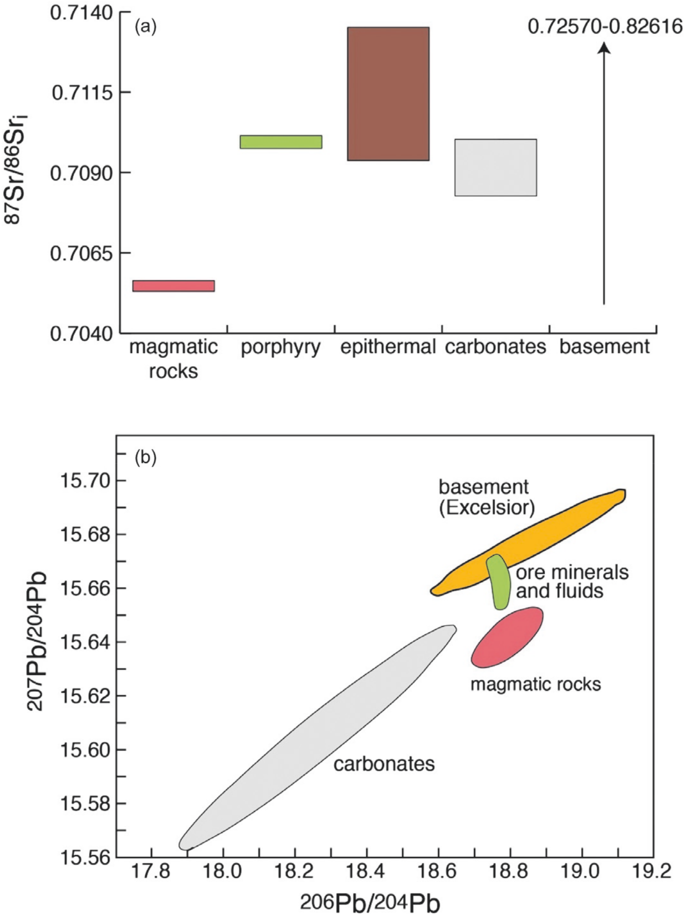

Fig. 12 Sr and Pb isotope compositions of hydrothermal fluids of Cerro de Pasco mineralization (Central Peru) from quartz crush-leach compared to those of ore minerals, magmatic rocks, carbonate rocks and basement rocks of the area. Data from Rottier (2017).

Interestingly, these studies show that initial Sr isotope compositions of many fluid inclusions are more radiogenic than those of the associated magmatic rocks. Rottier (2017) measured fluid inclusions in quartz from both the porphyry Cu—Mo veins and from the epithermal mineralization of the giant porphyry-related epithermal polymetallic deposits of Cerro de Pasco (Peru). Age-corrected $^{87}Sr/^{86}Sr$ values of fluids in both the porphyry Cu—Mo veins and in the epithermal mineralization are significantly more radiogenic (0.70937–0.71352) than those of the magmatic rocks associated with the mineralization (0.70530–0.70564) and also than those of host carbonate rocks (0.70827–0.71003) (Fig. 12a). The fluids from the porphyry Cu—Mo veins (0.70975–0.71015) are slightly less radiogenic than those associated with the epithermal mineralization (0.70937–0.71352). This suggests that radiogenic Sr must have been leached by magmatic fluids from host rocks, e.g., Mitu sandstone (0.72570) or Excelsior shale and phyllite (0.75564–0.82616), somewhere deeper in the system. Similarly, in a study of bulk fluid inclusions from 4 porphyry deposits of the Andean Cordillera (Llurimagua, Ecuador; Toromocho and Antapaccay, Peru; Chuquicamata, Chile), Pérez (2012) found that Toromocho and Llurimagua were characterized by hydrothermal fluids with more radiogenic Sr than the associated magmatic rocks.

In contrast, Pb isotope compositions of the fluids in the Cerro de Pasco deposits (Rottier, 2017) are similar to those of magmatic rocks in terms of $^{206}Pb/^{204}Pb$ values, though slightly more radiogenic in terms of $^{207}Pb/^{204}Pb$ (Fig. 12b) and $^{208}Pb/^{204}Pb$ compositions. Fluid Pb isotope compositions are nonetheless similar to those of sulfide minerals from the same deposit (Fig. 12b). This suggests that also Pb isotopes record a non-magmatic Pb signature in the hydrothermal fluids and minerals, despite in apparently lower proportions compared to the Sr isotope system. This is probably related to the different isotopic and concentration contrasts between magmatic and host rocks for the Pb and Sr isotope systems.

The above examples illustrate that lead (and other elements) isotope heterogeneities in porphyry systems depend on two main factors: (i) contrasting Pb concentrations of the contributing sources (Fig. 8a–c vs. Fig. 8d–f), and (ii) contrasting Pb isotope signatures of the sources (cf., Fig. 7 and Fig. 8). The larger is the isotopic contrast and the lesser is the concentration contrast the more evident will be the contributions from different sources (Fig. 8a–c vs. Fig. 8d–f).

Volcanic-hosted massive sulfide (VHMS) deposits

VHMS deposits are strata-bound submarine deposits that constitute significant sources of base metals (Cu, Pb, Zn) and sometimes also of precious metals (Au, Ag). Their formation requires four main "ingredients" (Fig. 13a): (i) seawater; (ii) a magmatic heat

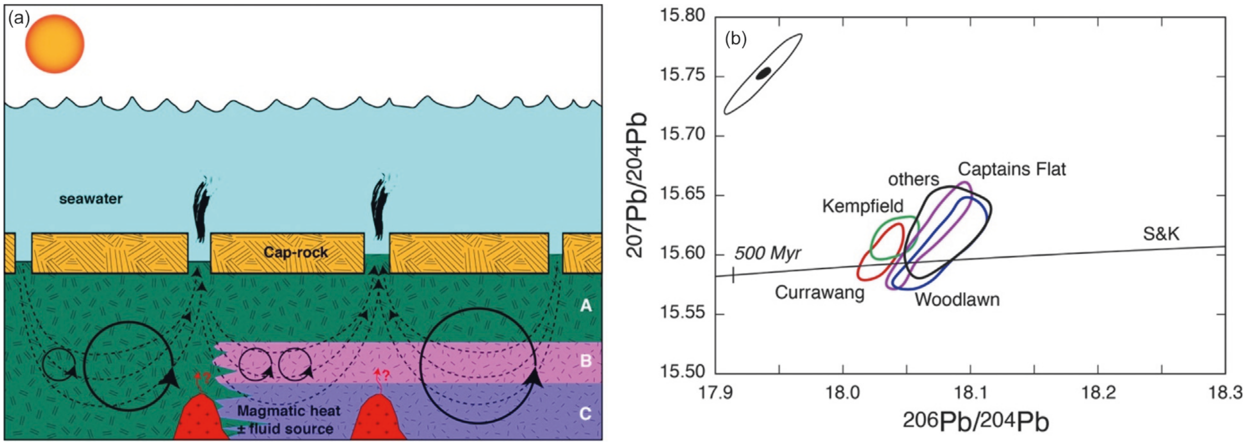

Fig. 13 Schematic model (a) of a VHMS system. The scheme illustrates two different situations: on the left modified seawater (black dashed arrows) circulate through and leaches metals from a lithologically and isotopically homogeneous volcanic/volcaniclastic rock (A), whereas to the right they circulate through and leach metals from lithologically and isotopically different volcanic/volcaniclastic rocks (A, B, C). Seawater is heated by sub-seawater surface magma bodies, which may also supply fluid and metals. These magma bodies also drive fluids into convective cells (black circle lines) which may result in variable isotopic homogenization depending on convective cell size. Hydrothermal fluids (modified seawater ± magmatic fluid) eventually exit at the seawater bottom through fractures in the cap rock above the magmatic bodies and deposit metals to form a VHMS deposit. Lead isotope compositions (b) of Paleozoic VHMS deposits of the Lachlan fold belt (Captains Flat-Goulburn Trough, SE Australia). The uncertainty ellipses refer to old data (empty ellipse: data compiled in Carr et al., 1995) and more recent data (black ellipse: data in Huston et al., 2016).

source; (iii) a volcanic-volcaniclastic sequence; (iv) a cap-rock. Seawater enters the volcanic-volcaniclastic sequence through fractures of the cap rock and becomes progressively heated with depth when approaching the magma source. Along its path approaching the magma source the seawater is heated and reacts with the host volcanic-volcaniclastic rocks leaching their metals and becoming progressively more reduced and more saline. Eventually fluids form variably long-lived convective cell systems in which the cap rock acts like the lid of a cooking pot. When fluids ascend to shallow levels, close to the submarine rock-water interface, they precipitate ore minerals due to the large temperature and salinity decrease following their mixing with cold and less saline seawater. The magma is the driving heat engine of the convective system but may also contribute fluid and metals (e.g., Sillitoe et al., 1996; de Ronde et al., 2005, 2011; Piercey, 2011; Martin et al., 2020).

In such metallogenetic environment homogeneous Pb isotope compositions of ore minerals within individual deposits may result from the following processes: (i) the leached volcanic/volcaniclastic sequences belong to the same magmatic episode and therefore are isotopically homogeneous (e.g., Fig. 7d and f), which would correspond to the left-hand part of Fig. 13a; (ii) even if there were some lithological and isotopic differences in the sequence (right-hand part of Fig. 13a), the establishment of long-lived convective cells could homogenize the Pb from isotopically different parts of the sequence (Fig. 7b and c). Nonetheless, more or less heterogeneous Pb isotope compositions could be related to different sizes of the convective cells and/or to lateral and vertical changes in the lithology and thus in their isotopic composition (Fig. 13a). It is evident that, like in the case of porphyry systems, also in this case a complete understanding of the Pb isotope compositions needs the analysis of the various lithologies potentially associated with the mineralizing system.

A typical example of VHMS deposits with relatively homogeneous and similar Pb isotope compositions is that of the Paleozoic Eastern Lachlan fold belt in SE Australia (Gulson, 1986; Carr et al., 1995; Huston et al., 2016) (Fig. 13b). These deposits have quite homogeneous Pb isotope signatures not only at the individual deposit scale but also at the hundreds of km scale of the mineralized belt, suggesting a very similar and homogeneous magmatic Pb source.

Chiaradia and Fontboté (2001) analyzed Pb isotope compositions from three small Paleogene VHMS deposits hosted by the Macuchi arc sequence, in the Western Cordillera of Ecuador. Two deposits (Macuchi and El Patiño) are situated within a few km from each other whereas the third one (La Plata) is situated about 100 km to the NNE within the same Macuchi arc sequence. They found that Pb isotope compositions of the ores within each individual deposit were homogeneous, but that they varied from one deposit to the other (Fig. 14). The Pb isotope compositions of the deposits fall within the field of the variable Pb isotope signatures of the Macuchi volcanic rocks, suggesting derivation of Pb from them. The inter-deposit differences suggest leaching and homogenization of different parts of the isotopically heterogeneous volcanic sequence, in agreement with the different stratigraphic positions of the deposits within the Macuchi arc sequence (Chiaradia and Fontboté, 2001). The Pb isotope compositions of VHMS ore minerals may also offer a way to interpret their paleogeodynamic environment of formation, e.g., island arcs characterized by more radiogenic signatures than the oceanic crust like the Macuchi arc VHMS deposits, or MORB-related VHMS deposits that would be characterized by no input of crustal radiogenic lead (Orgeval et al., 2005).

The stable radiogenic isotopes of Sr and Nd have been measured in ore samples of VHMS deposits of the Iberian pyrite belt (Relvas et al., 2001), where they occur as sub-trace elements, to infer, together with Pb isotopes, multiple sources of metals, a

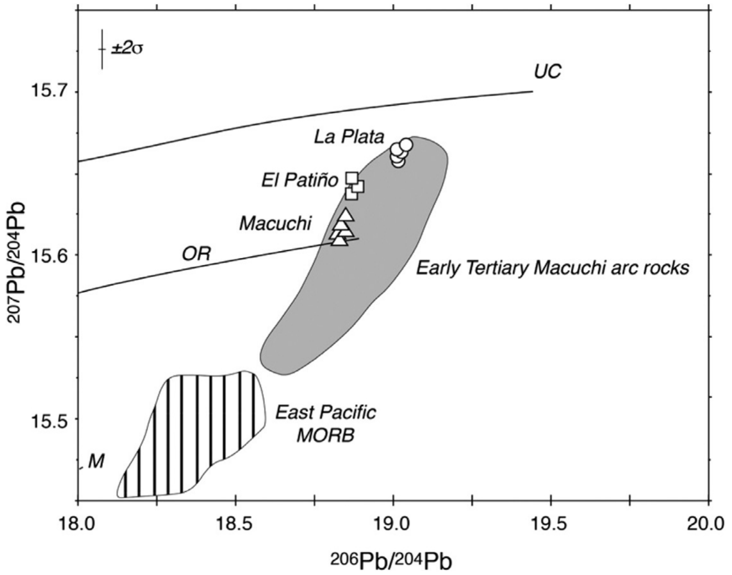

Fig. 14 Lead isotope compositions of VHMS deposits of the Macuchi arc (Western Cordillera of Ecuador) and of the host volcanic rocks. Modified from Chiaradia M and Fontboté L (2001) Radiogenic lead signatures in Au-rich volcanic-hosted massive sulfide ores and associated volcanic rocks of the Early Tertiary Macuchi island arc (Western Cordillera of Ecuador). *Economic Geology* **96**(6): 1361–1378.

conclusion also supported by Os isotope analyzes (Munhá et al., 2005). Reviews on VHMS deposits by Huston (1999) and on recent ore mineralizing hydrothermal systems on the seafloor by Shanks III (2001) have revealed the complexities of such mineralizing systems based on H, C, O, and S stable isotope geochemistry. These studies demonstrated a dominance of seawater or exchanged seawater as the major mineralizing fluid, but with rather large amounts of magmatic-derived sulfur as well as some contributions from bacterial sulfate reduction of seawater sulfate. Additional information on the processes of formation of VHMS deposits could be derived from stable isotope systematics of transition metals (Cu, Fe, Zn), but relatively few studies have been published on this topic so far (see below the section on transition metal stable isotopes).

Sediment-hosted stratiform Cu deposits

Genetic models of sediment-hosted stratiform Cu deposits, such as represented by the classical *Kupferschiefer* deposits in Poland and/or the Earth's largest sediment-hosted Cu ores of the Central African Copper Belt, have evolved from a single-stage, disseminated Cu-sulfide mineralization to a multi-stage ore mineralization. In the latter case, the first stage is followed by subsequent ones of remineralization during diagenesis or even under hydrothermal, metamorphic conditions (e.g., Dewaele et al., 2006; El Desouky et al., 2009, 2010; Hitzman et al., 2010). The large-scale remineralization during *syn*-orogenic metamorphism of the Cu ores of the Central African Copper Belt has questioned the importance of the pre-metamorphic mineralization, implying that the bulk ore mineralization may even be entirely of hydrothermal, metamorphic origin during active deformation and orogenesis. Indeed, a syn-sedimentary or early diagenetic origin for these types of deposits was initially proposed based on large variations in the S-isotope compositions of the Cu-sulfides in these deposits. This range is best explained by Bacterial Sulfate Reduction (BSR) of marine sulfate within the carbonates, shales, and interbedded sandstones, that occurs in response to changing redox conditions occasionally also producing a redox front induced by the presence and relative abundance of organic matter in these types of rocks (Leach et al., 2005; Shanks III, 2014). More recently, Cu isotope compositions of sulfides have indeed confirmed that the range in isotopic composition is clearly related to changes in redox conditions at the depositional site, with important transport of the Cu as chloride and/or sulfide complexes for the classic *Kupferschiefer* deposits and in other stratiform sedimentary Cu deposits (Asael et al., 2009, 2012; see also the section on Cu isotopes below). However, Pb isotope compositions allow for the introduction of Pb from crystalline country rocks (Fig. 15). Similarly, Re—Os dating of the disseminated Cu-sulfides in the metamorphosed Central African Copper Belt (Muchez et al., 2015) has also supported a *syn*-sedimentary origin for the disseminated Cu-sulfides, but with substantial resetting of this system during remobilization of the ore into veins (note, however, that there is debate on the meaning of Re—Os ages of these ore deposits: Sillitoe et al., 2017; Hitzman and Broughton, 2017; Muchez et al., 2017). This first stage is followed by re-mineralization during early and late diagenesis and subsequently by further hydrothermal redistribution of sulfides under high-temperature tectonic settings (e.g., Dewaele et al., 2006; El Desouky et al., 2009, 2010; Hitzman et al., 2010). Evidence for a multistage origin of the mineralization and accompanying changes in the fluids also comes from detailed petrographic work, fluid inclusion analyzes, as well as C, O, and Sr isotope compositions of different carbonate phases within these deposits (e.g., El Desouky et al., 2010; Muchez et al., 2010; Shanks III, 2014). Furthermore, the large range of sulfur isotope compositions, compatible with an early BSR process for the mineralization, could have been homogenized during the subsequent "redistribution" of the disseminated ore minerals. This possibly occurred under conditions amenable to thermochemical sulfate

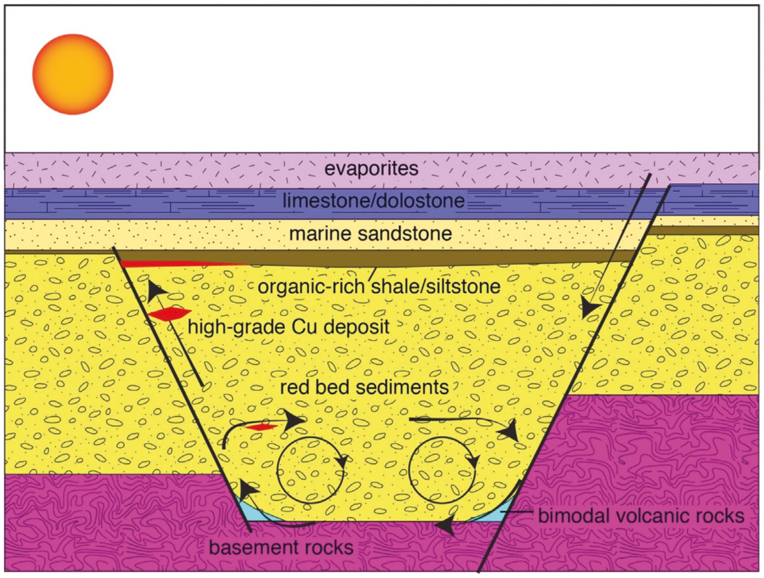

Fig. 15 Model of stratiform copper deposit formation. Black arrows represent fluid flow paths and convection cells. Modified from Hitzman MW, Selley D and Bull S (2010) Formation of sedimentary rock-hosted stratiform copper deposits through Earth history. *Economic Geology* **105**(3): 627–639.; Arndt NT, Fontboté L, Hedenquist JW, Kesler SE, Thompson JF and Wood DG (2017) Future global mineral resources. *Geochemical Perspectives* **6**(1): 1–171.

reduction (TSR) at higher temperatures (Leach et al., 2005; Muchez et al., 2010; Shanks III, 2014), during the transition from a disseminated or patchy mineralization to a more concentrated vein-hosted mineralization, but with a similar range in isotopic compositions. However, new metals may well have been introduced during the later, metamorphic stages of the metamorphism, notably in the metamorphosed deposits of the Central African Copperbelt, which may have also resulted in these deposits becoming supergiant ore deposits (e.g., Schmandt et al., 2013).

The circulation of highly saline fluid through broadly different lithologies, including occasional crystalline basement rocks (Fig. 15), may have also formed another category of sediment-hosted Zn—Pb—Cu deposits within the larger hydrothermal systems established during the deformation metamorphism of the Central African Copperbelt (e.g., Kampunzu et al., 2009). The fluid flow in such mineralizing systems is characterized both by unidirectional gravity-driven fluid flow of basinal brines from the near surface to deeper levels, as well as by the establishment of convective cells at deeper levels of the sedimentary basin before the fluid ascends to variably shallower levels where the high-grade Cu deposits are formed (Fig. 15). In such a context heterogeneous Pb isotope compositions, derived from mixing of two or more sources (Fig. 15), are likely and have also been corroborated on the basis of stable isotope compositions of heavy metals (Shanks III, 2014). However, heterogeneity of the compositions may be variable within individual deposits depending on differences in the plumbing systems, in the isotopic and Pb concentration contrasts of the involved lithologies, and in the efficiency of homogenization processes in the deep convective cells (see for instance variably homogeneous to heterogeneous Pb isotope compositions of sediment-hosted Zn—Pb—Cu deposits of Central Africa: Kampunzu et al., 2009).

Mississippi Valley-type (MVT) deposits

Mississippi Valley-type (MVT) Pb—Zn deposits are formed in back-arc foreland basins as the result of orogenic elevation and topography-driven fluid flow (Fig. 16). Basinal brines migrate into the deep portions of the foreland basin, coming into contact with different sedimentary and crystalline basement lithologies and thereby potentially leaching the Pb and Zn from these different lithologies. Eventually the fluid precipitates the metals in the shallow margins of the basin within platform carbonate lithologies, that act as efficient metal traps, through BSR reactions. Also mixing of oxidized metal-bearing brines with sulfide-rich fluids from thermochemical reduction of sulfate is a common metal precipitation mechanism in MVT deposits (Leach et al., 2010). Like sediment-hosted stratiform Cu deposits and other sedimentary exhalative (SedEx) types of mineralization, MVT deposits are also characterized by a wide range in S-isotope compositions of sphalerite and galena, typical for BSR of marine sulfate in open or partially closed platform-type marine carbonates (e.g., Goldhaber and Kaplan, 1974; Kuhlemann et al., 2001; Goldhaber, 2003; Leach et al., 2005; Shanks III, 2014). However, the modal distribution of the sulfides in terms of $\delta^{34}S$ values is different for different deposits on a regional and global scale, supporting locally variable conditions of permeability, initial sulfate concentrations and isotopic compositions as well as variable amounts of organic matter as the reducing substrate. Recent clumped isotope compositions on carbonate veins within MVT deposits of the Derbyshire Platform (UK) support models of pulsed fluid flow with mineralization temperatures ranging between 40 °C and 100 °C for the hydrothermal conditions of vein formation (Dennis et al., 2019). Regional differences in H, C, and O isotope compositions of gangue and vein minerals, but also in H and O-isotope compositions as well as Na—Cl—Br compositions of fluids included in sphalerite, galena and fluorite from different

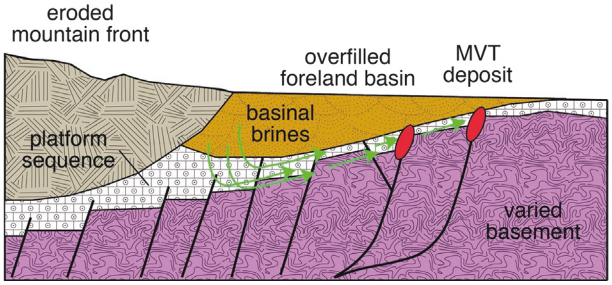

Fig. 16 Model of Mississippi Valley-type (MVT) deposit formation. Green arrows represent fluid flow paths. Modified from Leach DL, Bradley DC, Huston D, Pisarevsky SA, Taylor RD and Gardoll SJ (2010) Sediment-hosted lead-zinc deposits in Earth history. *Economic Geology* **105**(3): 593–625.; Arndt NT, Fontboté L, Hedenquist JW, Kesler SE, Thompson JF and Wood DG (2017) Future global mineral resources. *Geochemical Perspectives* **6**(1): 1–171.

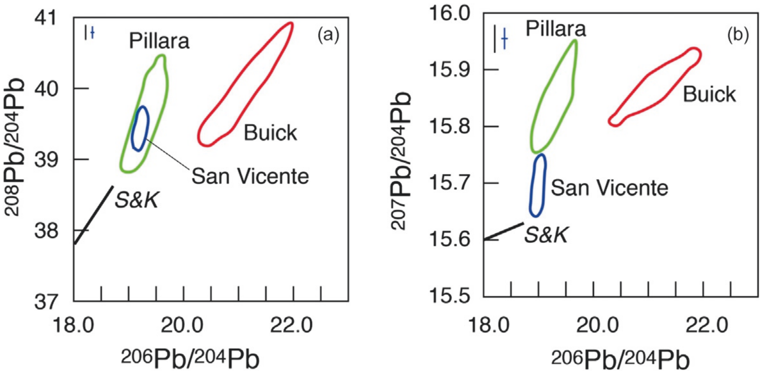

Fig. 17 Lead isotope compositions in the thorogenic (a) and uranogenic (b) plots of MVT deposits from Western Australia (Pillara), SE Missouri (Buick), and San Vicente (Peru). Error bars on the left corners of the two plots are 2SD uncertainties for Pillara and Buick (black) and San Vicente (blue). S&K is the Stacey and Kramer evolution curve of the Earth (redrawn from Gulson, 1986 with addition of data from San Vicente from Chiaradia and Fontboté, 2003).

mineral deposits, indicate the presence of variable mixtures of residual seawater and meteoric water. These mixed fluids have, however, extensively exchanged with regionally different sediments, evaporites, and crystalline basement rocks (Kesler et al., 1997; Shanks III, 2014).

MVT deposits are characterized by the widespread occurrence of radiogenic common lead isotopic composition of their ores, more radiogenic than the end-points of typical bulk Earth evolution curves (e.g., Gulson, 1986; Kesler et al., 1994; Tosdal et al., 1999) (Fig. 17). This requires leaching of lead from lithologies variably older than the mineralization and with μ (^{238}U/^{204}Pb) values much higher than those of the bulk Earth. Only in this way, such lithologies could have developed highly radiogenic compositions at the time of the mineralization. MVT ores often, but not always, define linear or cloudy elongated trends with different slopes, either steep or shallow in Pb isotope diagrams. This suggests derivation of Pb in these ores from mixing of crustal reservoirs characterized by variably high μ values and/or mixing of Pb from these highly radiogenic Pb reservoirs with Pb that is closer to a typical bulk Earth evolution.

The heterogeneous compositions of Pb isotopes in MVT deposits are consistent with the hydrothermal fluid plumbing system in this type of mineralization and the heterogeneous and variably old lithologies that the fluids encounter during their flow from the source region to the deposition site (Fig. 16). Large Pb isotope heterogeneities can be found even at the single galena crystal scale (Hart et al., 1981; Deloule et al., 1986), suggesting that the origin of Pb in the fluids changes not only depending on the position of the ore mineral in the deposit but also through the time required to precipitate single galena crystals.

Fig. 18 shows the examples of two trends from data in Potra et al. (2018) for the MVT deposits of two classical districts of central United States, the Northern Arkansas and Central Kentucky districts. The potential interpretation of these data provided below is purely based on the topology of the data in the ^{207}Pb/^{204}Pb versus ^{206}Pb/^{204}Pb space and could be applicable to other examples. For a full geological interpretation of the data the reader is invited to refer to Potra et al. (2018).

Fig. 18 shows that ore Pb from the Central Kentucky district forms a steep trend with a very small variation in ^{206}Pb/^{204}Pb values, whereas the ore Pb of the Northern Arkansas district forms a shallower trend with a large variation in ^{206}Pb/^{204}Pb values. In the diagram also shown are simulated mixing results between three hypothetical end-member sources (A, B, C) under the following conditions. Reproduction of the steep trend of the Central Kentucky district Pb is obtained assuming a 3-end member mixing in which source C contributes a maximum of 5% Pb. Reproduction of the shallow trend of the Northern Arkansas district is obtained assuming maximum 48% contributions of sources A and C and maximum 60% contribution of B. The source C in this hypothetic scenario represents radiogenic Pb associated with the evolution curve of a reservoir with a high $\mu = 40$, that separated at 1.2 Gyr

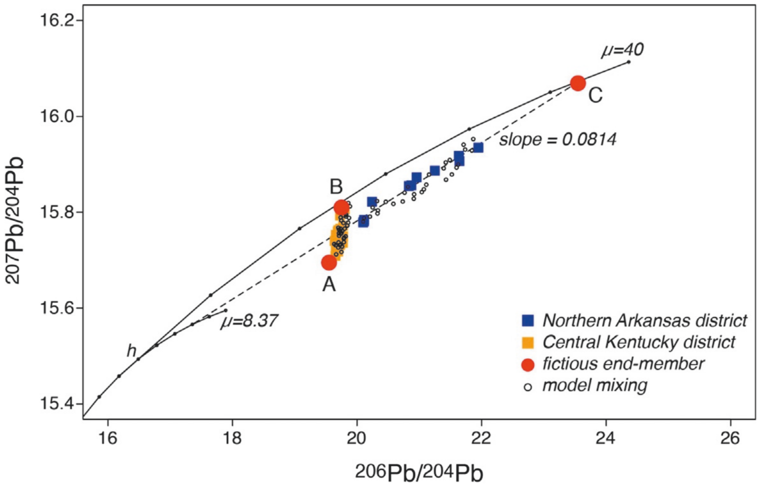

Fig. 18 Plot of Pb isotope compositions of MVT ores of the Northern Arkansas and Central Kentucky districts (data from Potra et al., 2018). The Central Kentucky district ores fall on a steep binary mixing trend between potential sources A and B. Northern Arkansas district ores are enclosed within a triangle formed by A, B, and C potential source lithologies (arbitrarily chosen in this example). Source C corresponds to radiogenic Pb from evolution in a U-rich reservoir with a μ value of 40. The empty black circles are simulations of mixing between the three end-members. For the Central Kentucky district ores, the simulations are obtained for a maximum contribution of Pb from source C of 5%. For the Northern Arkansas district ores, the simulations are obtained for maximum contributions of sources A and C of 48% and for B of 60%. The Northern Arkansas ores also scatter around a straight line with a slope of 0.0814 which would correspond to Pb leached from ~1.06 Gyr rock assuming a mineralization age of 250 Myr (see text for discussion). Small black circles on the evolution curves correspond to intervals of 400 Myr, starting from 0 Myr at the right hand-side of the curves.

from a "typical" bulk silicate reservoir characterized by a $\mu = 8.37$ (Fig. 18). This example shows that when only ore Pb isotope compositions are considered one can make some assumptions about the potential source rocks. However, it is the analysis of Pb isotope compositions of real potential rocks in the area that allows us to constrain the real sources (A, B, C) and their mixing proportions.

Another possible interpretation of the shallow trend defined by the Northern Arkansas ores is provided by the value of its slope (see also Potra et al., 2018; Kesler et al., 1994). In fact, shallow linear trends in the $^{207}Pb/^{204}Pb$ versus $^{206}Pb/^{204}Pb$ space may correspond to secondary isochrons (e.g., Faure and Mensing, 2005), that are defined by the following equation

$$m = \frac{^{207}Pb^{*}}{^{206}Pb} = \frac{1}{137.88}\left[\frac{e^{\lambda^{235}T} - e^{\lambda^{235}t}}{e^{\lambda^{238}T} - e^{\lambda^{238}t}}\right] \tag{16}$$

where m is the slope of the linear trend and corresponds to the radiogenic growth of $^{207}Pb^*$ and $^{206}Pb^*$, λ^{235} and λ^{238} are the decay constants of ^{235}U and ^{238}U, T is the time in the past when the radiogenic growth of $^{207}Pb^*$ and $^{206}Pb^*$ started from an isotopically homogeneous source with different μ values (point h in Fig. 18), and t is the time when the variably radiogenic Pb, which was formed between T and t along evolution curves with the same initial $^{206}Pb/^{204}Pb$ and $^{207}Pb/^{204}Pb$ values but different μ values, became fixed in the ore minerals. Therefore, T can be considered as the age of the source rocks and t the time of the mineralization.

The equation can be solved either for T or t by interpolation of the slope defined by the trend with the slopes obtained assigning fixed T and t values (e.g., see Faure and Mensing, 2005). If t (the age of the mineralization) is known, then T (the age of the source rock) can be obtained, vice versa if T is known then t can be calculated. In the case of the MVT deposits of mid-continent United States an age of about 250 Ma has been proposed based on U—Pb dating of hydrothermal calcite and paleomagnetic data (Pan et al., 1990; Potra et al., 2018). Using an age of 250 Ma for the mineralization, the slope of the Northern Arkansas district trend (0.0814 in Fig. 18) results in an age of the source rock of ~1.06 Gyr. Therefore, this treatment allows us to infer the potential contribution of radiogenic Pb from a source rock of a certain age that should be verified on the basis of the geological occurrence of rocks in this age range (see Kesler et al., 1994 and Potra et al., 2018, for discussion in this sense applied to MVT deposits of United States).

If $t = 0$ in the Eq. (16) above, then the equation reduces to

$$m = \frac{^{207}Pb^{*}}{^{206}Pb} = \frac{1}{137.88}\left[\frac{e^{\lambda^{235}T} - 1}{e^{\lambda^{238}T} - 1}\right] \tag{17}$$

which is the equation of an isochron allowing us to obtain the age of a series of cogenetic rocks, minerals (or their fractions: see below) having the same initial Pb isotope compositions but that evolved to different radiogenic signatures due to different μ values since the time of their formation (T) until nowadays.

In some studies, also Sr and Nd isotopes have been used to characterize the sources of the fluids in MVT deposits through the analysis of hydrothermal minerals like fluorite, barite and carbonates (Lange et al., 1983; Ruiz et al., 1985; Kesler et al., 1988; Bau et al., 2003). Sr and Nd isotope studies of hydrothermal non-ore minerals in MVT deposits may provide additional information on the fluid plumbing systems, but limited information on the metal sources, since there can be a large decoupling between Sr and Nd concentrations of potential source rocks on one hand and metal contents of the same rocks on the other hand (see next section for more details on this topic).

Pb isotopes as tracers of sources of other metals?

Pb isotopes are of course tracers of the sources of lead in various mineral deposit types. Because of the similar behavior in hydrothermal solutions, Pb isotopes are extensively used also as a proxy for the sources of other base metals like Cu and Zn and precious metals Au and Ag (e.g., Richards and Noble, 1998). Whereas this is justified to some extent, we warn from applying this without giving some thoughts to the problematic. The proportions of lead coming from two or more sources in ore samples are controlled by the isotopic compositions of the ore samples compared to those of the sources, but the proportions of the sources (i.e., fluids, rocks, magmas, reservoirs) involved in this process are also controlled by the concentrations of lead in those sources. For instance, a binary mixing between two sources A and B that corresponds to a 50:50 proportion of lead from them will correspond to sources that mix in 50:50 proportions only if the concentrations of Pb in the two sources are the same (Fig. 19). If the concentrations are significantly different the source with lower Pb concentrations needs to contribute in mass much more than the source with higher Pb concentrations to achieve a 50:50 proportion of the two lead types (Fig. 19).

The same reasoning applies to other metals, especially those, like Cu and Au, for which a decoupling in potential source rocks is expected with respect to Pb. For example, let us imagine a fluid that circulates through two isotopically different lithologies (A and B) from which it leaches Pb and Cu, with A being a mafic lithology with high contents of Cu (80–100 ppm) but relatively low contents of Pb (10–20 ppm) and B being a felsic lithology characterized by high contents of Pb (80–100 ppm) but low contents of Cu (1–5 ppm). This could be a scenario exemplifying the formation of stratiform copper, SHMS or VHMS deposits. It is clear that if the fluid leaches comparable volumes of the two lithologies (e.g., the green simulation points in Fig. 20) it will contain Pb that is dominantly derived from lithology B (~90%) and Cu that is dominantly derived from lithology A (>95%). If the two source rocks have different lead isotope compositions, the lead isotopes of the ore minerals will indicate a dominant source of Pb from lithology B (~90%) which can be erroneously interpreted also as the main source of Cu, which is clearly not the case (Fig. 20). The same applies to Au which has a geochemical behavior during petrogenetic processes more similar to Cu than to Pb, whereas Zn and Ag are more successfully proxied using Pb isotopes because they have a geochemical behavior more akin to Pb.

We conclude that, before extending the use of lead isotopes as tracers of the sources of other metals (especially Cu and Au), the geological situation should be carefully evaluated, recognizing the potential source lithologies and evaluating the concentrations of the various metals that these lithologies can deliver. In this sense, lead isotopes are more successfully used as tracers of fluid flow paths and of fluid-rock interactions than of sources of metals different from Pb (±Zn, Ag) itself.

Lead isotope model ages

Fig. 21 shows the isotope evolution curves of Pb through time starting from an initial composition (that of the Canyon Diablo troilite) at the time of Earth formation assuming three fixed and constant μ values of 8, 9, and 10 (single-stage or Holmes-Houtermans Pb evolutions). The lead isotope ratios of the points on such curves at any time t in the past (^{206}Pb/^{204}Pb$_t$ and ^{207}Pb/^{204}Pb$_t$) are the result of the addition of radiogenic lead, during the time interval between Earth's formation (T) and time t, to the initial primordial lead of the chondritic material (i.e., the lead of the Canyon Diablo troilite: ^{206}Pb/^{204}Pb$_T$ and ^{207}Pb/^{204}Pb$_T$)

$$\frac{^{206}Pb}{^{204}Pb_t} = \frac{^{206}Pb}{^{204}Pb_T} + \mu\left(e^{\lambda^{238}T} - e^{\lambda^{238}t}\right) \qquad (18)$$

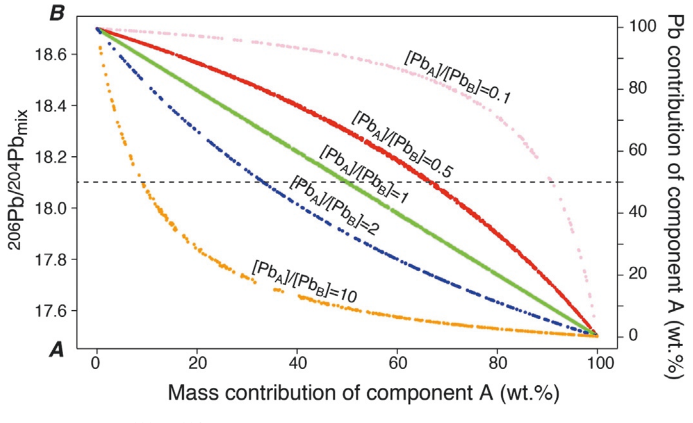

Fig. 19 Simulations of the relationship between the ^{206}Pb/^{204}Pb ratio resulting from mixing between two sources (A and B) and wt% mass contribution of source A for different ratios of the Pb concentrations in sources A and B [Pb$_A$/Pb$_B$].

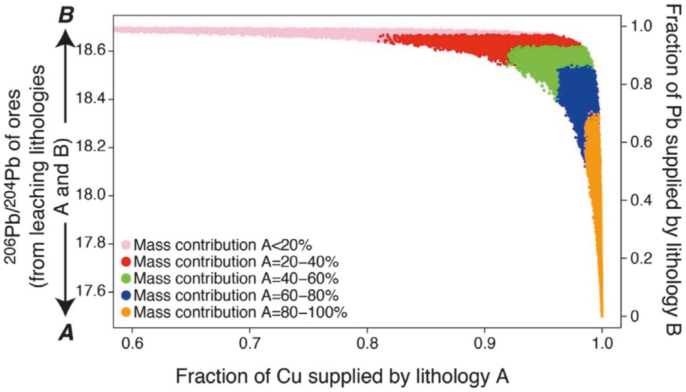

Fig. 20 Simulations of the relationship between $^{206}Pb/^{204}Pb$ compositions of ore minerals derived from leaching sources A (Pb = 10–20 ppm; Cu = 80–100 ppm; $^{206}Pb/^{204}Pb = 17.5$) and B (Pb = 80–100 pm; Cu = 1–5 ppm; $^{206}Pb/^{204}Pb = 18.7$) and fractions of Cu supplied by source A. The simulations are color-coded for mass contribution of source A.

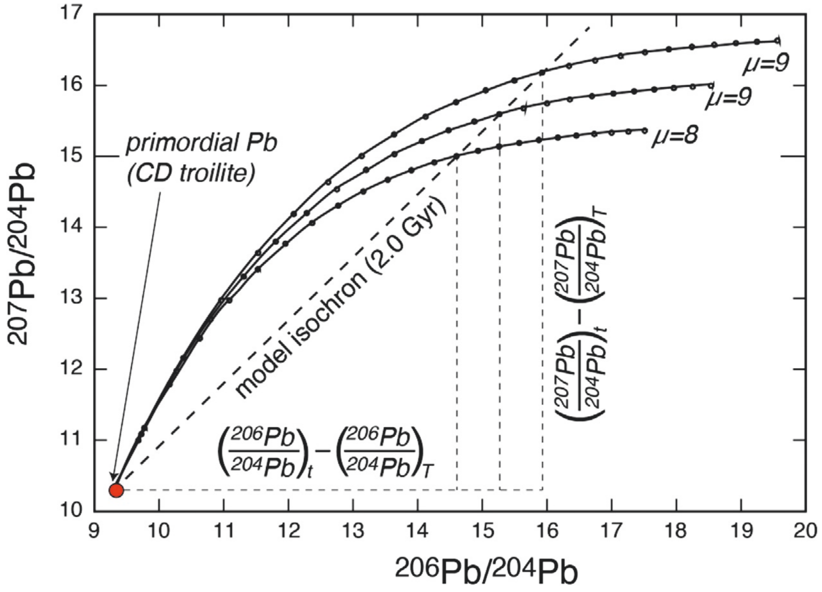

Fig. 21 Lead isotope model age of 2 Gyr for three different evolution curves (μ = 8, 9, 10).

$$\frac{^{207}Pb}{^{204}Pb_t} = \frac{^{207}Pb}{^{204}Pb_T} + \frac{\mu}{137.88}\left(e^{\lambda^{235}T} - e^{\lambda^{235}t}\right) \tag{19}$$

where λ^{238} and λ^{235} are the decay constants of ^{238}U and ^{235}U respectively and 137.88 is the $^{238}U/^{235}U$ ratio nowadays.

By rearranging and dividing the two equations one obtains

$$\frac{\frac{^{207}Pb}{^{204}Pb_t} - \frac{^{207}Pb}{^{204}Pb_T}}{\frac{^{206}Pb}{^{204}Pb_t} - \frac{^{206}Pb}{^{204}Pb_T}} = \frac{1}{137.88}\left(\frac{e^{\lambda^{235}T} - e^{\lambda^{235}t}}{e^{\lambda^{238}T} - e^{\lambda^{238}t}}\right) \tag{20}$$

It can be easily realized that this equation contains only one unknown (t) because $^{206}Pb/^{204}Pb_t$ and $^{207}Pb/^{204}Pb_t$ are measured on the sample, $^{206}Pb/^{204}Pb_T$ and $^{207}Pb/^{204}Pb_T$ are the values of the Canyon Diablo troilite (9.307 and 10.294 respectively), and T is the age of the Earth (e.g., 4.55 Gyr: Patterson, 1956). Therefore, using this equation a model age can be assigned to any sample that records the common lead signature of the Earth in the past (these samples are essentially galenas from stratabound deposits: see above). This equation cannot be solved by an algebraic method but only by interpolation (see Faure and Mensing, 2005 for details).

The age so obtained is not a radiometric absolute age, but a model age, i.e., it relies entirely on the assumption that the investigated sample has indeed evolved through a single-stage step characterized by a specific μ value. The latter, once obtained the age t, can be calculated from Eqs. (18) or (19) by substituting the age obtained from Eq. (20). Therefore, the above assumption must be tested against several criteria (first of all broad concordance with radiometric ages of the immediate geological environment) before the model age can be used for geological interpretations (see Faure and Mensing, 2005 for more details on Pb model ages).

Pb isotopes as metallogenetic terrane discriminators

Many studies have used lead isotopes of magmatic-hydrothermal ores and associated magmatic rocks to recognize the occurrence of different geological and metallogenic terranes at the regional scale and place the formation of distinct ore types in a broader paleo-geodynamic context. Terranes are crustal blocks with specific lithologic compositions and ages that become juxtaposed during the geodynamic history of Earth. Magmatism and associated mineral deposit formation subsequent or previous to the terrane juxtaposition result in lead isotope signatures that depend on the lithologies composing the terrane (i.e., continental vs. oceanic) and on their ages (i.e., young vs. old). Such an approach allows us to place mineral deposit formation in the context of a larger geographic scale and to correlate it with the geodynamic evolution of a specific region of the planet.

One of the seminal studies in this sense is the Pb isotope study on central Andean ores by Macfarlane et al. (1990), who individuated different Pb isotope provinces and compared them to the different geological domains of the region. Fig. 22 shows the metallogenetic Provinces and Subprovinces of Macfarlane et al. (1990) overlapped to a more recent contour map of Pb isotope composition of the Central Andes (Mamani et al., 2010) obtained by the combination of ore and magmatic rocks lead. Other studies that used Pb isotopes of ore minerals and magmatic rocks to delineate terrane boundaries have been carried out, among others, in the western United States (Wooden and Mueller, 1988; Wooden et al., 1988, 1998; Wooden et al., 1991), Ecuador (Chiaradia et al., 2004), Mexico (Potra and Macfarlane, 2014), and Central Asia (Chiaradia et al., 2006). In another study, Bouse (1995) showed that the different Ag/Au ratios of Arizona mineral deposits correspond to different Pb isotope systematics of the Proterozoic basement, suggesting a terrane control on the metallogeny of the region.

Another approach has been to combine large databases of Pb (and also Nd) isotopes with GIS to build up isotope maps, ranging in scale from mineral districts to continents. These isotope maps (see Fig. 22 for an example), which are based not only on isotope ratios but also on elaboration of lead model values (like μ and the difference between Pb model ages and known radiometric ages), can be used to delineate, especially within old continents, the occurrence of transcrustal tectonic limits and structures as well as magmatic belts that would correspond, based on isotope composition, to specific geodynamic settings with potential metallogenetic fertility (e.g., Champion and Huston, 2016; Huston et al., 2016; Wu et al., 2022).

Chiaradia and Fontboté (2002), using Pb isotope compositions of Cenozoic ore minerals and magmatic rocks from the entire Andean Cordillera, identified four regions characterized by steep mixing trends in the $^{207}Pb/^{204}Pb$ and $^{208}Pb/^{204}Pb$ versus $^{206}Pb/^{204}Pb$ space (Fig. 23) that they interpreted as the result of mixing between a MORB-type mantle and upper crustal rocks. They also noticed that the low radiogenic ends of the trends, corresponding to the MORB-type mantle, show a systematic decrease of $^{206}Pb/^{204}Pb$ values from north to south which they tentatively interpreted as the result of the influence of an increasing HIMU component in the northern section of the Andean Cordillera. This could be related to a Mesozoic plume that contaminated the mantle in the northern part of the Andes (Chiaradia and Fontboté, 2002) or to the interaction in the deep crust of mantle-derived magmas with oceanic plateau fragments that were accreted in the Late Cretaceous onto the margin of the northern Andes (Vallejo et al., 2009; Chiaradia, 2009; Chiaradia et al., 2020, 2021).

The success of Pb isotopes in tracking metallogenetic processes has also resulted in their use in mineral exploration programs. Gulson (1986) has outlined a series of case studies for the exploration of Australian deposits through the definition of region-specific Pb isotope targets (based on the occurrence of known mineralization) against which compare the metallogenetic potential of unknown prospects. Usable materials for the exploration of mineral deposits on which carrying out Pb isotope investigations are sulfides, gossans, soils, weathered bedrock, vegetation and groundwaters.

Osmium isotopes

Theoretical background

Os has seven stable isotopes, one of which, ^{187}Os, is the radiogenic product of the β^- decay of ^{187}Re. The $^{187}Re \rightarrow {}^{187}Os$ decay is used for dating various sulfide and also oxide ore minerals (see below). Molybdenite is the only widespread sulfide that does not contain any initial (common) osmium whereas it incorporates significant amounts of Re (up to >100 s of ppm). For this reason, it can be dated using Eq. (9), reasonably assuming that no initial Os is present (model age of molybdenite: Stein et al., 2000). Conversely, molybdenite cannot be used for common Os isotope tracing studies since there is virtually no common Os incorporated into molybdenite at the time of its formation and the only Os is radiogenic ^{187}Os developed in situ.

In contrast, other sulfides and oxides occurring in mineral deposits of various types always contain initial (common) Os in measurable amounts and in variable ratios with Re. Therefore, for these minerals the following equation applies

$$\frac{^{187}Os}{^{188}Os_t} = \frac{^{187}Os}{^{188}Os_0} - \frac{^{187}Re}{^{188}Os_0}\left(e^{\lambda^{187}t} - 1\right) \tag{21}$$

where λ^{187} is the decay constant of ^{187}Re, t is the time of the mineralization and the indices t and 0 refer to the isotope ratios calculated at the time t of the mineralization and measured today ($t = 0$), respectively. By analyzing only one of such non-molybdenite samples of a mineralization it is impossible to obtain both the age t of the mineralization and the initial Os isotopic composition

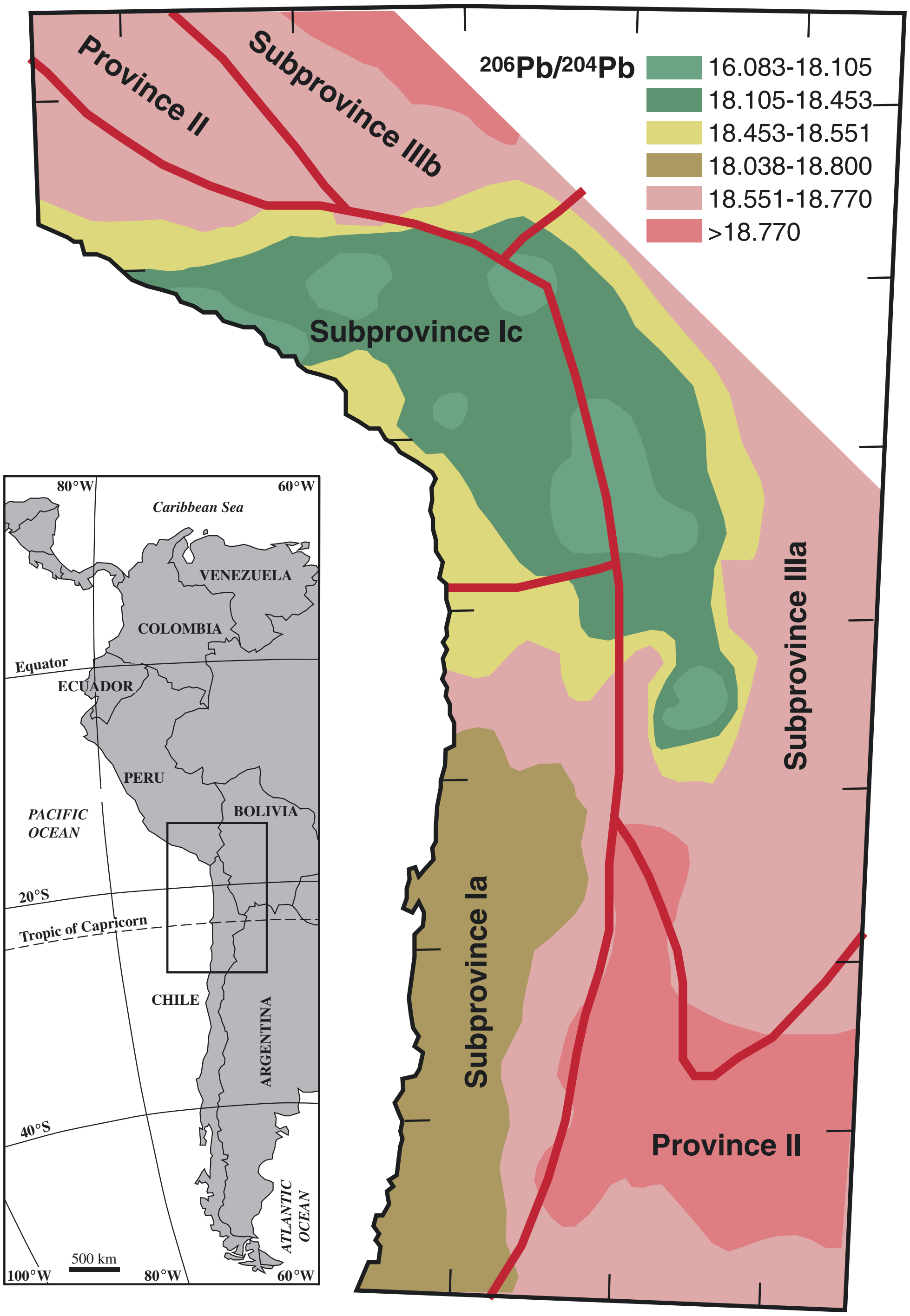

Fig. 22 Lead isotope provinces of MacFarlane et al. (1990) superimposed on the $^{206}Pb/^{204}Pb$ map of the Central Andes of Mamani et al. (2010), distinguishing different isotopic domains.

($^{187}Os/^{188}Os$), as discussed above. However, analyzing several cogenetic samples for the mineralization and using the isochron method (see below) both the age t and the initial common Os isotopic composition of the mineralization can be obtained.

The initial value of $^{187}Os/^{188}Os$ of a sample can also be expressed as its deviation from the value of the CHondritic Uniform Reservoir (CHUR) at the same age as that of the sample using the following notation

$$\gamma_{Os_t} = 100\left(\frac{^{187}Os/^{188}Os_{t-sample}}{^{187}Os/^{188}Os_{t-CHUR}} - 1\right) \tag{22}$$

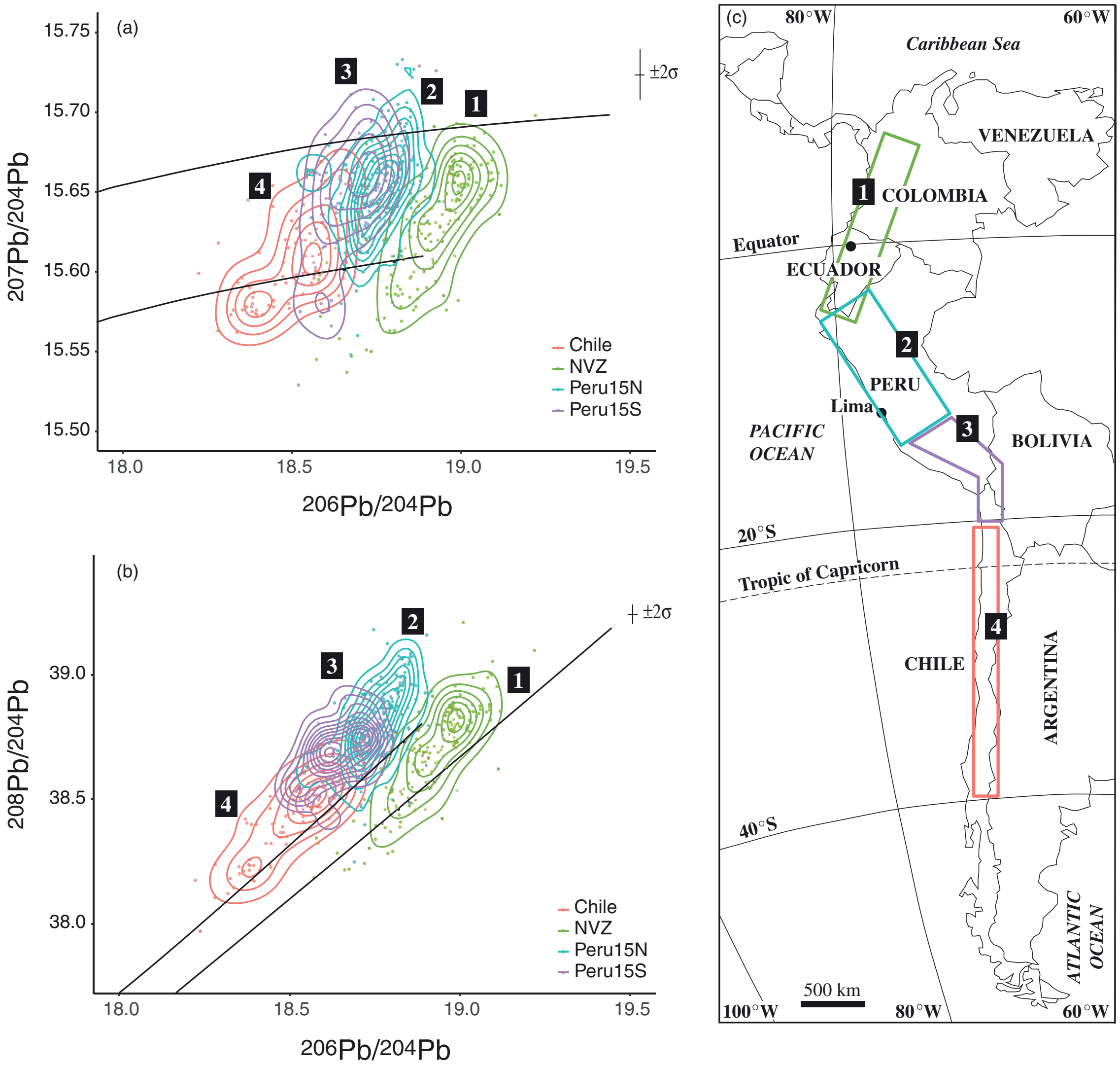

Fig. 23 Lead isotope compositions of 4 different provinces along the Andean Cordillera from Chiaradia and Fontboté (2002). Each province indicates mixing between a low $^{207}Pb/^{204}Pb$ and $^{208}Pb/^{204}Pb$ component and a high $^{207}Pb/^{204}Pb$ and $^{208}Pb/^{204}Pb$ component. At the same time each mixing line is shifted to progressively lower $^{206}Pb/^{204}Pb$ values from north to south. Concentric lines represent density contours for the data of each province.

where the indices "*t-sample*" and "*t-CHUR*" refer to the isotope ratios recalculated for both sample and CHUR at the time t using Eq. (21) above.

The systematics of radiogenic Os are controlled by the different compatibility of Os and Re during mantle magmatic processes. Os in fact is compatible during mantle partial melting due to its high affinity for residual sulfide phases, whereas Re is more incompatible (e.g., Lambert et al., 1999). This results in a Depleted Mantle reservoir that has evolved at low $^{187}Os/^{188}Os$ values through time because the mantle has continuously lost Re to partial melts that formed the crust (Fig. 24). These partial melts are characterized by very high Re/Os values which develop through time extremely high $^{187}Os/^{188}Os$ and positive γ_{Os} values (Fig. 24). Therefore, compared to the Rb—Sr, U—Pb, Sm—Nd and Lu—Hf systematics, in which both parent and radiogenic daughter isotopes are variably incompatible, the more distinct behavior of Re and Os makes this system more (very!) sensitive to crustal contamination.

Applications

Because Os is a platinum group element (PGE) the most widespread use of common Os isotopes is to trace the sources of PGE in various Ni—Cu—Co—PGE deposits (e.g., Kambalda, Voisey's Bay, Bushveld, Sudbury, Stillwater) (Lambert et al., 1999). There is a common agreement about the fact that PGE mineralization in this orthomagmatic context is associated with initially S-undersaturated mafic magmas derived from the mantle and intruded at upper crustal levels (Lambert et al., 1999). If such

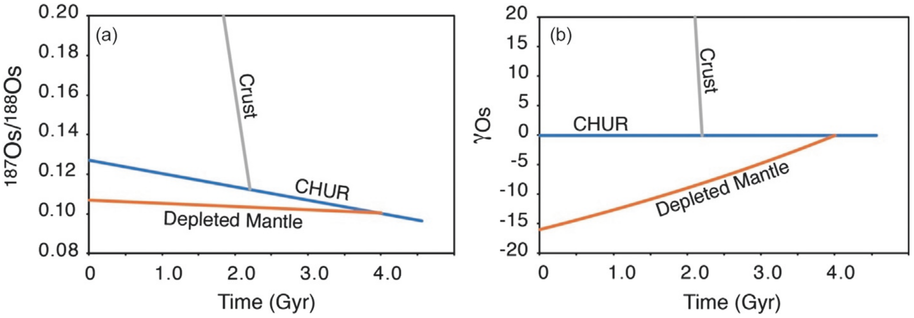

Fig. 24 Evolution through time of $^{187}Os/^{188}Os$ and γ_{Os} for CHUR (CHondritic Uniform Reservoir), Depleted Mantle and Continental Crust. The evolution of Depleted Mantle starts at 4.0 Gyr in this plot assuming that extraction of magma from the CHUR mantle to form continental crust started at this age and that the Depleted Mantle has a $^{187}Re/^{188}Os$ value of 0.0966. The Continental Crust evolution is for a hypothetical granitic crustal rock separated from CHUR at 2.2 Gyr and characterized by a $^{187}Re/^{188}Os$ value of 14.49.

magmas were S-saturated in the mantle or became so during their ascent before reaching the place where mineralization occurs, they would lose most if not all of PGEs, because of the extremely high compatibility of PGEs in sulfide phases. Therefore, mineralization occurs when these mantle-derived mafic magmas become S-saturated at shallow crustal levels. A process that may lead to sulfur saturation of these mafic magmas is assimilation of S-rich host crustal lithologies, a process that has been suggested based on the S-isotope compositions of such orthomagmatic complexes (e.g., Ripley and Li, 2003). Under this point of view, Os isotopes are ideally suited to reveal crustal contamination, due to the strong difference in $^{187}Os/^{188}Os$ signatures of mantle-derived magmas and variably old crustal rocks (Fig. 24). The plot of Fig. 25 shows $\gamma_{Os\text{-initial}}$ values of ore-related samples which indicate that crustal contamination of the magmas and associated ores occurred at the deposits of Sudbury, Stillwater and Bushveld, supporting the above discussed process of shallow crustal contamination as responsible for sulfur saturation of the magma. For the large and economically important Bushveld Igneous Complex, estimates of crustal assimilation during the emplacement of the complex of up to 30–40% are required in order to account for the overall high O isotope compositions of feldspar, pyroxene and biotite within the mafic-ultramafic layered suites, values that are unlike those for mantle-derived melts (e.g., Harris et al., 2005). Similar estimates have been made based on Sr and Nd isotopic compositions (e.g., Kruger and Marsh, 1982; Kruger, 1994; Maier et al., 2000). In contrast to the Sr and Nd isotopic compositions, however, the homogeneous O-isotope compositions throughout this large complex and the constancy of the inter-mineral O-isotope fractionations would support large scale assimilation of ^{18}O-rich lower to middle crustal rocks during the emplacement of the magmas of the complex (Harris et al., 2005).

Another advantage that makes Os isotopes particularly suited to trace crustal contamination in PGE orthomagmatic deposits is the occurrence in these deposits of high-Os and low-Re minerals, like Os-rich laurite (RuS_2) and chromite. Chromite has been often analyzed on bulk mineral separates, but this mineral may host micro-inclusions of Os-rich minerals like laurite and osmium-iridium alloys, which have also been analyzed individually for Os isotope composition using in situ methods (e.g., Ahmed et al.,

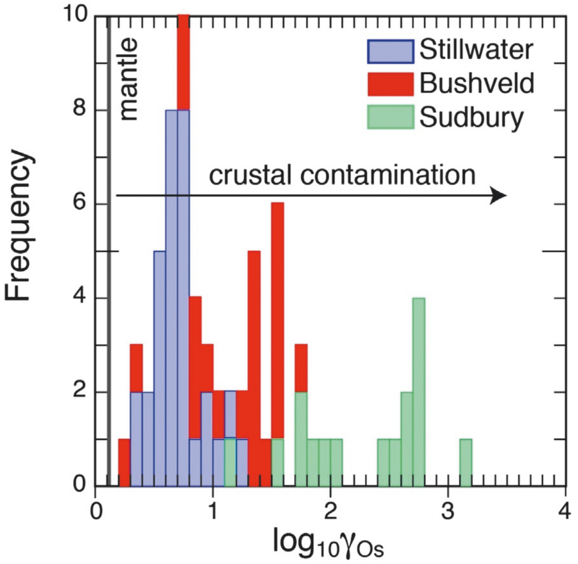

Fig. 25 Common Os isotope compositions of rocks and ores of three major orthomagmatic PGE deposits showing various degrees of Os crustal contamination of the mantle-derived Os.

2006). This particularity makes ore minerals commonly associated with orthomagmatic PGEs deposits (e.g., chromites, Os-rich sulfides like laurite) the most suitable to be used in tracing studies, because their very low to near zero Re/Os values minimize the time-integrated correction for in situ decay and associated uncertainties due to age and Re—Os concentration measurements as well as possible open system behavior (see also above). In Os-poor sulfides such time-integrated corrections require, besides knowledge of the age, also precise measurements of Re and Os concentrations, that should be obtained by isotope dilution, making the overall analytical procedure longer and requiring specialized laboratories.

Although the majority of Os tracing studies has concentrated on PGE orthomagmatic deposits, Os isotopes have also been used in conjunction with isochron dating to determine initial isotope ratios of various Os-poor sulfide minerals in other deposit types (e.g., porphyry Cu deposits, sediment-hosted Cu—Co deposits) with consequent inferences about mantle versus crustal Os sources in these deposits (e.g., Ruiz and Mathur, 1999). For instance, Mathur et al. (2000), using initial $^{187}Os/^{188}Os$ obtained from regressions of sulfides isochrons from various Chilean porphyry Cu deposits, could find that the stronger is the mantle contribution defined by the $^{187}Os/^{188}Os_i$ values, the larger is the Cu endowment of the deposit. Saintilan et al. (2021), using initial $^{187}Os/^{188}Os$ of sulfides (pyrite and enargite) from the high-sulfidation epithermal deposit of Colquijirca and the Cordilleran-type base metal deposit of Cerro de Pasco (Peru), found that there was a decrease in the crustal Os contribution through time (i.e., using minerals of the paragenetic sequence), which they explained by initial flushing of crustal osmium by early magmatic fluids, so that late-stage enargite was unaffected by crustal Os (see also Fig. 10 for a visualization of this interpretation).

Dating mineral deposits

Geochronology of mineral deposits is essential to correlate mineralization to large-scale geological processes, e.g., magmatism, metamorphism, climatic changes, biologic activity, tectonism, and/or geodynamics (e.g., Hames et al., 2009; Bekker et al., 2010). It also allows us to link various mineral deposit types with major events of the Earth's history (e.g., supercontinent assembly, oxidation events, climatic changes) and to evaluate their temporal recurrence or uniqueness (Watson, 1978; Veizer et al., 1989; Barley and Groves, 1992; Goldfarb et al., 2001; Frimmel, 2005; Heinrich, 2015). Geochronology of mineral deposits also offers a "predictive" tool for exploration of different mineral deposit types within specific geochronological windows. Finally, the determination of the timescales of mineralizing events improves our understanding of the physico-chemical processes that lead to metal precipitation, especially the rate at which metallogenic processes occurs, which is a function of the energy of the system and how this energy is distributed through time (Weis et al., 2012; Chiaradia et al., 2013, 2014; Chelle-Michou et al., 2017; Chiaradia et al., 2018; Chiaradia, 2020, 2022; Large et al., 2021; Chiaradia and Caricchi, 2022; Carter et al., 2022).

Radiometric dating is the most accurate and precise way of determining the age of a mineral deposit. Careful textural observations should be carried out prior to dating in order to date ore and/or alteration minerals that are genetically associated with the mineralization (e.g., Chiaradia et al., 2013). Accuracy refers to how close a measurement of an age is to the "real" value (see Chiaradia et al., 2013 about how accuracy is estimated). Precision indicates the uncertainty associated with an age and usually depends on limitations of the analytical and instrumental tools used. Date is the geochronological value returned by radiometric dating which becomes an age only after its interpretation and validation within the geological context.

Theoretical background

The theoretical bases of radioactive-radiogenic systems which are used for dating have been addressed above (Section "Bases of radioactive-radiogenic isotope systems") and are extensively discussed in, e.g., Dickin (2005) and Faure and Mensing (2005). Here, we just summarize some essential information. Dating of minerals can be done using Eq. (1), if the dated mineral does not incorporate any initial amount of radiogenic isotope (e.g., zircon and molybdenite), or Eq. (5), if the dated mineral incorporates non-negligible amounts of initial radiogenic isotope.Each one of these equations can be solved for t, yielding

$$t = \frac{1}{\lambda} \ln\left(\frac{D}{N_0} + 1\right) \tag{23}$$

$$t = \frac{1}{\lambda} \ln\left(\frac{D/R_{ref} - D_t/R_{ref}}{N_0/D_{ref}} + 1\right) \tag{24}$$

However, there are several conditions that must be met in order to use Eqs. (23) and (24) to obtain meaningful ages. The most important is that the dated mineral must have behaved as a closed system since its formation, not allowing any escape or ingression of either parent or daughter isotopes, which would modify D/N_0 and D_t/D_{ref}, resulting in unconstrained D/D_{ref} ratios and D and N_0 amounts. This condition is difficult to be met because: (i) all elements occurring in minerals, including radioactive isotopes, tend to diffuse in order to re-equilibrate with the surrounding environment under the drive of chemical and thermal gradients; (ii) radioactive decay creates damage to the crystalline lattice of minerals, which favors the escape or ingression of elements; (iii) the minerals hosting the radioactive parents may be subjected to interactions with fluids during their geological life which will cause a release or an ingression of radiogenic and parent isotopes (the reader may refer to Mattinson, 2005, to see how the problem of crystal lattice damage of zircons can be tackled in U—Pb geochronology). Among these three processes, thermally activated diffusion is a ubiquitous process, by which elements diffuse within crystals as a function of atomic size, crystal structure, crystal size, and temperature. For a particular element in a particular crystal structure, diffusion becomes increasingly fast with increasing temperature, through an exponential function known as the Arrhenius law (Fig. 26).

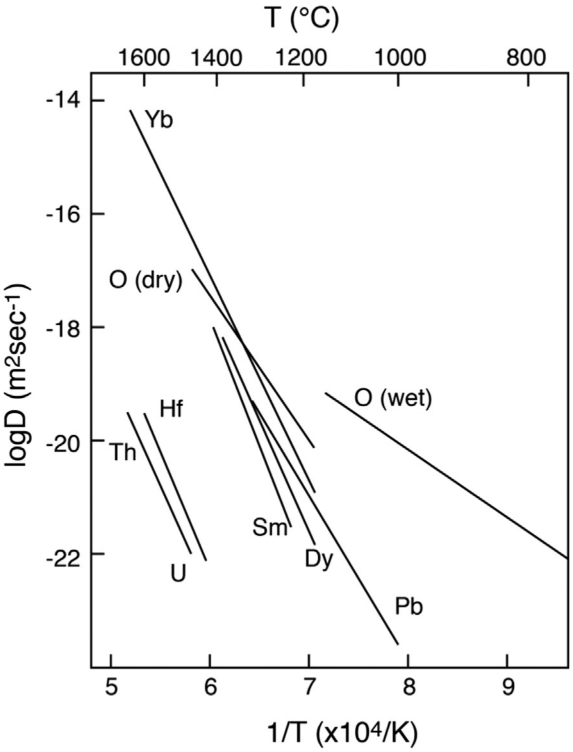

Fig. 26 Data on diffusion of various elements in zircon. From Cherniak DJ and Watson EB (2001) Pb diffusion in zircon. *Chemical Geology* **172**: 5–24 and references therein.

Therefore, a radiometric date reflects the time since the mineral cooled to a temperature below which diffusion of the parent and daughter isotopes becomes so slow that the mineral acts as a closed system. This temperature is known as closure temperature (Dodson, 1973). Because the closure temperature depends on crystal structure, size of the crystal, and atomic size of the diffusing isotope, there is a wide range of closure temperatures (from >900 °C to <100 °C) for the different radiometric dating systems applied to different minerals (Fig. 27).

In cases where a mineral has grown at temperatures below its closure temperature for the isotopic system of interest, a radiometric date reflects the time of formation of that mineral. In contrast, where a mineral grows at temperatures above its closure

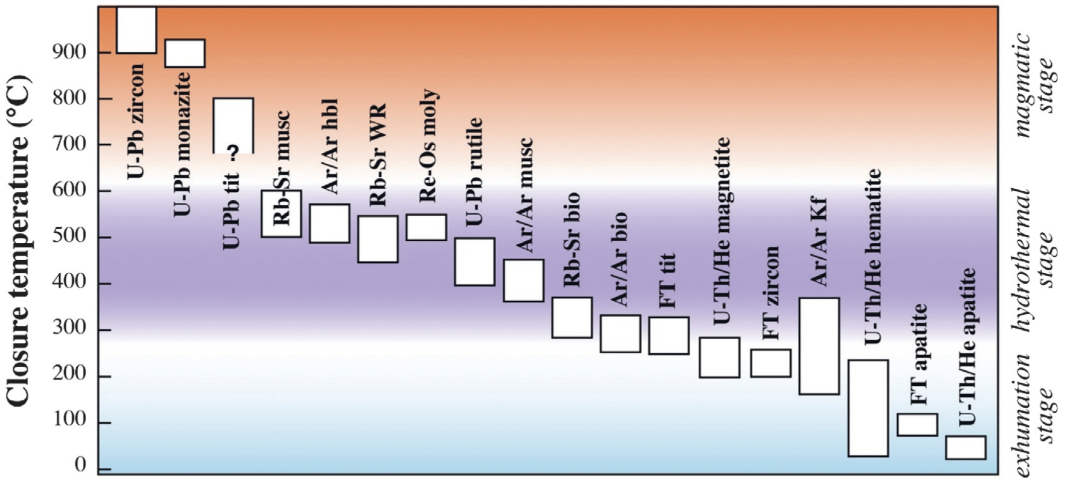

Fig. 27 Closure temperatures of various dating methods for different minerals. Modified from Chiaradia M, Schaltegger U and Spikings R (2014) *Time Scales of Mineral Systems—Advances in Understanding Over the Past Decade.* SEG Special Publication 18, pp. 37–58 and references therein, plus Kohn MJ (2017) Titanite petrochronology. *Reviews in Mineralogy and Geochemistry* **83**(1): 419–441.; Harrison TM, Célérier J, Aikman AB, Hermann J and Heizler MT (2009) Diffusion of ^{40}Ar in muscovite. *Geochimica et Cosmochimica Acta* **73**(4): 1039–1051.; Eberlei T, Habler G, Wegner W, Schuster R, Körner W, Thöni M and Abart R (2015) Rb/Sr isotopic and compositional retentivity of muscovite during deformation. *Lithos* **227**: 161–178.

temperature, the radiometric date will be younger than the time of mineral formation. The time when a mineral cools below its closure temperature can be variably younger than the time of its formation depending on the thermal history (e.g., cooling rate) of the rock that contains the mineral (thermochronology). These considerations highlight the need to know as much as possible the geological context of the sample. Additionally, a mineral can be dated using Eqs. (23) and (24) only if it does not incorporate any significant amount of daughter isotope from the surrounding environment during its formation (Eq. (23)) or if the amount and isotopic composition of the incorporated daughter isotope are known (D_t/D_{ref} in Eq. (24)). In such cases either all the daughter isotopes measured in the mineral can be attributed to in situ radioactive decay (Eq. 23) or a correction for the incorporation of the initial daughter isotopes can be applied (Eq. 24).

Dating minerals that do not contain any initial amount of radiogenic daughter isotope

Daughter isotopes of any parent-daughter system are continuously produced everywhere on Earth and therefore the possibility to use Eq. (23) depends on the ability of a mineral to selectively incorporate a radioactive parent and exclude the radiogenic daughter at the time of mineral formation. The most commonly dated minerals that behave in this way and allow the use of Eq. (23) are zircon and monazite for the U(—Th)—Pb system and molybdenite for the Re—Os system, for which the Eqs. (8) and (9) apply. Additionally, for the U—Pb system in zircon another independent age equation applies for the decay of ^{235}U to ^{207}Pb

$$t = \frac{1}{\lambda^{235}} \ln\left(\frac{^{207}Pb_0}{^{235}U_0} + 1\right) \tag{25}$$

This provides the unique possibility to date the same mineral with two independent U—Pb chronometers (Eqs. (8) and (25)) and allows us to check for open (different, i.e., discordant ^{238}U—^{206}Pb vs. ^{235}U/^{207}Pb ages) versus closed system (same, i.e., concordant ages) behavior of the U—Pb clocks in zircon, through their graphic expression in Concordia plots as concordant or discordant points (Fig. 28). Fig. 28 shows a concordant point analysis corresponding to t_1 and several analyzes of cogenetic zircons from the same intrusion showing all the same concordant ages for which a pooled concordant age can be calculated (inset of Fig. 28). Fig. 28 also shows that either Pb or U loss can be identified in the Concordia plot. If lead loss at time t_3 affected a number of zircons that crystallized from a magma at time t_2, the zircons will plot on a chord (called Discordia) intercepting the Concordia at two points: the upper one represents the age of zircon crystallization from the magma (t_2) whereas the lower one represents the timing

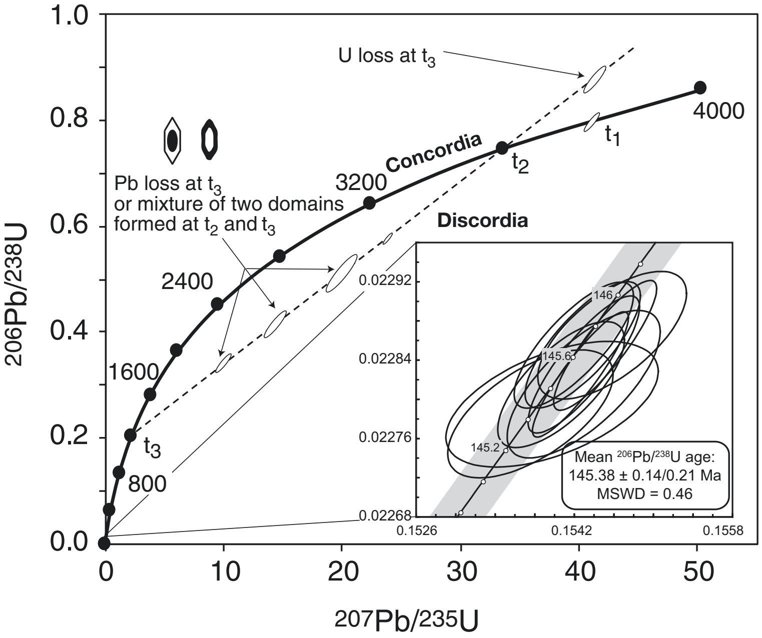

Fig. 28 Wetherill U—Pb Concordia diagram. In this diagram zircons yielding the same ages with the decays of ^{238}U to ^{206}Pb and of ^{235}U to ^{207}Pb fall on the Concordia line. Note that each zircon analysis is represented by an ellipse that corresponds to analytical uncertainties of the ^{207}Pb/^{235}U and ^{206}Pb/^{238}U values. Zircons that underwent lead or uranium loss define straight lines (called Discordia) that intersect the Concordia curve at points that may be interpreted geologically. Various examples are shown. Zircon t1 is a zircon yielding a concordant age of 3800 Myr. The zircons along the Discordia line t_2-t_3 represent zircons that initially crystallized at time t_2 but underwent Pb or U loss at time t_3. Their alignment intersects the Concordia at times t_2 and t_3 that can be interpreted as the time of magmatic crystallization ($t_2 = 3600$ Myr) and the time ($t_3 = 1200$ Myr) of a geological event that has caused partial Pb (or U) loss (e.g., metamorphism). Note that the zircon analyzes plotting along the Discordia line t_2-t_3 and corresponding to Pb loss could also represent another situation: they could be the result of the analysis of bulk single zircon grains characterized by an old core crystallized at t_2 and a younger rim overgrown at t_3. This is why each analysis of a zircon must be preceded by a careful petrographic evaluation through CL-imaging to identify old cores. In such a case a bulk grain analysis would be meaningless and an in situ analytical approach, allowing the dating of small domains of the zircon, should be undertaken.

of the event (e.g., metamorphism) that caused the lead loss (t_3). Lead loss can also occur continuously since the time of crystallization of the zircons from the magma due to damage of the crystal lattice: in such a case a continuous escape of Pb occurs through time resulting in a Discordia line that intersects the Concordia at zero age. Because the diffusion of Pb is more likely to result in Pb loss for the Pb atoms that are situated closest to the outer surfaces of a zircon grain, different procedures have been adopted to limit the effects of Pb loss. For many years, one procedure has been that of the mechanical abrasion of the outer rims of zircons (Krogh, 1982). However, application of such method does not warrant always a complete removal of the zircon domains affected by Pb loss. The procedure of chemical abrasion (CA) of zircon (Mattinson, 2005) has dramatically reduced the effect of lead loss and has become the analytical approach of choice to date zircon by CA-ID-TIMS and also LA-ICPMS (e.g., Crowley et al., 2014) in many labs.

The inset shows single grain analyzes of zircons from the same sample of a porphyritic rock associated with the gold skarn mineralization of Nambija (Ecuador) (data from Chiaradia et al., 2009). All the ellipses referring to each zircon analysis and its uncertainties overlap and fall on the Concordia, yielding a combined Concordia age of $145.33 \pm 0.14/0.21$ Ma age. The two uncertainties associated with the age are the analytical uncertainty (0.14) and the analytical uncertainty plus the uncertainties on the ^{238}U and ^{235}U decay constants. The latter are graphically represented by the gray band in the inset plot.

Discordant lines defined by several cogenetic zircons could also be the result of mixing of domains grown at different times, e.g., an older core and a younger rim, which cannot be deconvoluted by the analysis of a bulk zircon grain. For instance, an older core could represent a detrital zircon from erosion of an old magmatic rock and transferred into a sedimentary rock that subsequently has undergone partial melting with growth of a magmatic zircon rim around the old core (Fig. 28). Conversely, zircons from a magmatic rock subjected to metamorphism can also be overgrown by a metamorphic rim (Fig. 28; e.g., Gaynor et al., 2022). In any case, these examples, corresponding to zircon grain analyzed in bulk or to spot analysis straddling two domains, highlight the need of careful textural characterization of the zircon crystals to be dated, e.g., through cathode-luminescence imaging.

For the Re—Os chronometer the control of double concordant ages is not possible. However, dating of several molybdenites that can be considered cogenetic based on paragenetic observations, will yield different concentrations of ^{187}Os and ^{187}Re that can be plotted in the ^{187}Os versus ^{187}Re space (Stein et al., 2001). These molybdenites should plot on a straight line (isochron) passing through the origin of this diagram, lending support that they record the same time of crystallization. The high closure temperatures of zircon (Cherniak and Watson, 2001) and molybdenite (Stein et al., 2001) for the U—Pb and Re—Os systems, respectively, usually higher than crystallization temperatures of these minerals, imply that dates obtained on these minerals are most of the times crystallization ages.

Dating minerals that contain an initial amount of radiogenic daughter isotope

Eq. (24) applies to all minerals that incorporate non-negligible amounts of radiogenic isotope at the moment of their formation so that the final amount of radiogenic isotope is the sum of that isotope incorporated at the moment of mineral formation plus the amount developed in situ by decay of the incorporated radioactive parent. Eq. (24) can be solved for time only if we know D_t/R_{ref}, i.e., the ratio of the radiogenic to the reference non-radiogenic isotope incorporated at the moment of crystal formation.

One possibility to solve Eq. (24) is to assign a sound value to D_t/R_{ref}. This is done when dating minerals with the K—Ar method and its derivation, the Ar/Ar method, in which it is usually true (and verifiable using the isochron method: see below) that initially incorporated Ar has the fixed and known isotopic composition of atmospheric argon. This is also the case of minerals datable with the U—Pb method, like titanite and rutile for instance, for which a reasonable value of D_t/R_{ref} can be assumed using, for instance, common Pb isotope compositions of Earth evolution models or of associated minerals (e.g., K-feldspar). It is important to bear in mind that not all titanite and rutile minerals yield equally successful ages with this method, because the successful dating requires that the in situ grown radiogenic proportion of Pb in Eq. (24) be much greater than the proportion of common Pb incorporated in the mineral at the time of its formation. This is so because, when there is little radiogenic Pb added within the mineral, the radiogenic and common Pb components become increasingly close in composition and error propagation magnifies through a power law the uncertainty on the calculated age (Fig. 29). In addition, if the assumed common Pb composition is not correct the age calculated will also be increasingly inaccurate.

Another way to date minerals that contain mixtures of radiogenic and common leads is to use the Tera-Wasserburg plot (Fig. 30). In such a plot different cogenetic crystals or their portions (for bulk dissolution methods) or spots from different in situ analyzes may define straight mixing lines between common and radiogenic Pb end-members. The lower intersection of these lines with the Concordia curve provides the age. This diagram is often used, especially for in situ methods results (SIMS, LA-ICPMS), to date minerals containing significant amounts of common lead, like titanite, rutile, cassiterite, calcite. Because of the shape of the Concordia, this method can be applied only to relatively young minerals, e.g., $<\sim$400 Ma old.

The K—Ar and Ar/Ar methods

The K—Ar method of dating of K-bearing minerals differs for at least two issues compared to U—Pb and Re—Os dating of zircon and molybdenite, respectively. The first issue is that the relatively low closure temperatures of Ar diffusion in commonly dated K-bearing minerals (Fig. 27), due to the high diffusivity of Ar, implies that K—Ar dates record the time at which the minerals cool below their Ar closure temperatures. The latter, for most K-bearing minerals, fall in the lower range of hydrothermal temperatures (Fig. 27) and therefore may be lower than the mineral crystallization temperatures. In such a case, the K—Ar date recorded by the mineral will be younger than the mineral crystallization age. In other cases, the crystallization of the K-bearing minerals may occur at temperatures that are similar or lower than their closure temperature. In such a case the K/Ar date will yield the crystallization age

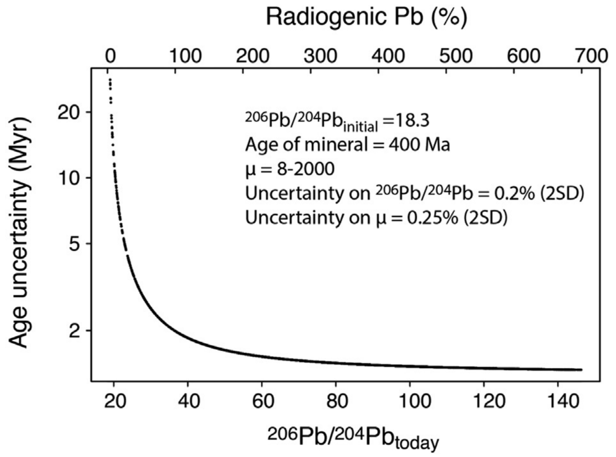

Fig. 29 Dependence of the age uncertainty (2SD) calculated using Eq. (24) for different amounts of radiogenic Pb developed within the mineral depending on μ (^{238}U/^{204}Pb) values varying between 8 and 2000 for an age of 400 Ma. As the amount of radiogenic Pb decreases below 100% (with respect to common Pb with a ^{206}Pb/^{204}Pb $= 18.3$) the increase in age uncertainty follows a power law.

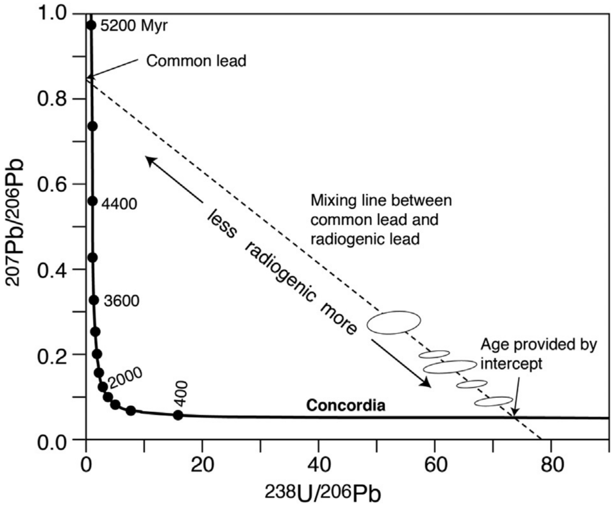

Fig. 30 The Tera-Wasserburg plot is often used for dating relatively young (e.g., <400 Ma old) minerals. Indeed, the plot shows that for ages >400 Myr the resolution becomes worse. This is particularly true if the analyzes are not concordant and the age must be obtained by regression of various points and their intersection on the Concordia line. In this a case the definition of such intersection becomes impossible for ages $>\sim 400$ Myr. This type of diagram is particularly used for minerals that contain variable amounts of common Pb (e.g., titanite, rutile, cassiterite, carbonates, and others). If various cogenetic minerals or domains of the same mineral characterized by different U/Pb ratios are analyzed they may define a straight line which is a mixing line between the more radiogenic samples/domains and the less radiogenic ones. The intersection on the lower side of the Concordia will yield the age whereas the intersection on the y-axis will yield the common Pb isotope composition. Black dots on the Concordia correspond to 400 Myr intervals.

of the mineral. Careful petrographic studies should be carried out to evaluate the meaning of K—Ar ages of K-bearing minerals associated with mineral deposits. This is especially true in multi-pulsed systems like porphyry deposits that are characterized by long-lived thermal anomalies above the closure temperature of commonly dated K-bearing minerals (e.g., Chiaradia et al., 2014). The second issue is that the K—Ar method requires independent measurements of K and Ar by distinct analytical methods on different sample aliquots, which poses a problem of sample size and aliquot homogeneity. For other issues related with the K/Ar and Ar/Ar dating systems applied to mineral deposits the reader may refer to Richards and Noble (1998) and Chiaradia et al. (2013, 2014).

The ^{40}Ar/^{39}Ar method of dating is a derivation of the K—Ar method, and has the advantage that a date can be obtained through a single measurement of the same sample aliquot on a noble gas mass spectrometer. This is achieved thanks to the conversion of ^{39}K of the sample to ^{39}Ar by neutron irradiation in a nuclear reactor. Since ^{39}K and ^{40}K occur in a fixed ratio, ^{39}Ar becomes a proxy for the measurement of ^{40}K. This method requires the use of monitors with a known age for the quantification of the conversion of ^{39}K to ^{39}Ar in the reactor, and is therefore an indirect dating method relying on the accuracy of the monitors' ages (see Richards and

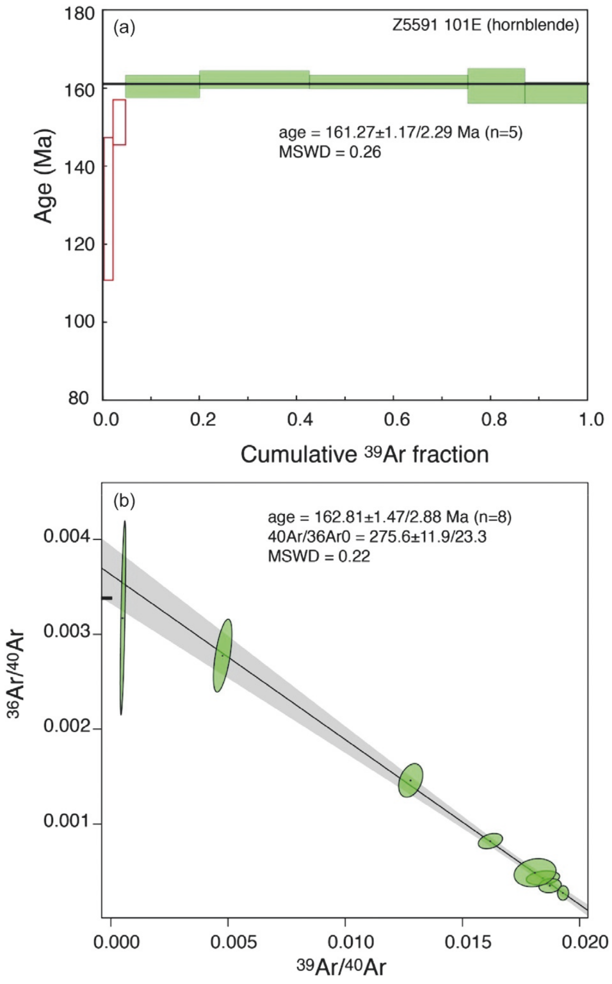

Fig. 31 Ar/Ar data of a hornblende from a porphyritic rock associated with a porphyry Cu—Mo mineralization (San Carlos prospect, Pangui district Ecuador: data from Chiaradia et al., 2009). In (a) it is reported the ^{40}Ar/^{39}Ar age spectrum corresponding to the release of subsequent argon fractions from the hornblende upon heating. The last five fractions (in green), corresponding to the higher temperatures, define ages that overlap within uncertainties yielding a plateau. The inverse isochron plot (b) shows that the regression of the different heating steps yields an isochron age that overlaps within uncertainty with the plateau age and intersects the ^{36}Ar/^{40}Ar axis at a value that is, within uncertainty, that of atmospheric Ar. This excludes the initial incorporation of significant amounts of non-atmospheric Ar in the hornblende. The ages are reported with uncertainties stated as 'x I y' where x stands for the standard error and y for the studentized 95% confidence interval (Vermeesch, 2018).

Noble, 1998, Dickin, 2005 and Faure and Mensing, 2005, for more details). The reader may refer to Chiaradia et al. (2013) for potential problems related to inaccurate ages of the monitors when dating mineral deposit formation.

Another advantage of the ^{40}Ar/^{39}Ar over the K—Ar method is that it allows the acquisition of a series of dates on the same sample by incrementally heating it, which causes the release of Ar aliquots at each different heating step (Fig. 31a). The dates so obtained correspond to the release of Ar from increasingly retentive (i.e., higher closure temperatures) parts or crystallographic domains of the mineral. This method allows us to draw an age spectrum diagram using the dates obtained for each step of argon released during the mineral heating process (Fig. 31a). In ideal cases, several steps (usually the higher temperature ones accounting for at least 50% of the total ^{39}Ar released) provide statistically identical ages forming a so-called plateau age (Fig. 31a) (see Dalrymple and Lanphere, 1974; Lee et al., 1991 for the requirements necessary to obtain a plateau age). This plateau age can be considered as the closest approximation to the age of the mineral. Younger ages, usually pertaining to the lower temperature steps, correspond to parts and/or crystallographic domains of the mineral that have undergone variable Ar loss. The isochron diagram (Fig. 31b) allows us to evaluate whether the assumption that the isotope composition of the initial argon incorporated into the dated mineral at the time of its formation, is indeed that of atmospheric argon that is used in Eq. (24) to calculate the age. The reader is invited to consult the specific literature (e.g., Richards and Noble, 1998; Faure and Mensing, 2005; Dickin, 2005) for more detailed information on the K—Ar and ^{40}Ar/^{39}Ar dating methods.

Isochrons

Another possibility to solve Eq. (24), for minerals with unconstrained value of D_t/D_{ref} is given by the observation that Eq. (24) represents a straight line with a slope m

$$m = \frac{D/R_{ref} - D_t/R_{ref}}{N_0/D_{ref}} \tag{26}$$

in the isotope space (D/R_{ref}–D_t/R_{ref}) versus N_0/D_{ref}. Such a straight line is called an isochron, i.e., an alignment of points yielding the same age. If several cogenetic minerals (or fractions of single minerals) have the same D_t/R_{ref} value (i.e., they were precipitated from an isotopically homogeneous fluid or crystallized from an isotopically homogeneous magma), but different N_0/D_{ref}, they will plot along the same line that intersects the D/R_{ref} axis at the D_t/R_{ref} value and has slope m (Fig. 32a). By determining the slope of the isochron it will therefore be possible to calculate an age substituting Eq. (26) into Eq. (24), which gives

$$t = \frac{1}{\lambda}\ln(m+1) \tag{27}$$

and obtain D_t/R_{ref} as the intercept of the isochron on the y-axis (Fig. 32a).

In (b) a Pb—Pb isochron is shown, i.e., an isochron constructed using only radiogenic isotopes. This isochron can be constructed only for Pb isotopes, because only in the U—Pb system there are two radiogenic isotopes of the same element, Pb, that are generated

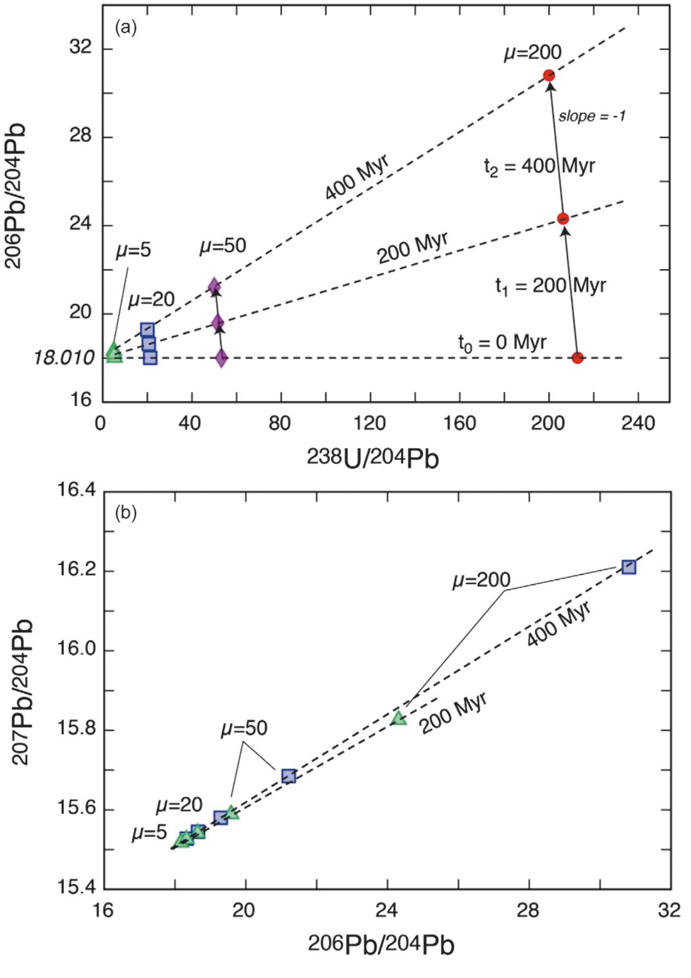

Fig. 32 U—Pb (a) and Pb—Pb (b) isochron plots. In (a) a "conventional" isochron plot is shown in which the x- and y-axes correspond, respectively, to the radioactive parent and radiogenic daughter both divided by a non-radiogenic isotope of the daughter element. Here the example is shown for the ^{238}U-^{206}Pb decay system, but the same plot can be used for, e.g., ^{187}Re-^{187}Os, ^{87}Rb-^{87}Sr, ^{147}Sm-^{143}Nd. In (a) an isochron is generated by cogenetic minerals from the same mineralization or different domains of the same minerals (e.g., stepwise leaching) that are characterized by the same initial ^{206}Pb/^{204}Pb ratio at the time t_0 of the mineralization, but by different ^{238}U/^{204}Pb values (i.e., different μ values). With time, the ^{238}U/^{204}Pb ratio decreases because of the radioactive decay of ^{238}U whereas the ratio ^{206}Pb/^{204}Pb increases by the same amount (because the number of disintegrated ^{238}U isotopes ultimately decay to the same number of radiogenic ^{206}Pb isotopes). For this reason, the slope of the decay lines in the plot is –1 (in absolute value). After $t_1 = 200$ Myr and $t_2 = 400$ Myr the different minerals/mineral fractions are aligned along straight lines which slope depends on the elapsed time and intersect the y-axis always at the same initial ^{206}Pb/^{204}Pb value.

by decay of two radioactive isotopes of the same element, U. The example shows how the same minerals/mineral fractions shown in (a) would yield a Pb—Pb isochron in the Pb—Pb space.

In order to obtain a linear regression at least two samples should be analyzed, but two- and three-point regressions have very limited statistical significance (e.g., Ludwig, 2001).

Robustness and precision of the regression of an ideal isochron (i.e., without any disturbance of the system) depend on (e.g., Chiaradia, 2023): (i) the spread of the points along the isochron (the wider the spread the lower the uncertainty on the isochron age), (ii) the analytical uncertainty of the isotope ratios of each analysis (the lower this uncertainty the lower the uncertainty on the age), and (iii) the number of points defining the regression. In many applications of isochron methods in geochronology, the different points of a linear regression are represented by different but cogenetic minerals. The use of different minerals ensures that they have a broad range of parent/daughter ratios which is a prerequisite to obtain a spread of points along the regression.

The use of Eq. (27) requires that the minerals used for the regression have remained closed systems since their formation and that they have formed coevally incorporating the radiogenic isotope from the formation environment (fluid) in the same ratio to the non-radiogenic isotope (e.g., the $^{206}Pb/^{204}Pb$ ratio of all minerals at time 0 is 18.010 in Fig. 33a), i.e., they must be formed by an isotopically homogeneous hydrothermal fluid, in the case of hydrothermal mineral deposits. It should be noted that the precision of the isochron dating method is usually poorer than dating of minerals which incorporate no or very little initial daughter isotope, e.g., U—Pb dating of zircon, Re—Os dating of molybdenite, $^{40}Ar/^{39}Ar$ (K—Ar) dating of K-bearing minerals.

Isochrons have been used for the Re—Os, U—Pb, Rb—Sr, Sm—Nd, Lu—Hf systems. The convention is to plot on the y-axis the ratio of the radiogenic to non-radiogenic reference isotope (i.e., $^{187}Os/^{188}Os$, $^{206}Pb/^{204}Pb$, $^{207}Pb/^{204}Pb$, $^{87}Sr/^{86}Sr$, $^{143}Nd/^{144}Nd$, $^{176}Hf/^{177}Hf$) and on the x-axis the ratio of the radioactive nuclide to the stable non-radiogenic nuclide of the daughter (i.e., $^{187}Re/^{188}Os$, $^{238}U/^{204}Pb$, $^{235}U/^{204}Pb$, $^{87}Rb/^{86}Sr$, $^{147}Sm/^{144}Nd$, $^{176}Lu/^{177}Hf$) (Fig. 31a).

Pb—Pb isochrons

All the above conventional isochrons require precise and accurate measurement of the number of atoms of both the radioactive parent and radiogenic daughter (Fig. 32a) which can only be achieved using Isotope Dilution (see above and Faure and Mensing, 2005; Dickin, 2005). The unique feature of the U—Pb system, with two radioactive nuclides of the same element (^{238}U, ^{235}U) decaying to two stable radiogenic isotopes of the same element (^{206}Pb, ^{207}Pb) allows us to obtain isochrons in the stable radiogenic Pb—Pb isotope space without the need of quantifying daughter and radioactive parent amounts (Fig. 32b), i.e., simply using radiogenic to non-radiogenic isotope ratios of Pb, which do not require the Isotope Dilution approach.

Present-day Pb isotope signatures are the sum of the initial Pb incorporated by the system (mineral or rock) plus the in situ grown radiogenic component due to U incorporation at the moment of formation of the system. If in a specific geologic context different samples have incorporated initial Pb with the same isotopic composition but have different U/Pb ratios, after a certain time t they will be aligned along a straight line which is an isochron characterized by a slope m

$$m = \frac{1}{137.88}\left[\frac{e^{\lambda^{235}t} - 1}{e^{\lambda^{238}t} - 1}\right] \tag{28}$$

where t is the time and λ^{238}, λ^{235} are the decay constants of ^{238}U and ^{235}U to ^{206}Pb and ^{207}Pb, respectively (Fig. 32b). This equation can be solved for t by obtaining the slope of the regression line in the $^{207}Pb/^{204}Pb$ versus $^{206}Pb/^{204}Pb$ space and then interpolating it with slopes obtained by substituting into Eq. (28) a series of values of t.

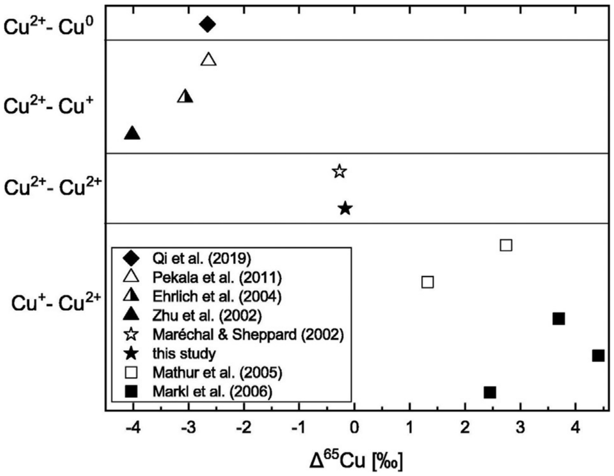

Fig. 33 Redox-dependent fractionation factors associated with different copper species. From Plumhoff AM, Mathur R, Milovský R and Majzlan J (2021) Fractionation of the copper, oxygen and hydrogen isotopes between malachite and aqueous phase. *Geochimica et Cosmochimica Acta* **300**: 246–257.

In some cases, Pb—Pb isochrons of a single mineral can be obtained by sequentially leaching the mineral and extracting different proportions of radiogenic and common lead from it (e.g., Frei and Kamber, 1995). The Pb—Pb isochron method of dating has been applied to various ore minerals, like sulfides and oxides, especially from IOCG, skarn and orthomagmatic deposits.

Dating approaches

We can distinguish three main cases when trying to date a mineral deposit:

1. Methods that directly date ore minerals (e.g., sulfides, oxides) or mineralization-related fluids;
2. Methods that date hydrothermal minerals that are paragenetically associated with ore minerals as a result of fluid-rock interaction or co-precipitation from the hydrothermal fluid;
3. Methods that date minerals allowing upper and lower age bracketing of the ore event.

Methods directly dating ore minerals and ore fluids

Re—Os is the most precise and accurate method for directly dating ore minerals (Stein et al., 2001; Markey et al., 2003), because Re, being a siderophile to chalcophile element, is incorporated to variable extents into sulfide minerals. This method allows high precision dating of molybdenite (MoS_2) through Eq. (9) and a variety of sulfides and sulfosalts (pyrite, chalcopyrite, etc.; Morelli et al., 2007; Saintilan et al., 2018) through the isochron method. The Re—Os method is very versatile and allows dating of a broad range of mineral deposits because of the widespread occurrence of molybdenite and other Re-bearing sulfides in a great variety of geological environments (e.g., porphyry systems, stratiform Cu deposits, IOCG, VHMS, MVT deposits: Ruiz and Mathur, 1999; Stein et al., 2001; Li et al., 2017; Saintilan et al., 2018; Liu et al., 2015a, 2015b; Requia et al., 2003; Nozaki et al., 2014). U—Pb dating of cassiterite has been extensively and successfully applied to directly date Sn deposits (e.g., Yuan et al., 2011) and U—Pb dating of hematite has been applied to date directly IOCG deposits (Courtney-Davies et al., 2019, 2020).

Other methods have been used with variable success for directly dating ore minerals. Although these methods may yield less precise and accurate ages because often based on the isochron method (see above), on parent-daughter systems that are less robust than U—Pb and Re—Os, or on fluid inclusions with poor petrographic control, they are worth mentioning because they are the only ones applicable to some types of deposits notoriously difficult to date. These include Rb—Sr isochrons on sphalerite to date MVT deposits (e.g., Nakai et al., 1993; Christensen et al., 1997), although debate exists on the geological meaning of these ages and ages using this method have not been reported recently, on sulfosalts to date Carlin-type deposits (Tretbar et al., 2000), and on pyrite to date lode-gold deposits (Li et al., 2008). Sm—Nd isochron dating on sphalerite, galena and pyrite has been carried out to date stratabound Pb—Zn—Ag deposits (Jiang et al., 2000) and on scheelite ($CaWO_4$) to date W and Au deposits (e.g., Eichhorn et al., 1997; Anglin et al., 1996; Zhang et al., 2019). Pb—Pb isochrons on sulfides and oxides (Frei and Kamber, 1995; Requia et al., 2003), $^{40}Ar/^{39}Ar$ dating of pyrite (Smith et al., 2001) and sphalerite (Qiu and Jiang, 2007), as well as U-Th/He dating of Fe-oxides (Wernicke and Lippolt, 1994) are other methods that can potentially be used for directly dating deposits where more reliable methods of dating are not available.

Methods dating hydrothermal alteration associated with mineralization

K-bearing alteration minerals (e.g., amphibole, biotite, adularia, muscovite, alunite, illite, and various other clay minerals) are almost ubiquitously associated not only with porphyry system mineralization and with low sulfidation epithermal deposits, but also with other types of mineralization (orogenic gold, Carlin-type, VHMS) and therefore they have been widely used for dating hydrothermal activity associated with various types of mineralization using the $^{40}Ar/^{39}Ar$ dating method (e.g., Henry et al., 1997; Marsh et al., 1997; Arehart et al., 2003). The $^{40}Ar/^{39}Ar$ system, due to its low closure temperature in the majority of datable minerals (Fig. 27), records the time at which a certain mineral has cooled below its closure temperature. Closure temperatures for the most commonly dated K-bearing minerals range between 550 °C and 200 °C (Fig. 27), which is a range of temperatures encompassing a wide variety of geological processes. Therefore, this method is sensitive not only to post-ore events during which temperatures may rise above the closure temperatures of these minerals, but also to a protracted thermal anomaly, e.g., induced by subsequent magma intrusions (Chiaradia et al., 2013). In such cases the date obtained will correspond to the time when the temperature drops below the closure temperature of the K-bearing mineral which may be variably later than its time of formation. In other cases, the K-bearing mineral may form at a temperature similar to its closure temperature and/or the cooling rate may be sufficiently rapid that the cooling age virtually coincides with the crystallization time of the mineral. $^{40}Ar/^{39}Ar$ dating of hydrothermal quartz fluid inclusions (Kendrick et al., 2001) offers another possibility to date ore-related fluids in gangue minerals.

U—Pb dating of hydrothermal titanite, zircon, hematite, rutile, monazite, xenotime, allanite, and U—Pb isochron dating of garnet may allow precise dating of different mineralization types like skarns, VHMS, orogenic gold-type and granitoid-related gold deposits among others (e.g., Vielreicher et al., 2003; Schaltegger, 2007; Chiaradia et al., 2009; Fielding et al., 2017; Zhou et al., 2017; Wafforn et al., 2018; Schirra and Laurent, 2021). U—Pb isochrons have been applied to date hydrothermal carbonates associated with MVT mineralization (Grandia et al., 2000).

Rb—Sr isochron dating of hydrothermal minerals (biotite, muscovite) has been used in the past but has the same problems of closure temperatures as $^{40}Ar/^{39}Ar$ (Fig. 28) with the additional caveat that it is less precise (see above). Rather precise Rb—Sr isochron dating of quartz-hosted fluid inclusions (Li et al., 2008) has also been reported. Sm—Nd dating of fluorite and calcite has been successfully applied to date Carlin-type mineralization (Tan et al., 2019) and Sm—Nd dating of tourmaline has been applied to date stratabound Pb—Zn—Ag mineralization (Jiang et al., 2000).

Bracketing

Dating geological events that temporally bracket the time of the mineralization is an alternative approach to direct dating of ore or hydrothermal minerals associated with the mineralization. The most common case is dating magmatic events that, through stratigraphic or cross-cutting relationships, are demonstrably pre- or *syn*- and post-mineralization. For instance, U—Pb dating of zircon has been used to bracket age and duration of magmatic hydrothermal activity associated with porphyry-type mineralization by dating pre- to syn- and post-ore porphyry intrusions (e.g., Von Quadt et al., 2011). The same method, applied to dating volcanic rocks occurring in the stratigraphic footwall and hanging-wall of strata-bound VHMS mineralization, has also been used to bracket the age of VHMS mineralization (e.g., Barrie et al., 2002).

Transition metal stable isotopes

Since the advent of Multi-Collector Inductively Coupled Plasma Mass Spectrometry (MC-ICPMS) in the late 1990s stable metal isotope geochemistry studies have covered applications ranging from the biological, archeological, chemical, and metallurgical fields to the geological applications discussed there. Ore metal commodities, like Ti, V, Fe, Ni, Cu, Zn, Mo, Ag, Cd, Sb, Sn, Hg and Te, have stable metal isotopes with measurable mass dependent isotopic fractionation recorded in a diverse set of minerals (sulfides and oxides) and surface/ground fluids. The order of the isotopic shifts is in the 0.1 to 10‰ range at a maximum (where the ‰ value indicates the per mil deviation of a specific isotope ratio measured in a sample compared to the same isotope ratio measured in an appropriate standard). Most values cluster within ±4‰ of the standards, thus sufficient 'isotopic breadth' exists to explore physicochemical processes and potentially identify sources of metals. Due to the fact that Cu, Fe, and Zn have received the bulk of attention to date, in the following we discuss the isotope systematics of these three transition elements and how they can be used for mineral exploration and ore genesis questions.

The obvious importance of stable metal isotope analysis is that information from the commodity can be directly inferred with these data. Many geochemical techniques provide information about the alteration silicate minerals or fluids that are in the alteration silicates. These are important data, however, information directly obtained from the metals of interest is essential for genetic models of ore deposits and for their exploration.

The measurement of stable metal isotope ratios has required developments both on the chemical separation techniques of these metals and on the mass spectrometry and correction schemes for mass bias corrections. Both these technologies are continuously evolving. For the separation techniques, the most important aspect is that the purification process does not induce fractionation of metal isotopes. This could potentially occur in the dissolution steps, drying steps and during the ion exchange chromatography. Multiple examples exist in the literature for each step and how metals are treated throughout. Typically, method papers accompany each isotope system and provide pathways for analysis. In general, the resins used in ion exchange chromatography can induce metal isotopic fractionation, thus careful yield calculations must be employed or a double spike must be used to account for this potential pitfall. For sulfides enriched in the element of interest, systems like copper isotope analysis of copper sulfides or native copper does not require chromatography. However, most published work used some procedure to purify the chemical matrix prior to analysis in the mass spectrometer.

For the mass spectrometry, the major issue is establishing a means to monitor isotope fractionation induced by the instrument. Traditional standard-sample-standard bracketing was employed at the start for metal isotope analysis. Next, doping of the unknown samples with elements in a similar mass range, with a similar ionization potential and known stable isotope ratios was employed with success and finally double spikes for elements with sufficient amounts of isotopes were used. Combinations of each correction technique are used currently.

Synchronous with the establishment of different mass bias correction schemes, is the development of different metal isotope standards for interlaboratory comparison. Multiple isotope systems use NIST generated standards as a means to compare all of the data. For some of the NIST standards, absolute isotopic values are not provided, however comparison of data to the same material provides a means for the community to use and compare data. Some groups provide international standards, like the Lyon Zn standard (Moynier et al., 2005, 2017) and the ETH Zn standard (Archer et al., 2017). Isotope values are reported relative to these standards and normalized.

Mass dependent isotope fractionation in elements with more than two stable isotopes, e.g., Ti, V, Fe, Ni, Zn, Mo, Ag, Cd, Sn and Te, has been reported and is used to demonstrate the robustness of the measurements. In contrast, monitoring mass dependent fractionation in elements with only two isotopes, like Cu, Ag, and Sb, is not possible. Data are traditionally presented in the ‰ (third decimal place shifts or δ notation)

$$\delta^{XX}\mathrm{Element} = \left(\left(\frac{\left(\frac{xxElement}{xxElement}\right) sample}{\left(\frac{xxElement}{xxElement}\right) standard}\right) - 1\right) * 1{,}000 \tag{29}$$

and (forth decimal place shifts or ε notation)

$$\varepsilon^{XX}\mathrm{Element} = \left(\left(\frac{\left(\frac{xxElement}{xxElement}\right) sample}{\left(\frac{xxElement}{xxElement}\right) standard}\right) - 1\right) * 10{,}000 \tag{30}$$

The heavier isotope is reported in the numerator of the ratios so that positive values indicate enrichments of the heavier isotope and negative values indicate enrichment of the lighter isotope with respect to the standard value. The majority of metal isotope papers use the δ notation above while the first papers used the ε notation because the fractionation of metal isotopes was not thought to be significant.

Modeling of the transition metal isotope data from natural samples involves several different strategies since both equilibrium and kinetic processes cause stable isotope fractionation (see above). Most papers provide or cite experiments that constrained a fractionation mechanism and the associated fractionation factor (α) defined as

$$\alpha_{z-y}\frac{1000 + \delta xxElement\ z}{1000 + \delta xxElement\ y} \tag{31}$$

where z and y are components (e.g., vapor, aqueous fluid, mineral) in a defined system. The fractionation factors are applied in open system Rayleigh distillation models using equations based on the following expression:

$$\frac{R}{Ri} = \mathrm{F}^{(\alpha-1)} \tag{32}$$

where R is the isotope ratio, i is the initial ratio, F is the fraction of a remaining component and α is the fractionation factor. The distillation models with chosen fractionation factors 'fit' data and show how different fractionation factors identify mechanisms which relate to specific processes. The most difficult value to constrain in natural systems is F, thus many different creative approaches have been used to constrain this important variable in the calculations.

Copper

Background and methods

Copper displays the largest range of all the stable metal isotope values reported in the literature with δ^{65}Cu > 10‰. The data provided here are reported relative to the NIST-976 copper isotope standard and since this was consumed several other copper standards of similar isotope composition have been reported (Hou et al., 2016; Yuan et al., 2017; Zhang et al., 2020). Copper has two isotopes (^{63}Cu and ^{65}Cu) and the first attempts for measuring copper isotope fractionation date back to the early 1960s by Shields et al. (1965). In the late 1990s and early 2000s, the first papers with measurements from MC-ICPMS were reported. Marechal et al. (1999) and Marechal and Albarede (2002) provided a robust chemical separation technique using BioRad MP-1 HCl-based resins along with a doping technique where Zn isotope values were correcting the Cu isotope data through an exponential correction. At about the same time, Zhu et al. (2000, 2002) reported data on several copper-rich ore samples corrected using standard-sample-standard bracketing.

These pioneering papers set the stage for developing more techniques to separate copper from complex silicate and organic matrices as well as development of different schemes for mass bias correction. The most obvious problems with measuring Cu are isobars, both on mass 63, like ^{23}Na^{40}Ar, and on mass 65, like ^{25}Mg^{40}Ar. Significant advances have been made in chemical separations to eliminate isobars and provide robust measurement of copper isotope values in silicates (Bigalke et al., 2009; Chapman et al., 2006; Liu et al., 2014a; Peel et al., 2008; Pokrovsky et al., 2008; Sossi et al., 2015), organic materials (Larner et al., 2011; Navarrete et al., 2011; Sullivan et al., 2020), and salts from dried waters (Archer and Vance, 2004; Bermin et al., 2006; Borrok et al., 2007, 2008; Kidder et al., 2020; Little et al., 2014; Vance et al., 2008). Equally important advances in the mass spectrometry and mass bias corrections have been made using elements like nickel (Maher, 2005; Sossi et al., 2015) and gallium (Hou et al., 2016; Zhang et al., 2020) that have ionization potentials that match copper more than zinc. The errors generated with these data are lower at approximately 0.03–0.05‰, in contrast to errors associated with simple standard-sample-standard bracketing at 0.07–0.12‰. From an analytical standpoint, both errors allow for resolution of isotopic differences for most geological samples.

Use in mineral exploration

Mineral exploration activities focused on identifying buried resources use geochemical signatures in surface/ground waters, soils, Fe-oxides that are the residues of sulfide weathering and the ore-related sulfide minerals. Copper isotope compositions of all these materials have been presented in the literature to date.

Ground and surface waters that interacted with copper mineralization along their path provide a direct means to monitor favorable commodity mineralogy at depth. Copper isotope signals in these media show the greatest potential to identify hidden copper resources because of the redox sensitivity of copper. Oxidation of copper sulfide minerals favors the heavier ^{65}Cu isotope. Multiple experiments at low temperature demonstrate that leaching of chalcopyrite (Borrok et al., 2008; Kimball et al., 2009; Li and Liu, 2022; Mathur et al., 2005), chalcocite (Mathur et al., 2005; Wall et al., 2011a), and bornite (Wall et al., 2011b) generates leached copper-rich solutions that possess heavier copper isotope compositions than the starting sulfide mineral. In contrast, minerals that possess oxidized copper do not fractionate copper to a significant degree as seen in the experiments and expressed as fractionation factors in Fig. 33 (Plumhoff et al., 2021). These geochemical reactions with natural waters and copper sulfides have been argued and modeled to generate different copper isotopic reservoirs (Fig. 34) where oxidized Cu appears in natural waters: the residues are isotopically lighter in leached rocks and soils and the primary copper sulfide mineralization is approximately 0‰ (Mathur and Fantle, 2015).

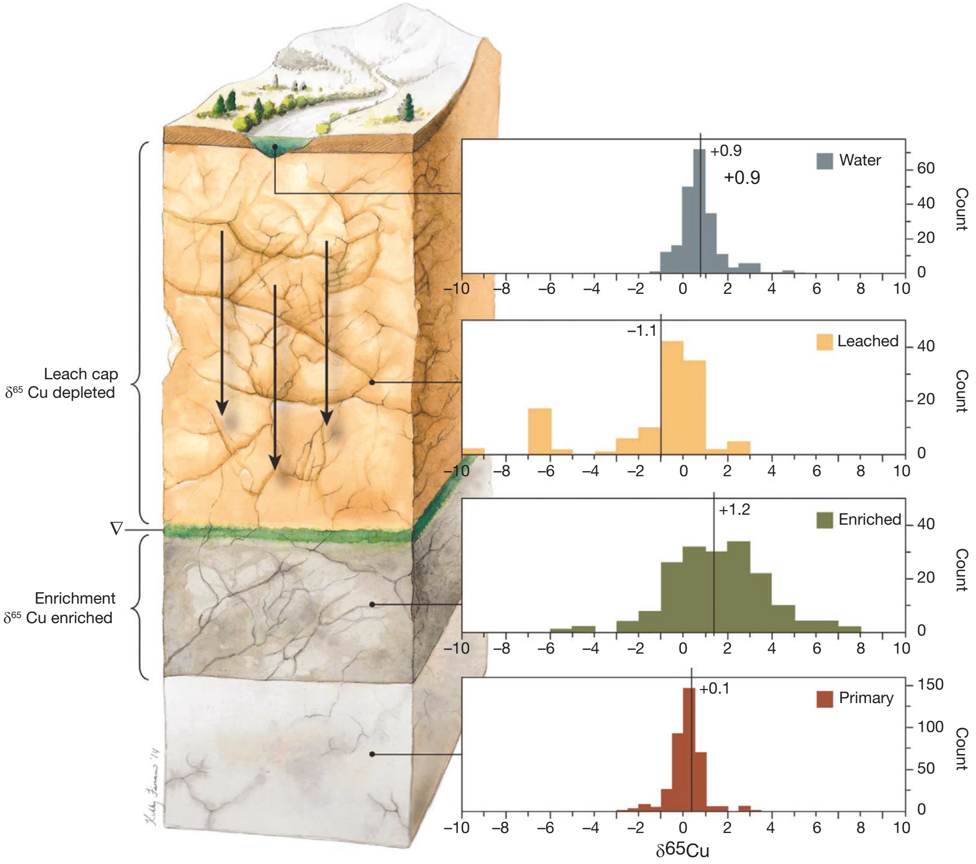

Fig. 34 Distinct copper isotope reservoirs developed by the redox of copper sulfides. Note that the waters have a distinctly higher copper isotope value in comparison to leached rocks/soils and the primary sulfides from where they potentially originated. From Mathur R and Fantle MS (2015) Copper isotopic perspectives on supergene processes: Implications for the Global Cu cycle. *Elements* **11**(5): 323–329.

For the technique to operate, the kinetics of the reactions control the isotope fractionation because equilibrium is most likely not achieved in the critical zone or slightly deeper. Several papers have demonstrated that the equilibrium reactions associated with precipitation of different copper sulfides at low temperature can induce significant copper isotope fractionation. Redox has been shown to cause the greatest degree of copper isotope fractionation whereas other variables like pH, changing temperatures, biological activity, and adsorption cause lower degrees of copper isotope fractionation (Balistrieri et al., 2008; Fujii et al., 2013; Guinoiseau et al., 2018; Liu et al., 2021; Navarrete et al., 2011; Pokrovsky et al., 2008; Seo et al., 2007). Similar variables along with vapor induced fractionation at higher temperatures occur (Maher et al., 2011; Syverson et al., 2021) and will be discussed later.

To date, eight published studies have demonstrated that elevated copper isotope values found in surface and groundwaters can be tied to weathering of copper sulfide buried at depth. Both exploration geochemical (Kidder et al., 2021; Mathur et al., 2013, 2014) as well as environmental geological applications (Borrok et al., 2008; Kimball et al., 2009; Song et al., 2016) document this reaction happening in nature. Fig. 35 demonstrates the spatial patterning of the copper isotope values of seep waters in the Pebble deposit in Alaska where the known area of copper mineralization has an elevated copper isotope value. Groundwaters show the same potential in the Cloncurry mineral district, Australia (Fig. 36). These examples from Alaska and Australia demonstrate that values between +1.5 and +4‰ cluster near mineralization areas that possess known copper sulfides. This range mimics experimental work referenced above and the strong patterning of copper isotope composition and known mineralization provides evidence for the efficacy of the technique.

The values that are higher and lower than those associated with copper sulfide weathering could be related to a variety of interconnected processes, ranging from adsorption to biological activity to different minerals carrying copper that are the result of weathering. Due to the extremely low Cu concentrations these effects could be comingling and potentially difficult to interpret. The Cloncurry dataset does not permit for distinction of any of these processes specifically, however it is known that copper could fractionate to this degree given the geological environment from which the groundwaters were derived (Boujelben et al., 2009; Fariña et al., 2018; Liu et al., 2014a, 2014b, 2022; Navarrete et al., 2011; Pokrovsky et al., 2008). Given this obvious complexity, the sampling strategy and proximity of known copper mineralization establishes the utility of this technique in this area. To properly apply the technique in unknown areas of mineralization, ideally waters from known areas could be used to establish ranges as exhibited here to constrain what mostly represents copper derived from sulfide weathering.

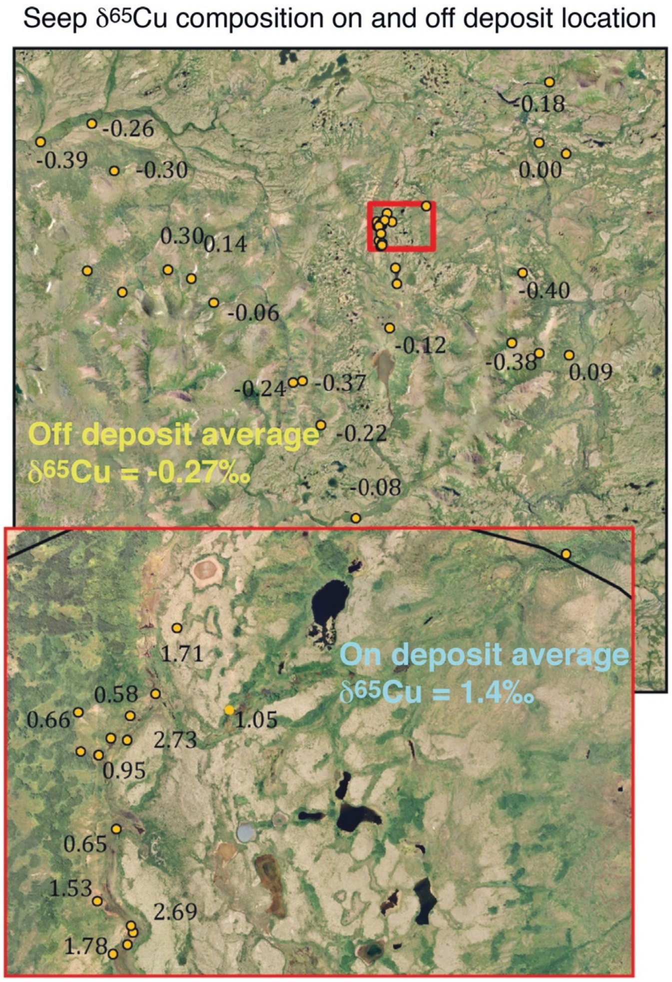

Fig. 35 Copper isotope compositions of seep waters on and near the Pebble deposit in Alaska. The red square indicates the location of the deposit and the higher copper isotope values are located on the deposit. Data are from Mathur et al. (2013).

The most plausible explanation for the higher Cu isotope values found in the groundwaters here could be tied to weathering of pyrite. The only known solids measured at the higher values seen in these waters are copper isotope compositions in hydrothermal pyrite. Fig. 36 demonstrates the overlap among these values. Without measuring multiple pyrite samples from these systems, no complete connection can be verified. However, four facts would suggest that pyrite and distal pyrite should possess heavier copper isotope compositions because (1) the known copper isotope fractionation mechanisms in hydrothermal systems favor the heavier isotope in the vapor phase, thus the higher copper isotope values are traditionally found in the distal parts of systems, (2) oxidized Cu^{++} favors ^{65}Cu, (3) Cu^{++} most likely substitutes for Fe^{++} in pyrite (Reich et al., 2013; Tardani et al., 2017), and (4) heavier copper isotope compositions were reported in pyrite from a porphyry copper and skarn deposits (Song et al., 2016; Su et al., 2018). The congruence of these factors suggests that heavier copper should be present in pyrite and could be the cause for the higher values found in the waters.

Importantly, values >+4.4‰ form a 'halo' around the cluster of mineral deposits (Eliose, Jericho and Maranon). These values could indicate weathering of pyrite of the hydrothermal systems associated with copper deposition. Given the circular plan view geometry of these values around known mineralization, the fingerprint of the 'economic' mineralization could be extended to 5 km distance from the known ore mineralization. Sizes of hydrothermal systems associated with mineralization are known to have footprints on this scale and these data could indicate weathering of distal pyrites associated with mineralization. Therefore, the copper isotope signals could potentially be used to indicate mineralization within a 5 km radius of mineralization.

As seen in Fig. 37, copper concentrations in the parts per trillion range possess copper isotope signals that indicate copper sulfide weathering. Clearly, even at the lowest concentration level measured in groundwaters, the copper isotope compositions provide relevant and important information. Therefore, the use of the copper isotope signals shows potential in low copper concentration solutions of both surface waters (Pebble example) and groundwaters (Australian example).

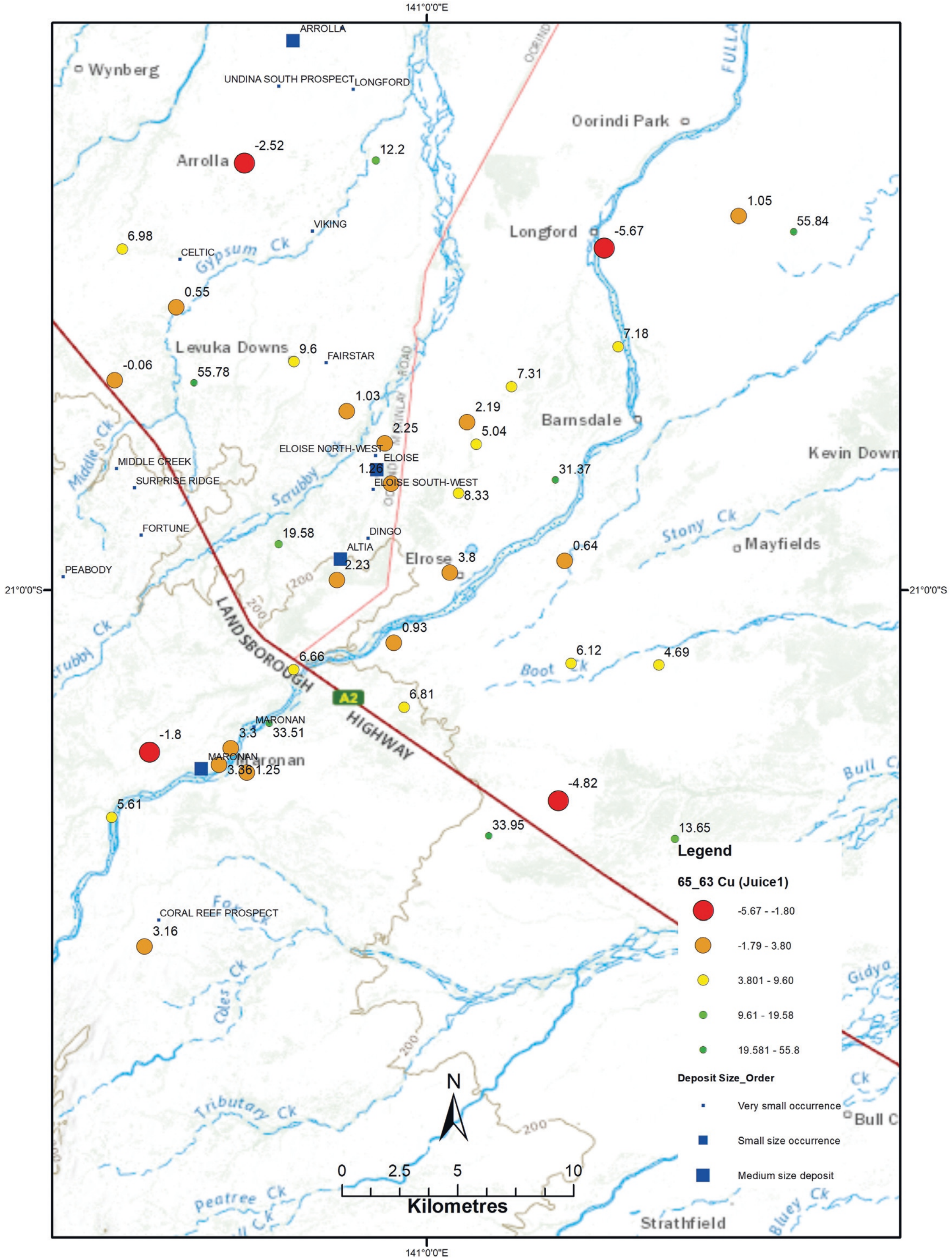

Fig. 36 Copper isotope compositions (δ^{65}Cu = 65_63) of deep groundwaters from the Cloncurry mineral district in Australia. From Mathur R, Mahan B, Godfrey L, Degeling H, Tang J, Dirks P, Rea P, Paitl K and Lasinsky C (2023) *Queensland Geological Report 2023/01*.

Copper isotopic fractionation during weathering can also be used in the leached remains of sulfide minerals in leach caps. Interpretation of limonite species in surficial weathering profiles has long been practiced to evaluate the potential for underlying supergene copper enrichment in porphyry environments, with varying degrees of success. A study by Braxton and Mathur (2014) revealed a broad range of δ^{65}Cu copper isotopic values for supergene phases between −27 and +6‰, representing the largest degree of fractionation measured in one deposit to date. Significantly, copper isotope values from Quellaveco's leached-cap iron oxides

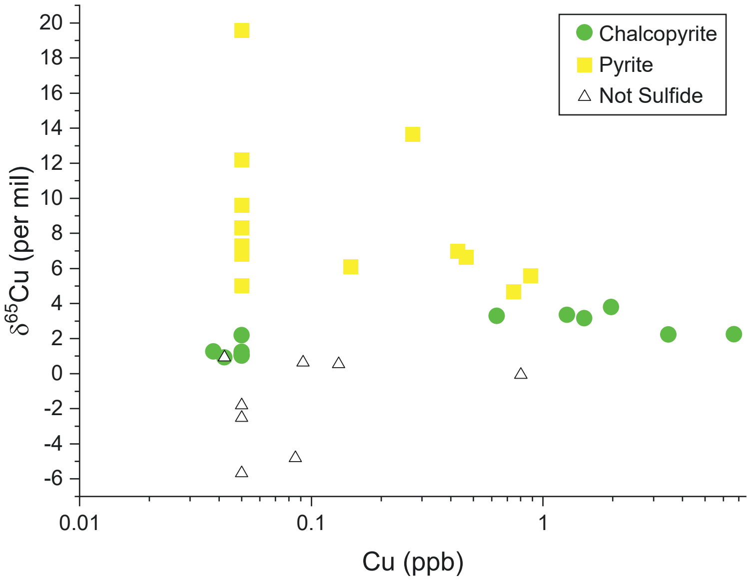

Fig. 37 Copper concentration versus copper isotope values for groundwater. Note that the concentrations of copper in most samples are less than a part per billion. From Mathur R, Mahan B, Godfrey L, Degeling H, Tang J, Dirks P, Rea P, Paitl K and Lasinsky C (2023) *Queensland Geological Report 2023/01*.

display systematic variation as a function of the supergene geological context and maturity of the underlying supergene enrichment. As seen in Fig. 38, limonites from Quellaveco showing weak isotopic depletion (δ^{65}Cu −5.0 to −1.0‰) correspond to areas of the leached cap overlying zones of moderate-strong copper enrichment, while those showing strong isotopic depletion (δ^{65}Cu <<−5‰) correspond to areas of the leached cap of the pyritic halo to the system. Leached cap limonites from Quellaveco showing moderate to heavy isotopic values (δ^{65}Cu >>+1‰) overlie zones where the sulfide enrichment blanket has been incised by erosion, and has experienced physical and isotopic re-working.

The copper isotopic patterns observed for leached cap limonites from Quellaveco are consistent with Rayleigh models describing leaching of variable amounts of copper from a hypogene (δ^{65}Cu near 0‰) or enriched (δ^{65}Cu > +2‰) copper sulfide zone (Braxton et al., 2009; Braxton and Mathur, 2011). The isotopically lightest values (δ^{65} Cu as low as −27‰), characteristic of limonites overlying the pyritic (5–10% pyrite) halo, reflect near-complete leaching of copper, a process consistent with the elevated acid-generating capacity that would attend the weathering of such material. The study results suggest that copper isotope analysis of supergene limonites represents a complement to, and an improvement upon, the traditional Fe-oxide studies in leach caps.

Multiple studies of soil profiles have been used from an environmental perspective to understand metal migration and contamination from various point sources (Babcsányi et al., 2016; Bigalke et al., 2009, 2010; Blotevogel et al., 2018; Dótor-Almazán et al., 2017; Fekiacova et al., 2015; Kusonwiriyawong et al., 2017; Liu et al., 2014b; Mathur et al., 2012a; Mihaljevič et al., 2018; Song et al., 2016; Vance et al., 2016). From an exploration geological angle, the most important aspect seen in all of these studies is that there are significant copper isotopic differences in soils and the processes related to metal movement in soils are complicated and intertwined. The soil studies point to a geochemically dynamic system with regards to copper isotope fractionation changing on a monthly to yearly interval. At the current time, no studies have shown distinct copper isotope signatures as a means to identify buried mineralization. This does not occlude the potential utility of soils, rather points to the true complexities associated with the bio-geo-chemical reactions in the soil profile.

Ore genesis processes and models

Copper isotopic analysis of minerals from both low and high temperature mineralization environments has provided key insights into processes associated with metal migration. Redox reactions have been pointed to as one of the main causes of copper isotope fractionation in all mineralization environments. However, biological, equilibrium, temperature, vapor, adsorption and other mechanisms have been identified and used to interpret the isotopic shifts present in minerals associated with mineralization.

The largest amount of copper isotopic fractionation measured in nature is in the supergene enrichment environments. Mathur et al. (2010) examined leach cap, enrichment and hypogene minerals. The porphyry copper deposits in Arizona (Silver Bell, Morenci, Ray) possess three different Cu reservoirs, each one with unique Cu isotope signatures, where the δ^{65}Cu values for leach cap minerals < hypogene minerals < supergene enrichment minerals. The pattern exists in all three deposits and most likely resulted from oxidative weathering of Cu at surface and reprecipitation of Cu at depth. Other processes could have contributed to the copper isotope signatures. Rayleigh distillation models with redox induced fractionation factors produce the Cu isotope patterns found in the leach cap and quantify the degree of leaching. A comparison of the isotopic composition of the three reservoirs among the three deposits reveals distinct differences: the Silver Bell mine possesses leach cap minerals that are more depleted in ^{65}Cu and enrichment minerals that are more enriched in ^{65}Cu than both the Morenci and Ray mines. A possible explanation for the

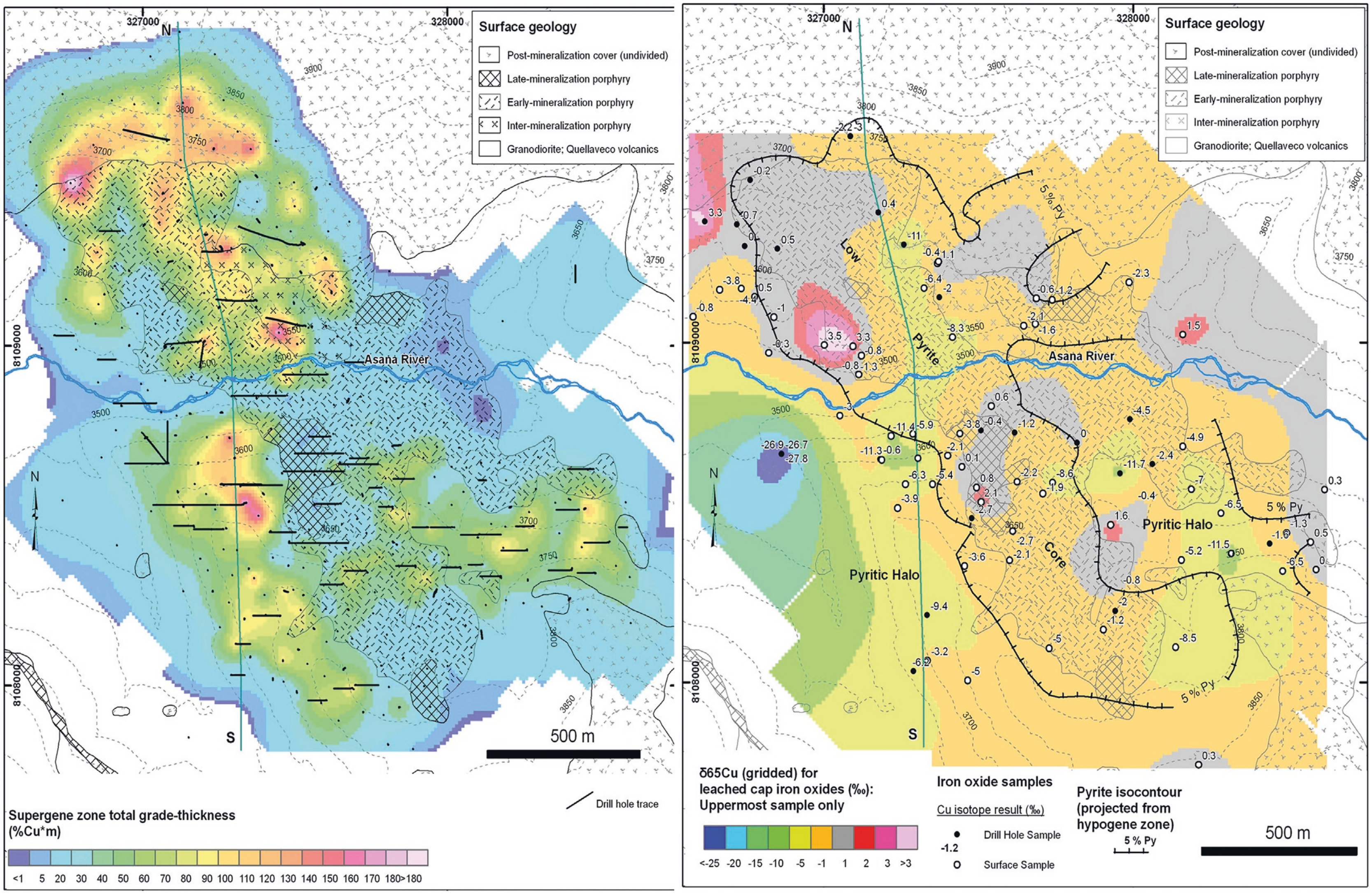

Fig. 38 Left panel shows copper enrichment grades and right panel shows Cu isotope compositions of Fe-oxides of the Quellaveco deposit in Peru. From Braxton DP and Mathur R (2014) Copper isotopic vectors to supergene enrichment: Leaches cap isotopic footprint of the Quellaveco porphyry copper deposit, southern Peru. In: *SEG Conference Proceedings, SEG 2014, Building Exploration Capability for the 21st Century.*

difference among the deposits could be that Silver Bell experienced a greater degree of leaching than Ray and Morenci. Palacios et al. (2011) present a similar dataset for the secondary and primary minerals at the Spence deposit in Chile. They also interpreted the +3‰ δ^{65}Cu values in chalcocite as a means to indicate significant degrees of supergene recycling of copper.

The importance of redox effects has been demonstrated in the sedimentary copper deposits. Multiple contributions (Asael et al., 2007; Asael et al., 2012; Asael et al., 2009; Dekov et al., 2013; Haest et al., 2009; Markl et al., 2006; Pękala et al., 2011) show how copper isotopes in chalcopyrite, bornite and copper oxides that formed in these environments are impacted by redox processes. Fig. 39 shows an Eh-pH diagram associated with Cl-rich fluids thought to be related to sedimentary copper deposition. The figure demonstrates how redox effects occur during the leaching of copper from oxidized sources and reduction during precipitation of copper minerals. Interestingly, Luczaj and Huang (2018) did not report large copper isotope fractionation (δ^{65}Cu of 0 ± 0.5‰) in Mississippi Valley type ores and interpreted the data to indicate lack of redox reactions throughout the mineralization process.

Significant copper isotope fractionation occurs in the highest temperature systems involving sulfide mineralization like mafic-ultramafic intrusions and associated deposits. Mantle partial melting and magmatic differentiation do not fractionate copper

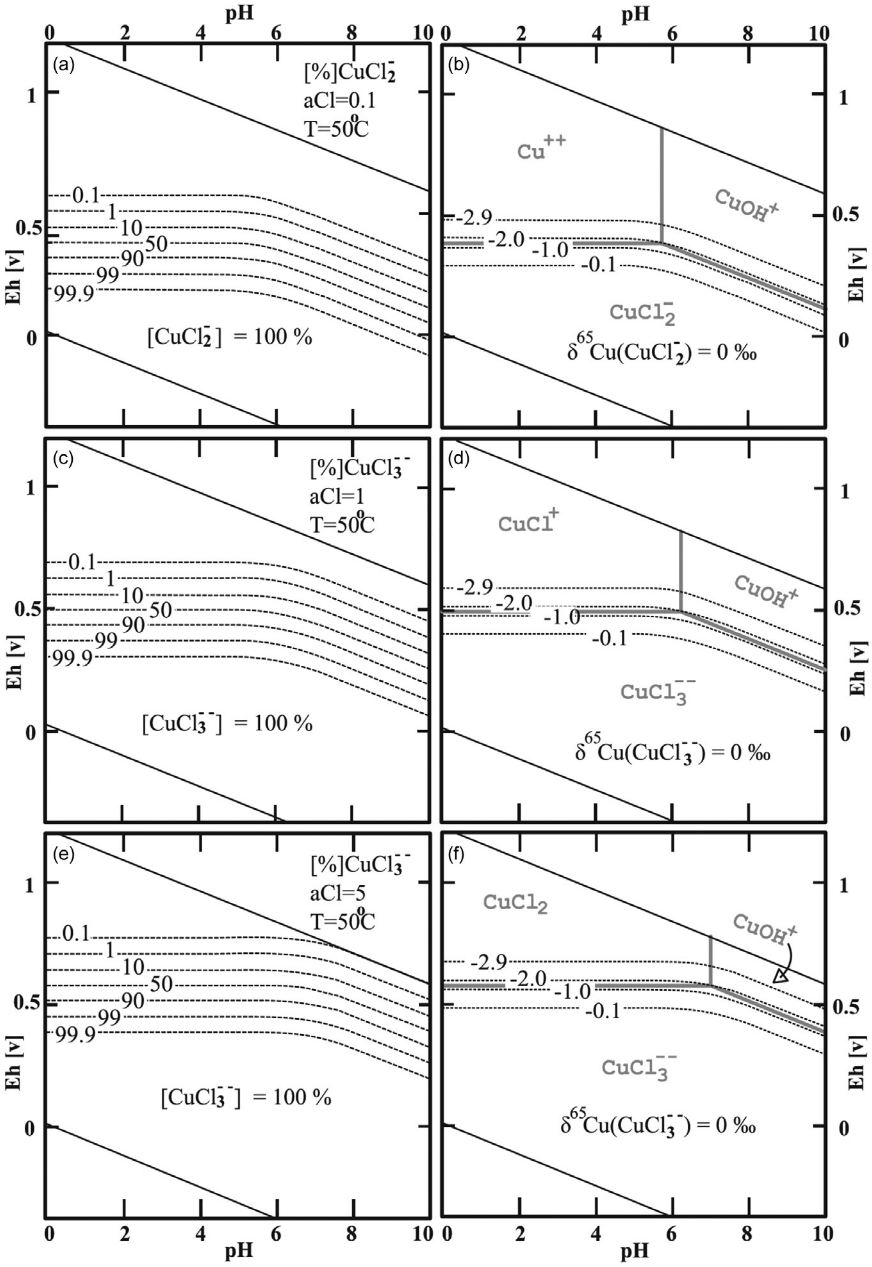

Fig. 39 Copper isotope fractionation controlled by Cl activity associated with the deposition of sedimentary copper deposits. From Asael D, Matthews A, Bar-Matthews M, Harlavan Y and Segal I (2012) Tracking redox controls and sources of sedimentary mineralization using copper and lead isotopes. *Chemical Geology* **310–311**: 23–35.

to a large degree as evidenced by a large set of peridotites, basalts and subduction-related andesites and dacites that match the bulk silicate Earth (BSE), which has an average δ^{65}Cu value of around 0.06‰ (Huang et al., 2016a; Liu et al., 2015a, 2015b; Savag et al., 2015). However, hydrothermal alterations under high temperatures in the basaltic oceanic crust may result in significant Cu isotope fractionations (Guo et al., 2020; Guo et al., 2022; Huang et al., 2016b). Accordingly, mantle metasomatism and lower crustal rocks with involvement of recycled crustal materials strongly fractionate Cu isotopes, spanning a wide range of δ^{65}Cu values from −0.64‰ to +3‰ (Kempton et al., 2022; Liu et al., 2015a, 2015b). By analyzing native copper grains and whole rock copper in peridotite, Ikehata and Hirata (2012) demonstrated that no Cu isotope fractionation occurs without sulfide segregation. It seems that the addition of recycled crustal materials into the mantle source would result in obvious Cu isotope heterogeneity in the mantle source. The magmas derived from mantle partial melting are expected to inherit the Cu isotopic compositions of their sources.

Recent studies show that significant Cu isotope fractionation (δ^{65}Cu ~4‰) has been involved during the formation of magmatic Ni—Cu deposits (Malitch et al., 2014; Ripley et al., 2015; Smith et al., 2022; Tang et al., 2020; Zhao et al., 2022b; Zhao et al., 2019; Zhao et al., 2017). Many factors have been advocated to explain the large variation of Cu isotopes in these deposits, including different mantle sources, variable degrees of mantle melting, different magmatic processes, crustal contamination, and/or redox reactions (Malitch et al., 2014; Ripley et al., 2015; Zhao et al., 2017, 2019; Tang et al., 2020). The generation of magmatic Ni—Cu deposits involves a series of stages: (1) mantle melting; (2) magma ascent; (3) segregation of sulfide melt from silicate melt and sulfide enrichment; (4) silicate mineral crystallization and possible internal fractionation within segregated sulfide melt. Malitch et al. (2014) assert that the Cu isotopic variation of the deposits in the Noril'sk region may result from multiple magmatic processes, different magma pulses, or assimilation of Cu from external sources. The distinct difference in δ^{65}Cu values between the sheet-style and conduit-style mineralization in the Lake Superior area is likely caused by mantle sources, variable degrees of melting, sulfide retention, and sulfide liquid fractionation (Ripley et al., 2015; Smith et al., 2022). It is difficult to precisely evaluate the contribution of the factors causing significant Cu isotope fractionation in the mafic-ultramafic intrusions of the Noril'sk region and Lake Superior area, since these intrusions are in different locations with diverse country rocks. Zhao et al. (2017, 2019) reported a systematic Cu and Fe isotopes study of the Tulaergen Ni—Cu deposit, China. In this deposit, >2‰ variation of δ^{65}Cu values has been observed, and the potential influence from crustal contamination, hydrothermal overprinting, diffusion, mantle sources or magmatic processes are excluded (Zhao et al., 2017, 2019). On the basis of negative correlation between δ^{65}Cu and δ^{56}Fe values of chalcopyrite and positive correlation between δ^{65}Cu values of chalcopyrite and δ^{56}Fe values of whole-rocks, redox reactions are expected to be the main factor governing the Cu isotope fractionation in magmatic Ni—Cu mineralization system (Zhao et al., 2017, 2019). However, Tang et al. (2020) proposed that δ^{65}Cu values show no correlation with intrusion/orebody shape, location of sample in the orebody, lithofacies or type of mineralization in the Kalatongke and Baishiquan deposits (Central Asian orogenic belt). The large variation of Cu isotopic composition in these deposits is attributed to the degree of partial melting in the mantle source and associated magmas (Tang et al., 2020). Finally, Zhao et al. (2022a, 2022b) demonstrated a strong relationship between the fO_2 of the magmas and the copper ores found in several Ni—Cu deposits in China to augment the relationship among redox shifts causing predictable copper isotopic signals in ores (Fig. 40).

Perhaps the most studied mineralized systems by Cu isotopes are porphyry copper deposits and related hydrothermal mineralization such as skarns and epithermal gold deposits. Fig. 41 shows the general patterning of chalcopyrite recorded in porphyry copper deposits. Chalcopyrite in veins from cores of the systems associated with higher temperature alteration silicate minerals, like biotite and K-feldspar, has lower copper isotope values that cluster around 0‰ (Asadi et al., 2015; Braxton and

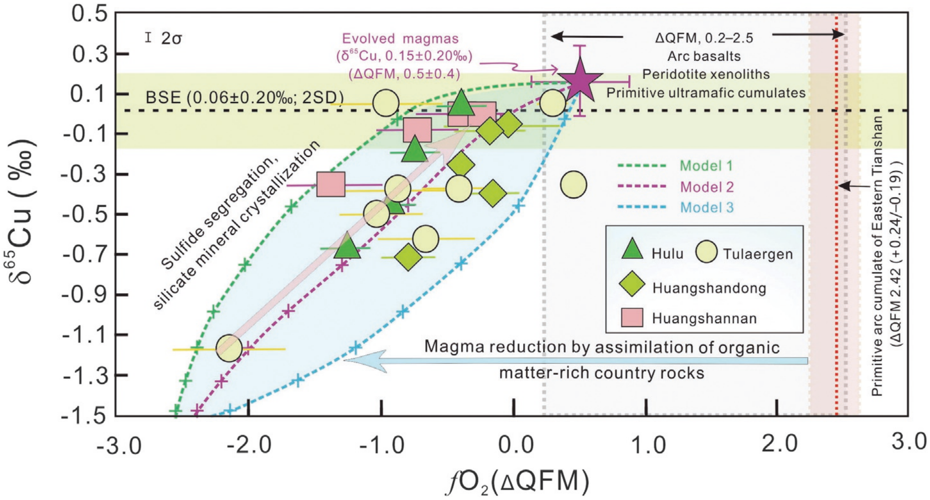

Fig. 40 Copper isotope values and estimated fO_2 of Cu—Ni deposits in China. From Zhao Y, Liu SA, Xue C, Mathur R, Symons DT and Ke J (2022b) Copper isotope fractionation in magmatic Ni–Cu mineralization systems associated with the variation of oxygen fugacity in silicate magmas. *Geochimica et Cosmochimica Acta 338*: 250–263.

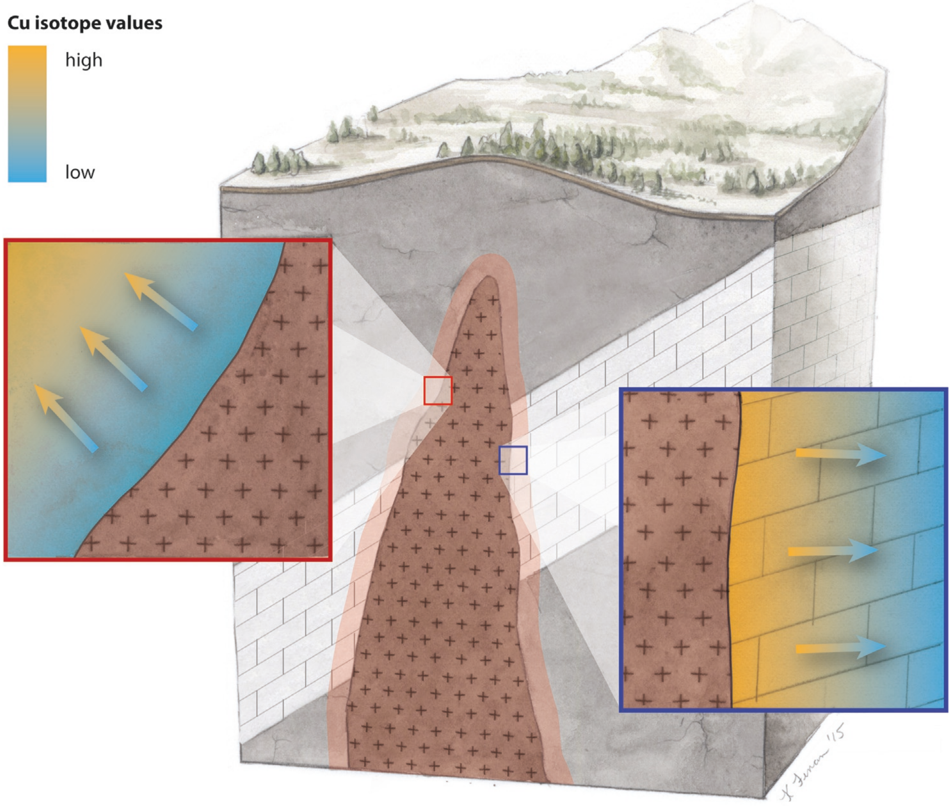

Fig. 41 Cross section demonstrating the vectoring patterns using the copper isotope compositions of chalcopyrite and bornite. From Mathur R and Wang D (2019) Transition metal isotopes applied to exploration geochemistry: Insights from Fe, Cu, and Zn. *Ore Deposits: Origin, Exploration, and Exploitation*, 163–183.

Mathur, 2011; Duan et al., 2016a; Graham et al., 2004; Gregory and Mathur, 2017; Li et al., 2010; Mathur et al., 2010; Mathur et al., 2018; Mathur et al., 2009; Mirnejad et al., 2010; Wall et al., 2010). In contrast, chalcopyrite in veins from distal parts of the systems, associated with lower temperature alteration silicate minerals like phyllite and kaolinite, have higher copper isotope values. Other copper-rich minerals, like bornite, also show similar patterns (Dendas, 2011). The fractionation associated with liquid-vapor partitioning in high temperature fluids coupled with equilibrium fractionation among copper-rich minerals has been modeled and determined experimentally to generate the observed patterning.

Skarns display an inverse pattern where the higher copper isotope values are found in the cores of the systems and the lower values are found in the outer parts (Larson et al., 2003; Maher et al., 2003; Yao et al., 2016). This inverse relationship is most likely related to the mechanisms that are fractionating copper during the formation of copper minerals from the hydrothermal solution. Maher et al. (2011) demonstrated with experimental data that pH, fO_2 and salinity were related to fluid-vapor formation of different copper species into the vapor phase. Thus, perhaps the difference in fractionation patterns between these two systems is related to metal transport with different ligands. For instance, CuCl species form in the acidic fluids associated with porphyry copper deposits in silicate rocks, in contrast CuCO species form in buffered reactions associated with skarn mineralization. The different bond strengths associated with the metal-ligand could lead to different fractionation factors during mineral precipitation.

Epithermal Au deposits show a similar pattern to porphyry copper deposits (Duan et al., 2016a) and the gold-rich ores in these systems also have δ^{65}Cu values that cluster around 0‰ (Mathur et al., 2012b; Saunders et al., 2015). Interestingly, the pattern of lower values in the core of the deposits and higher values on the borders is identical to porphyry copper deposits (Wu et al., 2017; Zhao et al., 2022a). If porphyry copper deposits are related to epithermal systems at depth, the isotopic values at the cores of the systems should be higher than that found in porphyries, instead they are identical. To date, the only copper isotope values of a system where a porphyry copper deposit is clearly beneath an epithermal system are data from Yanacocha (Condon et al., 2012). At Yanacocha, the values of copper isotopes in chalcopyrite are lowest in the deepest parts of the porphyry and become higher to the base of the epithermal system. The two chalcopyrite and chalcocite values at the base of the epithermal system return δ^{65}Cu values ~0‰ and then values become higher in the outer portions of the epithermal system. These preliminary data suggest that the two hydrothermal systems are unique and not linked to the same hydrothermal event.

Volcanic-hosted massive sulfide (VHMS) deposits display the largest range of copper isotope variations within the higher temperature hydrothermal systems. Rouxel et al. (2004) presented values from an active VHMS site in the Mid-Atlantic and reported ranges of δ^{65}Cu values of up to 3‰, which was attributed to reworking and later stage mobilization of copper. Berkenbosch et al. (2015) found smaller variations in a modern VHMS mineralization in the Pacific and noted that the liquid-vapor partitioning could explain the fractionation because vapors emitted from the chimneys are metal-rich. Ancient VHMS systems do not display large copper isotope variations in the massive ores, with δ^{65}Cu values ranging around 1‰ and do not display simple, systematic spatial variations of copper isotopes (Ikehata et al., 2011; Mason et al., 2005).

Given the large array of potential fractionation mechanisms operating on copper during mineralization events across all ranges of temperatures discussed above, relating the copper isotope values of ores to those of source rocks is difficult. Figs. 42 and 43 are summary figures of all published copper isotope values in mantle rocks, crustal rocks, and ores. The violin plots show obvious overlapping signatures in all reservoirs for metal as well as the metals in ores. Pointing to specific mantle or crustal reservoirs as a source for copper in mineral deposits is challenging. For example, the mean values for PCDs, Mt. Isa and the Michigan copper ores are nearly identical and match that of the mantle average value. Continental basalts reported by Liu et al. (2015a, 2015b) nicely overlap the Mt. Isa and Michigan copper deposits. Given that copper in these deposits has been suggested to come from continental rift basalts, perhaps the overlap reflects a source signal. Again, the overlap and large range restrict convincing interpretations.

The mean values perhaps provide some insight into the 'starting' copper isotope signal in mineral deposits before fractionation mechanisms operate and create the unimodal distribution seen in most deposit types. The shapes (ranges) and means viewed in this manner provide interesting comparisons and ability to infer processes operating during deposition of copper minerals. For instance, deposits that form at variably low temperatures, like VHMS and sedimentary copper deposits, display the largest ranges. This demonstrates that the combination of multiple processes can produce the largest degrees of copper isotope fractionation. Interestingly, the lowest mean values in sedimentary copper deposits could reflect the reductive transport of copper from oxidized

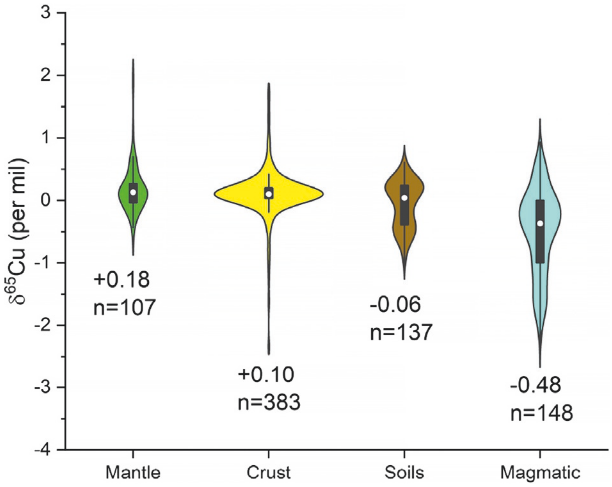

Fig. 42 Violin plot of copper isotope compositions of rocks. Data are from various sources.

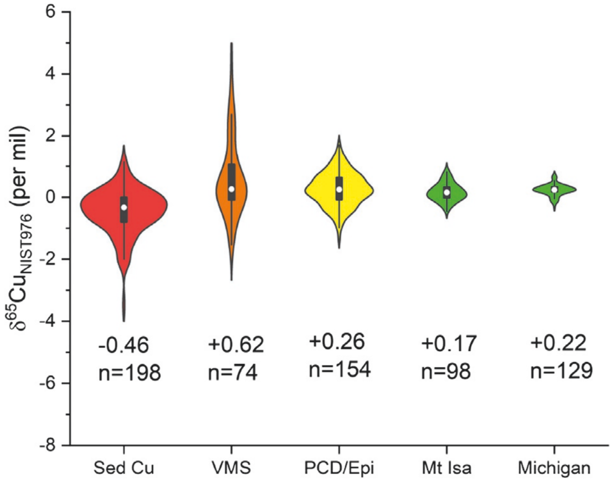

Fig. 43 Violin plot of copper isotope values in mineral deposits of the mineral chalcopyrite except for the Michigan Cu, where the copper isotope values come from native copper. Data are from various sources.

sedimentary rocks. The ranges for epithermal/porphyry copper deposits are larger than seen in places like the Michigan and Mt. Isa copper deposits, where moderate temperature fluids lacked a vapor phase and thus show smaller ranges of copper isotope fractionation. Therefore, summative comparison among the different deposits provides insights into different processes operating during mineralization, perhaps suggesting a more robust interpretation of the mean values.

Iron

Background and methods

Iron has four stable isotopes, ^{54}Fe, ^{56}Fe, ^{57}Fe and ^{58}Fe that comprise, respectively, 5.845%, 91.754%, 2.119% and 0.286% of natural occurring iron. There are an additional 24 known radioactive isotopes of iron, but none of these are useful for understanding mineral systems because their half-lives are too short, ranging from nanoseconds to years, or their concentration is too small for practical use. Iron isotope data are reported as δ^{56}Fe (‰) and/or δ^{57}Fe (‰) relative to the IRMM-14 standard and values of δ^{57}Fe‰ and δ^{56}Fe‰ are converted to each other by using the equation $\delta^{57}\text{Fe‰} \approx 1.5\delta^{56}\text{Fe‰}$ (Johnson et al., 2020). The use of iron isotopes has evolved rapidly over the past two decades because advances in multi-collector (MC) magnetic sector ICPMS have reduced molecular interferences or because the increased resolution of modern mass spectrometers allows the measurement of Fe isotopes on the ^{16}O^{40}Ar shoulder (mass 56 interfering with ^{56}Fe) (Anbar, 2004; Belshaw et al., 2000; Johnson et al., 2020). The abundances and calculated ^{56}Fe/^{54}Fe ratio and ^{57}Fe/^{54}Fe ratio of samples and IRMM-14 are now routinely measured with a repeatability of <100 ppm at 95% confidence level.

Iron isotope abundances are routinely measured in solution of bulk samples and in situ, using a femtosecond laser ablation system to vaporize a reduced mineral volume (spot) and measure the abundance of iron isotopes in the aerosol via MC-ICPMS. Details of the method can be found in Weyer et al. (2005).

Ore genesis processes and models

The use of iron isotopes has proven effective at distinguishing among multiple possible sources of iron in magmatic-hydrothermal and hydrothermal environments, despite the significantly smaller range of isotope fractionation for iron relative to copper (Fig. 44). The total range of δ^{56}Fe for all analyzed terrestrial materials is from ~−1.00 to +1.00‰ (Johnson et al., 2020 and references therein). There is a systematic fractionation of iron isotopes during the chemical evolution of silicate magmas, with δ^{56}Fe‰ values for whole rocks increasing from basalts to rhyolites. The δ^{56}Fe values of olivine, biotite, amphibole, and pyroxene in volcanic rocks are within the range defined for their igneous whole rocks and are relatively constant from basalt to rhyolite, whereas δ^{56}Fe values of magnetite are systematically heavier than their igneous host rock and silicate minerals. It has also been demonstrated that iron isotopes fractionate during degassing of a silicate melt reservoir (Heimann et al., 2008). The highest reported values of δ^{56}Fe are for intrusive and extrusive igneous rocks that preserve independent evidence for the loss of a magmatic-hydrothermal fluid, which is explained by preferentially scavenging of ^{54}Fe from the melt by the exsolved fluid.

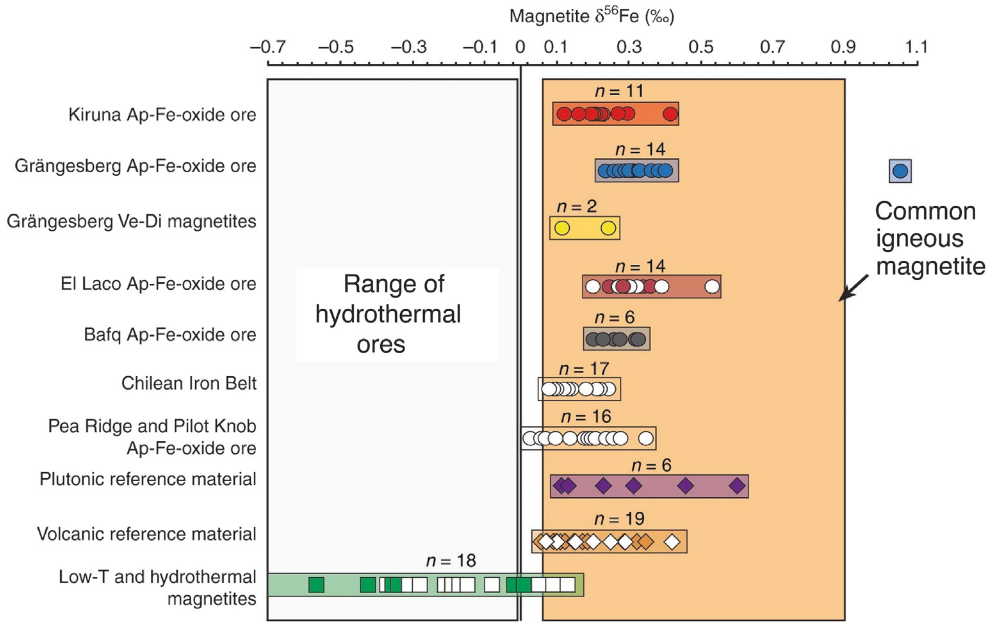

Fig. 44 Global range of iron isotope data for magnetite from several geological environments. Modified from Troll VR, Weis FA, Jonsson E, Andersson UB, Majidi SA, Högdahl K, Harris C, Millet MA, Chinnasamy SS, Kooijman E and Nilsson KP (2019) Global Fe–O isotope correlation reveals magmatic origin of Kiruna-type apatite-iron-oxide ores. *Nature Communications* **10**(1): 1712 all data reported relative to IRMM-14.

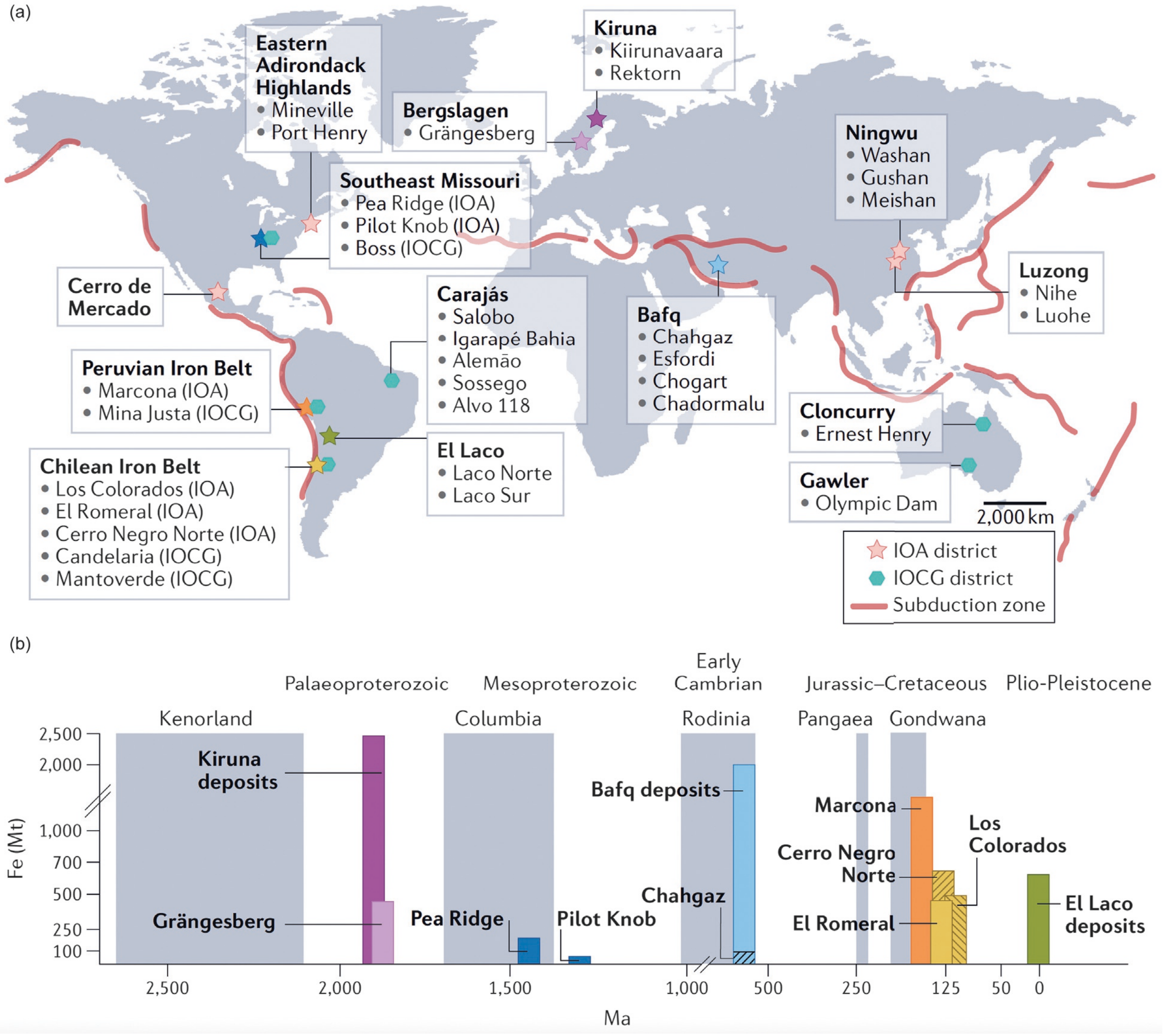

Fig. 45 Spatial and temporal distribution of important iron oxide-apatite mining districts. Iron oxide-apatite (IOA) deposits are distributed worldwide and have formed repeatedly over the history of the Earth, from the Paleoproterozoic to the Plio-Pleistocene. Panel (a): IOA deposits are typically associated with subduction-related extensional tectonic settings. IOA deposits (stars) can display spatial and temporal associations with iron oxide-copper-gold (IOCG) systems (hexagons), a feature most notably observed in the Andean province. Key deposits and districts are highlighted in bold. Panel (b): Temporal distribution of large (>100 Mt) IOA deposits, including their relation to the supercontinent cycle (gray blocks). Ma, million years ago. The bar colors match the symbols in (a). The formation of key IOA districts is broadly coincident with the break- up of the supercontinents Kenorland, Columbia, Rodinia and Gondwana. Reproduced with permission from Reich M, Simon AC, Barra F, Palma G, Hou T and Bilenker LD (2022) Formation of iron oxide–apatite deposits. *Nature Reviews Earth & Environment* 1–18.

A growing number of studies have used iron isotope abundances in bulk magnetite from iron oxide-apatite (IOA) deposits to fingerprint the source of iron. The first to report iron isotope data for magnetite from IOA deposits in the Cretaceous Chilean iron belt, the Plio-Pleistocene El Laco IOA deposit in Chile, and the Proterozoic Kiruna IOA district in Sweden (Fig. 45), were Bilenker et al. (2016, 2017) and Knipping et al. (2015a, 2015b). Subsequent studies reported iron isotope data for samples from IOA deposits globally (Fig. 45).

The data reveal that δ^{56}Fe values of magnetite in ore samples from all locations across nearly 3 billion years of Earth history (Fig. 45) fall within the range of about 0.00‰ to +1.00‰. These values are equal to the values for igneous rocks, and Knipping et al. (2015a, 2015b) and Bilenker et al. (2016) proposed that the overlapping range of iron isotope values for unequivocally igneous magnetite and magnetite in IOA deposits fingerprint a silicate magma as the source of iron in IOA deposits globally (Fig. 46). More recent studies of magnetite from El Laco (Childress et al., 2020a), the Chilean iron belt (Childress et al., 2020a; Rodriguez-Mustafa et al., 2022), the Bafq district, Iran (Troll et al., 2019), the Grängesberg Mining District, Central Sweden (Troll et al., 2019), the Missouri IOA district, United States (Childress et al., 2016; Tunnell et al., 2021), and the Kiruna Mining District, Northern Sweden

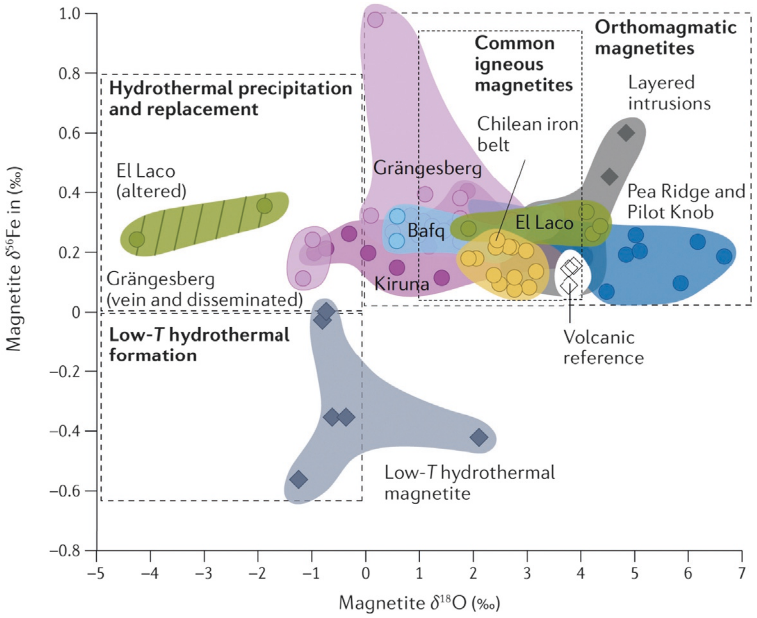

Fig. 46 The combination of Fe and O isotope data allow one to fingerprint the source reservoir(s) of the Fe ore. δ^{18}O versus δ^{56}Fe values of magnetite from deposits in Kiruna, Grängesberg, Bafq, Missouri, Chilean Iron Belt and El Laco are plotted and contoured as colored fields that correlate with those in Fig. 44. Nearly 90% of the Fe—O data isotope data lie within the reference boxes of common igneous (short- dashed line) and orthomagmatic magnetite, indicating a predominantly magmatic, high-temperature origin. Only 20% of the Fe—O data overlap with reference boxes of hydrothermal precipitation and replacement and low-temperature hydrothermal formation. δ^{18}O and δ^{56}Fe values are relative to SMOW and IRMM-14 standards, respectively. Figure from Reich M, Simon AC, Barra F, Palma G, Hou T and Bilenker LD (2022) Formation of iron oxide–apatite deposits. *Nature Reviews Earth & Environment* 1–18; Modified from Troll VR, Weis FA, Jonsson E, Andersson UB, Majidi SA, Högdahl K, Harris C, Millet MA, Chinnasamy SS, Kooijman E and Nilsson KP (2019) Global Fe–O isotope correlation reveals magmatic origin of Kiruna-type apatite-iron-oxide ores. Nature Communications 10(1): 1712.

(Troll et al., 2019) have corroborated this interpretation. The iron isotope data have been paired with oxygen isotope data in several studies, and together these data fingerprint a juvenile magma as the source of iron in IOA deposits globally (Reich et al., 2022; Simon et al., 2017) (Fig. 46). Combining iron and oxygen isotopes for magnetite from IOA deposits also reveals that post-mineralization processes change the oxygen but not the iron isotope compositions. This is seen most clearly in the oxygen isotope data of El Laco that document a systematic relationship between alteration of magnetite to hematite and goethite and decreasing oxygen isotope values (Fig. 47).

Knipping et al. (2019) used in situ femtosecond laser ablation multi-collector inductively coupled plasma mass spectrometry (LA-MC-ICP-MS) to measure intra-grain and grain-to-grain iron isotope abundances in magnetite to obtain spatial information within compositionally zoned magnetite grains. Bulk analysis for iron isotope abundances of magnetite grains yielded δ^{56}Fe values that range from 0.06‰ to 0.50‰, within the range reported for igneous and magmatic-hydrothermal reference materials. These authors reported that magnetite cores yield δ^{56}Fe values of 0.24‰, whereas magnetite rims yield δ^{56}Fe values of 0.15‰. This systematic core-to-rim decrease in δ^{56}Fe‰ values of magnetite is consistent with a two-stage growth process wherein magnetite cores grew in equilibrium with silicate liquid and magnetite rims grew in equilibrium with magmatic-hydrothermal fluid. The authors also report that the concentrations of Ti, Al, Ga, V, Mn, Zn in zoned magnetite grains systematically decrease from core to rim, which is consistent with igneous nucleation and growth followed by magmatic-hydrothermal growth around the igneous core.

Several studies have reported iron isotope data for magnetite from iron oxide-copper-gold (IOCG) deposits. These data indicate that the iron isotope composition of IOCG deposits covers approximately the same range as that for IOA deposits (Fig. 45). For example, δ^{56}Fe values of magnetite from the Mantoverde and Candelaria IOCG deposits in Chile overlap values for IOA deposits in the same district (Childress et al., 2020b; Rodriguez-Mustafa et al., 2022).

There are only a few studies that report iron isotope data for porphyry systems. Graham et al. (2004) reported δ^{57}Fe values for chalcopyrite and pyrite from the Grasberg porphyry gold deposit that range from −3.02‰ to +0.19‰ and −0.26‰ to +1.62‰, respectively. These authors emphasize that, despite the overlap in the total range of δ^{57}Fe values, there are only a few values for chalcopyrite and pyrite that are statistically similar. The fact that the majority of the δ^{57}Fe values for chalcopyrite and pyrite do not overlap indicates either isotopic fractionation between the two minerals or precipitation from different fluids. The data demonstrate that pyrite preferentially incorporates heavier iron isotopes relative to chalcopyrite and the authors suggest that iron isotope fractionation between these two sulfides may be temperature-dependent.

Wawryk and Foden (2017) reported iron isotope data for whole rocks and mineral separates from the granitic source rocks of the Renison porphyry tin deposit in Tasmania. The δ^{57}Fe values for whole rock range from +0.27‰ to +0.43‰. The δ^{57}Fe values for arsenopyrite, chalcopyrite, pyrite, pyrrhotite, magnetite and siderite range from, respectively, +0.85‰ to +1.11‰, +0.28‰ to

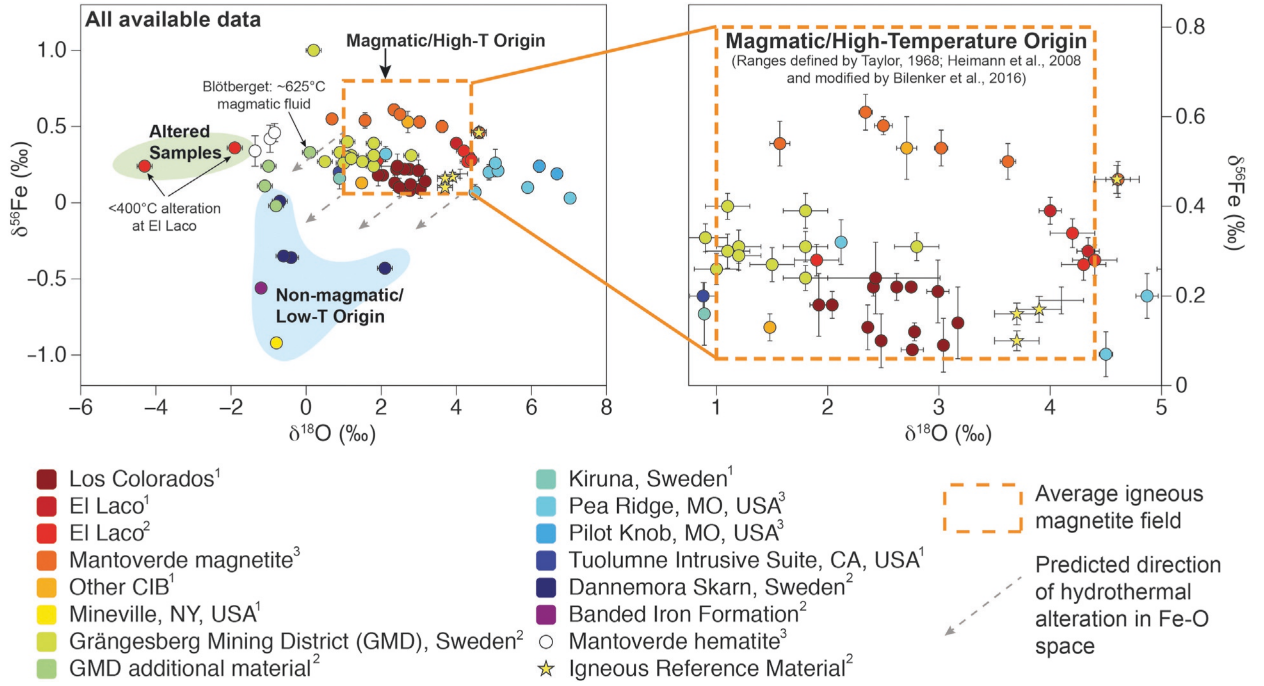

Fig. 47 Fe and O Isotopic data for magnetite samples in δ^{56}Fe vs. δ^{18}O space. The dashed orange box denotes the range for magmatic (igneous) Fe and O isotope values of magnetite. Stars denote δ^{56}Fe vs. δ^{18}O values for igneous magnetite. Error bars are 2σ. Data sources are indicated by superscripts as follows: 1 = Bilenker et al. (2016), 2 = Weis (2013), 3 = Childress et al. (2016), 4 = Childress et al. (2020a). Samples labeled Grängesberg mining district (GMD) are magnetite from the massive magnetite-apatite orebody, whereas samples labeled GMD additional material are magnetite from the metavolcanic host rock. See Bilenker et al. (2016) for details. Modified from *Simon AC, Knipping J, Reich M, Barra F, Deditius AP, Bilenker L and Childress T (2018) Kiruna-type iron oxide-apatite (IOA) and iron oxide copper-gold (IOCG) deposits form by a combination of igneous and magmatic-hydrothermal processes: Evidence from the Chilean Iron Belt. Society of Economic Geology Special Publication No. 21, 89–114.*

+1.32‰, +0.89‰ to +1.59‰, +1.0‰ to +1.01‰, −1.00‰ to 0.00‰ and 0.07‰ to +0.05‰. These authors compared calculated mineral-mineral fractionation factors from their data with theoretical predictions of equilibrium fractionation and reported that the temperatures obtained from the natural mineral-mineral pairs agree with published temperatures determined from fluid inclusion microthermometry. However, the mineral-mineral temperatures are not consistent with the expected decreasing temperature from the central hotter part of the system towards the periphery. Hence, the authors conclude that temperatures determined using mineral-mineral iron isotope fractionation factors should be used with caution.

Iron isotope data for magnetite, pyrite, and chalcopyrite as well as granodiorite host rocks in the Bolong and Duobuza ore bodies of the giant Duolong porphyry Cu—Au deposit, Tibet, record changes in isotopic composition for different alteration assemblages (Li et al., 2018). These data reveal that magnetite is isotopically enriched compared with pyrite, which is explained by fractionation during fluid cooling and precipitation of magnetite followed by chalcopyrite. The calculated equilibrium δ^{57}Fe values for fluids from which magnetite and chalcopyrite precipitated are systematically lighter than the mineral phases and the fluids are isotopically lighter than the granodiorite hypothesized to be the fluid source. Interestingly, the results reveal that chalcopyrite in oxidized systems is isotopically lighter than in reduced systems. This indicates the potential to use the iron isotopic composition of chalcopyrite as a redox indicator.

Wawryk and Foden (2017) reported iron isotopic data for the Batu Hijau porphyry-Cu-Au deposit (Indonesia) that further document a heavier isotope signature for magnetite relative to chalcopyrite. These authors report that iron isotopic signatures increase with increasing silica content of the igneous units. Magnetite from the ore body is isotopically heavier than chalcopyrite, which is isotopically lighter than chalcopyrite from reduced porphyries. The authors suggest that crystallization of pyrrhotite, because of its preference for isotopically light iron and the effects of redox conditions on iron, influences the signature of chalcopyrite.

Wei et al. (2020) reported that the iron isotopic composition of igneous magnetite is significantly heavier than coeval ilmenite in an anorthosite-hosted Fe—Ti oxide ore body. Iron isotopic fractionation between magnetite and ilmenite likely occurred at subsolidus conditions during cooling and oxidation of ulvöspinel. These authors also reported that igneous pyrite is isotopically heavier than hydrothermal pyrite, indicating that the iron isotopic composition of a magmatic-hydrothermal fluid is lighter than its source melt. This observation appears to be systematic across magmatic-hydrothermal deposit types.

Wang et al. (2011) reported iron isotope compositions of mineral separates and bulk samples from the Xinqiao Cu—Fe—Au skarn deposit of Anhui, China. The δ^{57}Fe values for quartz-monzodiorite whole rocks range from −0.15‰ to +0.29‰. The δ^{57}Fe values for magnetite, granular pyrite, colloform pyrite and chalcopyrite range from, respectively, −0.54‰ to +0.20‰, −1.05‰ to +0.73‰, −1.22‰ to +0.15‰, and −0.98‰ to −0.72‰. There are spatial and temporal relationships among the δ^{57}Fe values of the mineral phases and the authors propose that these variations may result from incorporation of Fe from host rocks during hydrothermal metasomatic processes, or Fe-isotope fractionation during fluid evolution. The δ^{57}Fe value of the host country rock is 0.41‰, which eliminates the possibility that contamination by the country rock can explain the higher δ^{57}Fe values for pyrite. The authors conclude that, based on the work of Heimann et al. (2008), fractionation of iron isotopes during fluid evolution is the most plausible explanation for the inter-mineral ranges of δ^{57}Fe values among magnetite, granular pyrite, colloform pyrite and chalcopyrite.

There is a dearth of iron isotopic data for sedimentary exhalative (SEDEX) Zn—Pb deposits. Gao et al. (2018) report that the δ^{56}Fe values of sphalerite and pyrrhotite from the brecciated Zn—Pb ores of the main ore body in the giant Dongshengmiao deposit, China, change systematically within the main ore body, which they explain by Rayleigh fractionation during hydrothermal fluid flow, with lighter Zn and Fe isotopes preferentially incorporated into the earliest sulfides. The δ^{56}Fe values of sphalerite exhibit more variability than δ^{66}Zn values of sphalerite, which is attributed to coeval precipitation of pyrrhotite that preferentially scavenges light iron from the hydrothermal fluid. The lead isotopic data for this system are consistent with a single hydrothermal fluid. There is a positive spatial correlation between the iron isotopic signature of pyrrhotite and sphalerite and copper mineralization that indicates the potential to use the iron isotopic data as a vectoring tool for copper.

Iron isotope data from VHMS deposits have been used to decipher their formation. Otake et al. (2021) report that sulfides from the ferruginous sedimentary rocks of the Kuroko VHMS deposit have δ^{56}Fe values that vary by almost 4‰ from about −2.00‰ to +2.00‰. The δ^{56}Fe values are significantly fractionated from that expected for iron dissolved in high-temperature, seafloor hydrothermal fluids, which range from −0.70‰ to −0.10‰, and iron in igneous and clastic sedimentary rocks, which range from −0.10‰ to +0.40‰. The data indicate that partial oxidation of ferrous iron in the hydrothermal fluid played a key role in the precipitation of iron hydroxides and oxides. The heavy isotopic values of iron hydroxides and oxides likely reflect coeval precipitation of sulfides and deposition of ferruginous sedimentary rocks. The Cu-rich ores are isotopically heavier than Zn-rich black ores, which have the lightest iron isotope signature in the deposit. These data are consistent with mixing of magmatic-hydrothermal fluids and seawater, which caused rapid precipitation of sulfide minerals to form the black ores. On the contrary, the yellow ores likely formed by slow growth of pyrite from high-temperature hydrothermal fluids that replaced the black ores.

Iron isotopes have also been used to understand processes in unconformity related uranium deposits. Potter et al. (2015) reported iron isotopic compositions of whole rocks and clay separates from the Bong uranium deposit, Thelon Basin Canada. The highest δ^{57}Fe values in the ore body correlate spatially with hematite-rich alteration and argue against formation of hematite during paleoweathering. These data indicate that significant fractionation occurred during oxidation of Fe^{2+} to Fe^{3+} and simultaneous reduction of U^{6+} to U^{4+}, which resulted in hematite and uraninite precipitation, respectively.

A few studies have used iron isotopes to fingerprint the source of iron in metamorphic environments. Whitehouse et al. (2015) used iron isotopes to test the hypothesis that iron-rich rocks in quartz-amphibole-pyroxene gneiss on the island of Akilia, southern West Greenland, might have inherited their iron from a banded iron formation. These rocks have been proposed to be either mafic-ultramafic igneous rocks that were subjected to extreme ductile deformation and high-grade metamorphic metasomatism, which added significant silica (i.e., quartz), or to represent an original chemical sedimentary origin. These authors report bulk-rock δ^{56}Fe signatures as high as +1.00‰, which are similar to early Archean banded iron formations from Isua. The elevated iron isotope values cannot be explained as inheritance from the mafic igneous protoliths, but rather suggest a chemical sedimentary origin for the iron isotope fractionation.

Zinc

Background and methods

Zinc has five isotopes (64, 66, 67, 68, 70) and, due to its high ionization potential, was not initially explored for isotopic fractionation until the advent of MC-ICPMS in the 1990s. Chemical purification through chromatography has been employed on ores and rocks. The separation technique employed for copper can also yield zinc at a later aliquot during the column chemistry procedure (Marechal et al., 1999). Other techniques have been employed using similar resins and slightly different acid protocols to confidently separate Zn (Bermin et al., 2006; Chapman et al., 2004; Mason et al., 2004; Moynier et al., 2006; Peel et al., 2008; Petit et al., 2008; Ponzevera et al., 2006; Sossi et al., 2015).

Zn isotope values are traditionally reported as δ^{66}Zn (using $^{66}Zn/^{64}Zn$) in the per mil (‰) format. Mass dependence has been reported for δ^{67}Zn and/or δ^{68}Zn for most materials. Mass bias is corrected using the NIST-976 copper isotope standard coupled with standard-sample-standard bracketing. Errors for these analyzes are slightly lower than for copper with typical 2σ ranges from ±0.03‰ to ±0.05‰.

Ore genesis processes and models

Zinc isotope fractionation is significantly smaller than seen in copper (Fig. 48) and most likely relates to the fact that there are not significant redox shifts with Zn in natural ore forming environments, Zn having only one oxidation state. As Borrok et al. (2008) demonstrated, the dissolution of sphalerite does not induce significant Zn isotopic shift at about +0.2‰ enrichment in the solution.

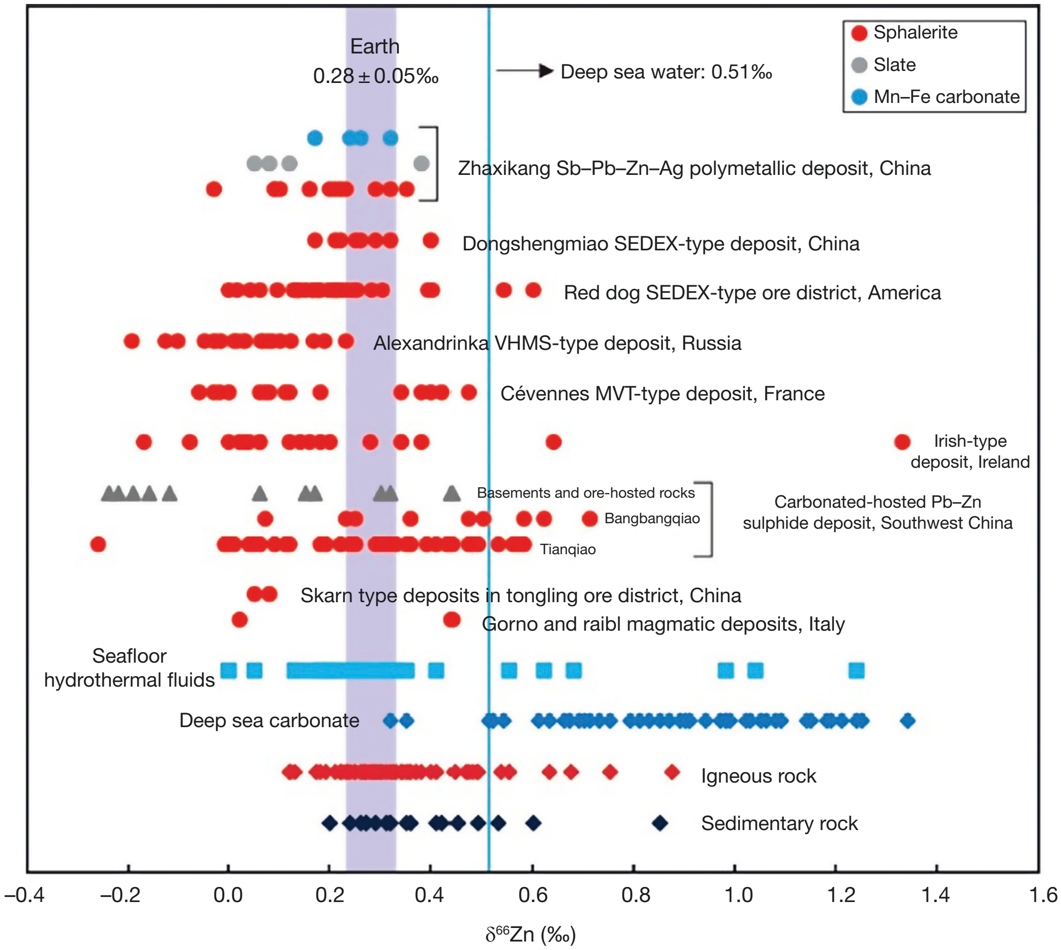

Fig. 48 Zn isotope variations in rocks and ores. Note that there are smaller ranges than seen for copper. All data are reported relative the Lyon Zn standard.

Therefore, no water geochemistry involving Zn and mineral exploration currently exists in the literature. Most studies concerning Zn ores show that some patterning could be seen in sphalerites and relate the variations to mineral depositional processes.

Several papers with relatively small datasets demonstrate that the largest Zn isotope fractionation on Earth occurs in mineral deposits. The largest range of Zn isotope fractionation occurs on the seafloor with δ^{66}Zn values spanning over 1‰ (John et al., 2008). The variation has been tied to lighter Zn precipitation in the first sphalerites forming from the cooling vent fluids. Yang et al. (2022) further corroborated this evidence by looking at sphalerite from an ancient seafloor continental VHMS deposit. The combination of S and Cd isotopes allowed them to infer the potential for biological activity in the fractionation of Zn isotopes. Mason et al. (2005) also reported fractionated Zn signals in hydrothermal seafloor vent mineralogy, with higher Zn isotope compositions found on the rims of chimneys.

Multiple Zn isotope studies have focused on sedimentary exhalative, MVT and Irish Midland deposits. Genetic models for all these deposits share some similarities, like the association with carbonate rocks, and some distinct differences in mineralogy and fluid compositions (Hitzman et al., 2010; Leach et al., 2005). From a Zn isotope perspective, the Irish Midland deposits possess the largest Zn isotope variation (Wilkinson et al., 2005). Highly fractionated Zn was also reported at the Broken Hill deposits in Australia (Spry et al., 2022). An integrated isotopic approach combining S and Cd with the Zn isotope composition aided interpreting the Broken Hill deposits to be related to syngenetic deposition of sulfides with a clear biological signature preserved in the ores. The importance of the interpretation is that the combined isotopic approach is still able to reveal these processes even in ores that experienced high degrees of post-mineral metamorphism.

Smaller ranges of Zn isotope fractionation were reported in several classic sedimentary exhalative deposits. Kelley et al. (2009) reported a δ^{66}Zn range of about 0.5‰ for ores at the Red Dog deposit in Alaska. They observed a pattern of changing Zn isotope composition in space and related the variations to fluid pathways. Post-mineral deposition processes could have caused such pattern, as argued for the metamorphosed ores at Balmat (Matt et al., 2020). The ore lenses at Balmat show a distinctly higher mean value of sphalerite down plunge of the major syncline (Fig. 49). Matt et al. (2020) argued that the slight Zn isotope variation of the values could reflect slight melt mobilization from the core of the structure to the limb. Zhou et al. (2014) measured Zn isotope compositions in sedimentary exhalative deposits in China and the variable Zn isotope values among the related mineral deposits

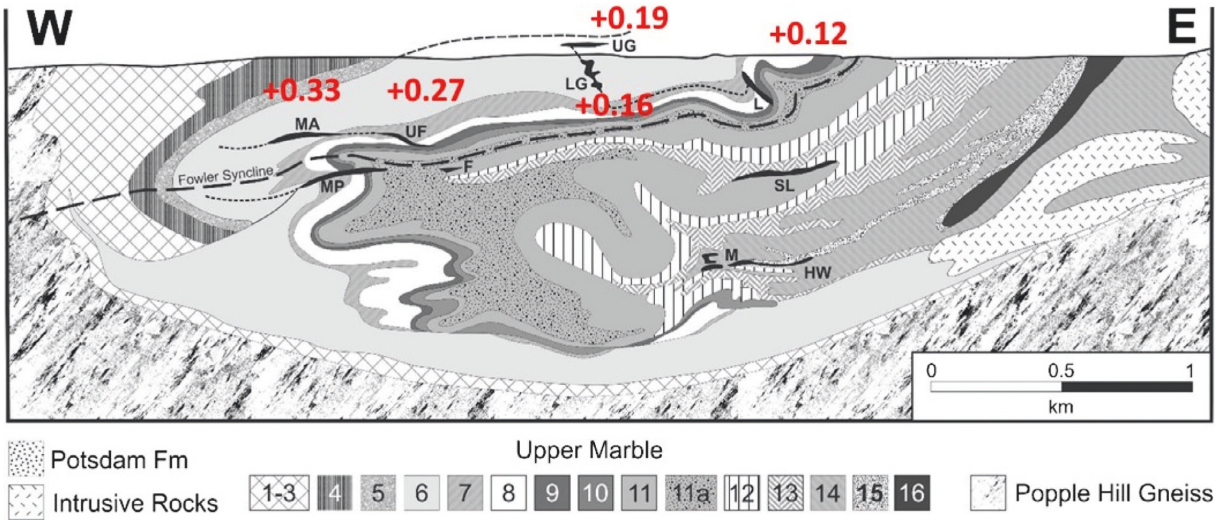

Fig. 49 Changes in the mean values of Zn isotope compositions (labeled in red) of the Balmat ore body (thicker black lines in cross section) in New York, United States.

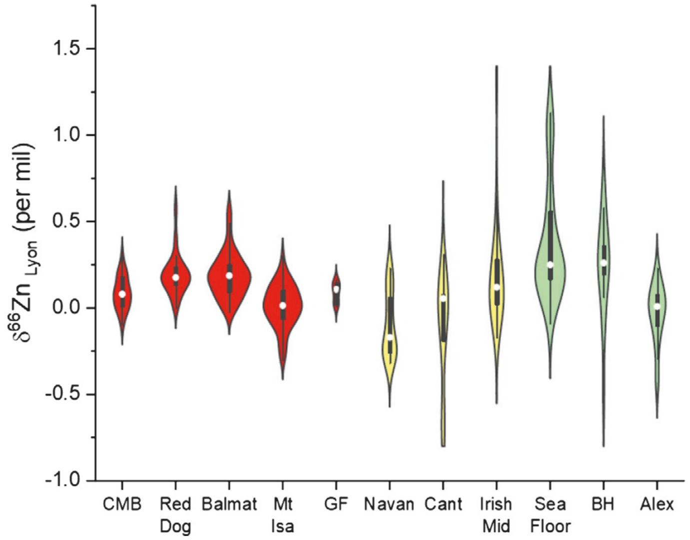

Fig. 50 Violin plot of Zn isotope values from different mineral deposit types. Data from various sources.

were argued to be caused by different source rocks as well as slight changes in the mineralization fluids. Wang et al. (2021a, 2021b) and Duan et al. (2016b) used Zn isotope values in the Zhaxikang deposit, Tibet, to demonstrate that Zn precipitated through sedimentary-exhalative processes and that an epithermal system overprinted the deposit.

The violin plot of Fig. 50 shows the variations among the deposits discussed above. The mean values do not show much consistency across deposit types. However, the ranges show that different processes must be operating during the formation of these Zn deposits. For instance, the traditional sedimentary exhalative deposits like Balmat, Red Dog, and Mt. Isa clearly have a distinctly smaller range in Zn isotope composition in comparison to all the other sphalerite deposits reported. These differences in range of Zn isotope compositions allow for distinction of mineral deposit process which could easily be related to pH and different Zn chloride or Zn carbonate speciation during mineral precipitation, as pointed to by Ducher et al. (2018) and Fujii et al. (2011).

Only one contribution has really explored how Zn behaves in the supergene low temperature environment. Mondillo et al. (2018) analyzed sphalerite and associated Zn oxides from multiple places across the globe (Fig. 51). They found that willemite has the greatest compositional variability, and that significant fractionations in positive and negative directions are recorded relative to the precursor phase. They pointed to several bonding and precipitation mechanisms which would lead to the recorded Zn isotope compositions. Zn oxide data were also presented in Matt et al. (2022). These authors observed a systematic trend in the Zn oxide phases where δ^{66}Zn decreased in value according to the following order: franklinite < williminite < zincite. This trend matched the theoretical predicted fractionation of Zn during precipitation of Zn oxides from moderate temperature solutions (Ducher et al., 2018). The pattern is consistent with a sedimentary exhalative origin for these deposits.

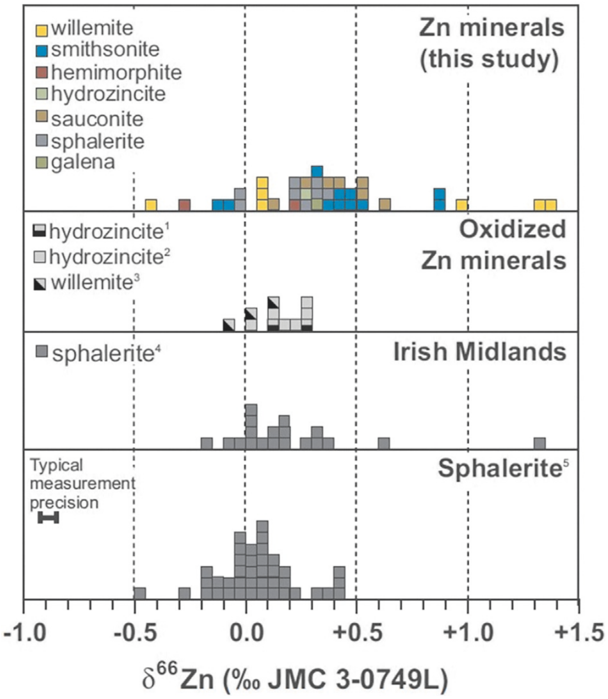

Fig. 51 Zn isotope variations in Zn ores from Mondillo et al. (2018).

Conclusions and outlook

Isotopes have been used since almost a century to investigate the formation processes of mineral deposits. For application purposes in mineral deposit studies we can distinguish three types of isotopes: (i) stable non-radiogenic isotopes; (ii) stable radiogenic isotopes, and (iii) unstable (radioactive) isotopes. Stable non-radiogenic isotopes of the same element (both with light, e.g., H, C, O and heavy atomic weights, e.g., Fe, Cu, Zn) fractionate in measurable amounts during chemical (e.g., redox reactions), physical (e.g., temperature), and biological (e.g., biogenic activity) reactions. Therefore, they are most suited to track processes that are associated with changes in these parameters during the formation of mineral deposits. Although in its "infancy," the application of "unconventional" metal stable isotopes to the study of mineral deposits is quickly growing allowing us to investigate processes previously not addressable with "traditional" isotopes as highlighted by the examples discussed above. A more extensive application to mineral deposit investigations of isotopes of elements displaying MIF, such as Hg and S, as well as of clumped isotopes, both of which are already used to investigate other geological processes, could be beneficial to deepen our understanding on some aspects of the formation of ore deposits.

Stable radiogenic isotope variations in the Earth depend on (i) the chemical partitioning of parent and daughter elements (e.g., Rb—Sr, U—Pb, Sm—Nd), which can occur both during deep Earth processes in the mantle and crust (e.g., partial melting, magma fractionation, metamorphism) as well as during surface processes (e.g., weathering), and (ii) on the time in the past when these processes occurred. As such, stable radiogenic isotopes are powerful tracers of metal (and other element) reservoirs, of their involvement during mineralization processes, and of their reciprocal interactions. Stable radiogenic isotopes are mostly used as tracers of metal and fluid sources in mineralization and of fluid-rock interactions helping us to reconstruct the hydrothermal plumbing system of the mineralization.

The combined use of radioactive parent and radiogenic daughter isotopes allows us, using simple isotope decay equations, to determine the time in the past when a mineral became a closed system with respect to the thermally-induced diffusion of parent and daughter isotopes. For some isotope systems and minerals this time coincides with the mineral formation and therefore this method allows us to determine the time of formation of a mineral deposit. In turn, this allows us to link mineral deposit formation to major geological processes occurred throughout Earth's history.

Continuous methodological, instrumental and analytical improvements have allowed us to reduce the size of the material to analyze, so that currently we can carry out all types of isotopic studies discussed above on samples ranging from bulk hand samples, to mineral separates, to single minerals, to specific portions of single minerals and even on single fluid inclusions hosted by minerals. The possibility to carry out isotopic studies at all these scales combined with increased precision (and accuracy) in the data gives us a powerful tool to investigate not only processes of ore formation but also their timescales, i.e., allows us to calculate rates of ore-forming processes. Quantifying the rates of geological processes, including ore-forming ones, is a new frontier if we want to understand how fast the fluid, metals and energy needed to form a mineral deposit are delivered to the system: this has impacts on our understanding of the large-scale geological processes that control the formation of mineral deposits.

The future of isotopic studies applied to mineral deposits, and not only, will be to push the limits of precision and spatial resolution with the aim to obtain almost a time-lapse reconstruction of a mineral deposit formation. This can only be achieved through the combined information provided by different isotope systems and their foreseeable future improvements.

Acknowledgments

We are grateful to Section Editor Matt Kohn for the invitation to contribute the present Chapter to this book. We also acknowledge the careful reviews of Matt Kohn, Georges Beaudoin and Yun Zhao, which contributed to improve significantly a previous version of the manuscript.

References

Ahmed AH, Hanghøj K, Kelemen PB, Hart SR, and Arai S (2006) Osmium isotope systematics of the Proterozoic and Phanerozoic ophiolitic chromitites: In situ ion probe analysis of primary Os-rich PGM. *Earth and Planetary Science Letters* 245(3–4): 777–791.

Anbar AD (2004) Iron stable isotopes; beyond biosignatures. *Earth and Planetary Science Letters* 217: 223–236.

Anglin CD, Jonasson IR, and Franklin JM (1996) Sm-Nd dating of scheelite and tourmaline: Implications for the genesis of Archean gold deposits, Val d'Or, Canada. *Economic Geology* 91: 1372–1382.

Archer C and Vance D (2004) Mass discrimination correction in multiple-collector plasma source mass spectrometry: An example using Cu and Zn isotopes. *Journal of Analytical Atomic Spectrometry* 19: 656–665.

Archer C, Andersen MB, Cloquet C, Conway TM, Dong S, Ellwood M, Moore R, Nelson J, Rehkamper M, Rouxel O, Samanta M, Shin K-C, Sohrin Y, Takano S, and Wasylenki L (2017) Inter-calibration of a proposed new primary reference standard AA-ETH Zn for zinc isotopic analysis. *Journal of Analytical Atomic Spectrometry* 32: 415–419.

Arehart GB, Chakurian AM, Tretbar DR, Christensen JR, McInnes BA, and Donelick RA (2003) Evaluation of radioisotope dating of carlin-type deposits in the great basin, Western North America, and implications for deposit genesis. *Economic Geology* 98: 235–248.

Asadi S, Mathur R, Moore F, and Zarasvandi A (2015) Copper isotope fractionation in the Meiduk porphyry copper deposit, Northwest of Kerman Cenozoic magmatic arc, Iran. *Terra Nova* 27: 36–41.

Asael D, Matthews A, Bar-Matthews M, and Halicz L (2007) Copper isotope fractionation in sedimentary copper mineralization (Timna Valley, Israel). *Chemical Geology* 243: 238–254.

Asael D, Matthews A, Oszczepalski S, Bar-Matthews M, and Halicz L (2009) Fluid speciation controls of low temperature copper isotope fractionation applied to the Kupferschiefer and Timna ore deposits. *Chemical Geology* 262: 147–158.

Asael D, Matthews A, Bar-Matthews M, Harlavan Y, and Segal I (2012) Tracking redox controls and sources of sedimentary mineralization using copper and lead isotopes. *Chemical Geology* 310–311: 23–35.

Ault KM and Williams-Jones AE (2004) Sulfur and lead isotope study of the El Mochito Zn-Pb-Ag deposit. *Economic Geology* 99: 1223–1231.

Babcsányi I, Chabaux F, Granet M, Meite F, Payraudeau S, Duplay J, and Imfeld G (2016) Copper in soil fractions and runoff in a vineyard catchment: Insights from copper stable isotopes. *Science of the Total Environment* 557–558: 154–162.

Balistrieri LS, Borrok DM, Wanty RB, and Ridley WI (2008) Fractionation of Cu and Zn isotopes during adsorption onto amorphous Fe(III) oxyhydroxide: Experimental mixing of acid rock drainage and ambient river water. *Geochimica et Cosmochimica Acta* 72: 311–328.

Barley ME and Groves DI (1992) Supercontinent cycles and the distribution of metals through time. *Geology* 20: 291–294.

Barrie TC, Amelin Y, and Pascual E (2002) U–Pb geochronology of VMS mineralization in the Iberian Pyrite Belt. *Mineralium Deposita* 37: 684–703.

Bau M, Romer RL, Lüders V, and Dulski P (2003) Tracing element sources of hydrothermal mineral deposits: REE and Y distribution and Sr-Nd-Pb isotopes in fluorite from MVT deposits in the Pennine Orefield, England. *Mineralium Deposita* 38(8): 992–1008.

Bekker A, Slack JF, Planavsky N, Krapez B, Hofmann A, Konhauser KO, and Rouxel OJ (2010) Iron formation: The sedimentary product of a complex interplay among Mantle, Tectonic, Oceanic, and Biospheric Processes. *Economic Geology* 105: 467–508.

Belshaw N, Zhu X, Guo Y, and O'Nions R (2000) High precision measurement of iron isotopes by plasma source mass spectrometry. *International Journal of Mass Spectrometry* 197: 191–195.

Bergquist BA and Blum JD (2007) Mass-dependent and-independent fractionation of Hg isotopes by photoreduction in aquatic systems. *Science* 318(5849): 417–420.

Berkenbosch HA, de Ronde CEJ, Paul BT, and Gemmell JB (2015) Characteristics of Cu isotopes from chalcopyrite-rich black smoker chimneys at Brothers volcano, Kermadec arc, and Niuatahi volcano, Lau basin. *Mineralium Deposita* 50: 811–824.

Bermin J, Vance D, Archer C, and Statham PJ (2006) The determination of the isotopic composition of Cu and Zn in seawater. *Chemical Geology* 226: 280–297.

Bigalke M, Weyer S, and Wilcke W (2009) Stable copper isotopes: A novel tool to trace copper behavior in hydromorphic soils. *Soil Science Society of America Journal* 74: 60–73.

Bigalke M, Weyer S, Kobza J, and Wilcke W (2010) Stable Cu and Zn isotope ratios as tracers of sources and transport of Cu and Zn in contaminated soil. *Geochimica et Cosmochimica Acta* 74: 6801–6813.

Bilenker LD, Simon AC, Reich M, Lundstrom CC, Gajos N, Bindeman I, Barra F, and Munizaga R (2016) Fe–O stable isotope pairs elucidate a high-temperature origin of Chilean iron oxide-apatite deposits. *Geochimica et Cosmochimica Acta* 177: 94–104.

Bilenker LD, VanTongeren JA, Lundstrom CC, and Simon AC (2017) Iron isotopic evolution during fractional crystallization of the uppermost Bushveld Complex layered mafic intrusion. *Geochemistry, Geophysics, Geosystems* 18(3): 956–972.

Blotevogel S, Oliva P, Sobanska S, Viers J, Vezin H, Audry S, Prunier J, Darrozes J, Orgogozo L, Courjault-Radé P, and Schreck E (2018) The fate of Cu pesticides in vineyard soils: A case study using δ^{65}Cu isotope ratios and EPR analysis. *Chemical Geology* 477: 35–46.

Borrok DM, Wanty RB, Ridley WI, Wolf R, Lamothe PJ, and Adams M (2007) Separation of copper, iron, and zinc from complex aqueous solutions for isotopic measurement. *Chemical Geology* 242(3-4): 400–414.

Borrok DM, Nimick DA, Wanty RB, and Ridley WI (2008) Isotopic variations of dissolved copper and zinc in stream waters affected by historical mining. *Geochimica et Cosmochimica Acta* 72(2): 329–344.

Boujelben N, Bouzid J, and Elouear Z (2009) Adsorption of nickel and copper onto natural iron oxide-coated sand from aqueous solutions: Study in single and binary systems. *Journal of Hazardous Materials* 163(1): 376–382.

Bouse RM (1995) *Lead Isotopic Compositions of Ore Deposition and Their Host Rocks in Arizona: Implications for the Crustal Inheritance of Metals*. The University of Arizona.

Bowman JR, Parry WT, Kropp WP, and Kruer SA (1987) Chemical and isotopic evolution of hydrothermal solutions at Bingham, Utah. *Economic Geology* 82: 395–428.

Braxton DP and Mathur R (2011) Exploration applications of copper isotopes in the supergene environment: A case study of the Bayugo Porphyry Copper-Gold deposit, Southern Philippines. *Economic Geology* 106(8): 1447–1463.

Braxton DP and Mathur R (2014) Copper isotopic vectors to supergene enrichment: Leaches cap isotopic footprint of the Quellaveco porphyry copper deposit, southern Peru. In: *SEG Conference Proceedings, SEG 2014, Building Exploration Capability for the 21st Century*.

Braxton DP, Cooke DR, Ignacio AM, Rye RO, and Waters PJ (2009) Ultra-deep oxidation and exotic copper formation at the late Pliocene Boyongan and Bayugo porphyry copper-gold deposits, Surigao, Philippines: Geology, mineralogy, paleoaltimetry, and their implications for geologic, physiographic, and tectonic controls. *Economic Geology* 104(3): 333–349.

Carr GR, Dean JA, Suppel DW, and Heithersay PS (1995) Precise lead isotope fingerprinting of hydrothermal activity associated with Ordovician to carboniferous metallogenetic events in the Lachlan fold belt of New South Wales. *Economic Geology* 90: 1467–1505.

Carter LC, Tapster SR, Williamson BJ, Buret Y, Selby D, Rollinson GK, Millar I, and Parvaz DB (2022) A rapid change in magma plumbing taps porphyry copper deposit-forming magmas. *Scientific Reports* 12(1): 1–20.

Champion DC and Huston DL (2016) Radiogenic isotopes, ore deposits and metallogenetic terranes: Novel approaches based on regional isotopic maps and the mineral systems concept. *Ore Geology Reviews* 76: 229–256.

Chapman JB, Mason TFD, Weiss DJ, Coles BJ, Wilkinson JJ, et al. (2004) An adapted column chemistry procedure for separation of Fe, Cu and Zn from geological matrices, and natural Zn isotopic variations in geological standard reference materials BCR-027, BCR-030 and NOD-P-1. *Abstracts with Programs - Geological Society of America* 36(5): 448.

Chapman JB, Mason TFD, Weiss DJ, Coles BJ, and Wilkinson JJ (2006) Chemical separation and isotopic variations of Cu and Zn from five geological reference materials. *Geostandards and Geoanalytical Research* 30(1): 5–16.

Chelle-Michou C, Chiaradia M, Ovtcharova M, Ulianov A, and Wotzlaw JF (2014) Zircon petrochronology reveals the temporal link between porphyry systems and the magmatic evolution of their hidden plutonic roots (the Eocene Coroccohuayco deposit, Peru). *Lithos* 198: 129–140.

Chelle-Michou C, Rottier B, Caricchi L, and Simpson G (2017) Tempo of magma degassing and the genesis of porphyry copper deposits. *Scientific Reports* 7: 40566.

Cherniak DJ and Watson EB (2001) Pb diffusion in zircon. *Chemical Geology* 172: 5–24.

Chiaradia M (2009) Adakite-like magmas from fractional crystallization and melting-assimilation of mafic lower crust (Eocene Macuchi arc, Western Cordillera, Ecuador). *Chemical Geology* 265(3-4): 468–487.

Chiaradia M (2020) Gold endowments of porphyry deposits controlled by precipitation efficiency. *Nature Communications* 11: 248. https://doi.org/10.1038/s41467-019-14113-1.

Chiaradia M (2022) Distinct magma evolution processes control the formation of porphyry Cu–Au deposits in thin and thick arcs. *Earth and Planetary Science Letters* 599: 117864.

Chiaradia M (2023) Radiometric dating applied to ore deposits: Theory and methods. In: Huston DL and Gutzmer J (eds.) *Isotopes in Economic Geology, Metallogensis and Exploration*. Berlin: Springer (in press).

Chiaradia M and Caricchi L (2022) Supergiant porphyry copper deposits are failed large eruptions. *Communications Earth & Environment* 3: 107.

Chiaradia M and Fontboté L (2001) Radiogenic lead signatures in Au-rich volcanic-hosted massive sulfide ores and associated volcanic rocks of the Early Tertiary Macuchi island arc (Western Cordillera of Ecuador). *Economic Geology* 96(6): 1361–1378.

Chiaradia M and Fontboté L (2002) Lead isotope systematics of Late Cretaceous–Tertiary Andean arc magmas and associated ores between 8N and 40S: Evidence for latitudinal mantle heterogeneity beneath the Andes. *Terra Nova* 14(5): 337–342.

Chiaradia M and Fontboté L (2003) Separate lead isotope analyses of leachate and residue rock fractions: Implications for metal source tracing in ore deposit studies. *Mineralium Deposita* 38(2): 185–195.

Chiaradia M, Fontboté L, and Paladines A (2004) Metal sources in mineral deposits and crustal rocks of Ecuador (1 N–4 S): A lead isotope synthesis. *Economic Geology* 99(6): 1085–1106.

Chiaradia M, Konopelko D, Seltmann R, and Cliff RA (2006) Lead isotope variations across terrane boundaries of the Tien Shan and Chinese Altay. *Mineralium Deposita* 41(5): 411–428.

Chiaradia M, Vallance J, Fontboté L, Stein H, Schaltegger U, Coder J, Richards J, Villeneuve M, and Gendall I (2009) U-Pb, Re-Os, and ^{40}Ar/^{39}Ar geochronology of the Nambija Au skarn and Pangui porphyry-Cu deposits, Ecuador: Implications for the Jurassic metallogenetic belt of the Northern Andes. *Mineralium Deposita* 44: 371–387.

Chiaradia M, Schaltegger U, Spikings R, Wotzlaw JF, and Ovtcharova M (2013) How accurately can we date the duration of magmatic-hydrothermal events in porphyry systems?—An invited paper. *Economic Geology* 108: 565–584.

Chiaradia M, Schaltegger U, and Spikings R (2014) *Time Scales of Mineral Systems—Advances in Understanding Over the Past Decade*. SEG Special Publication 18, pp. 37–58.

Chiaradia M, Pujol-Solà N, Farré-de-Pablo J, Aiuppa A, Paonita A, Rizzo AL, and Brusca L (2018) Geochemistry and isotope composition (Sr, Pb, δ66Zn) of Vulcano fumaroles (Aeolian Islands, Italy). *Chemical Geology* 493: 153–171.

Chiaradia M, Müntener O, and Beate B (2020) Effects of aseismic ridge subduction on the geochemistry of frontal arc magmas. *Earth and Planetary Science Letters* 531: 115984.

Chiaradia M, Bellver-Baca MT, Valverde V, and Spikings R (2021) Geochemical and isotopic variations in a frontal arc volcanic cluster (Chachimbiro-Pulumbura-Pilavo-Yanaurcu, Ecuador). *Chemical Geology* 574: 120240.

Childress TM, Simon AC, Day WC, Lundstrom CC, and Bindeman IN (2016) Iron and oxygen isotope signatures of the Pea Ridge and Pilot Knob magnetite-apatite deposits, southeast Missouri, USA. *Economic Geology* 111(8): 2033–2044.

Childress T, Simon AC, Reich M, Barra F, Bilenker LD, La Cruz NL, Bindeman IN, and Ovalle JT (2020a) Triple Oxygen (δ^{18}O, Δ^{17}O), hydrogen (δ^{2}H), and Iron (δ^{56}Fe) stable isotope signatures indicate a silicate magma source and magmatic-hydrothermal genesis for magnetite orebodies at El Laco, Chile. *Economic Geology* 115(7): 1519–1536.

Childress TM, Simon AC, Reich M, Barra F, Arce M, Lundstrom CC, and Bindeman IN (2020b) Formation of the Mantoverde iron oxide-copper-gold (IOCG) deposit, Chile: Insights from Fe and O stable isotopes and comparisons with iron oxide-apatite (IOA) deposits. *Mineralium Deposita* 55(7): 1489–1504.

Christensen JN, Halliday AN, Leigh KE, Randell RN, and Kesler SE (1997) Direct dating of sulfides by Rb-Sr: A critical test using the Polaris Mississippi Valley-type Zn-Pb deposit. *Geochimica et Cosmochimica Acta* 59: 5191–5197.

Condon D, Mathur R, Simpson T and Mendoza N (2012) *Cu Isotope Fractionation Used to Determine Supergene Processes at Yanacocha Mine in Northern Peru*. Geological Society of America Abstracts with Programs, vol. 46, No. 2.

Cooke DR and Simmons SF (2000) Characteristics and genesis of epithermal gold deposits. *Reviews in Economic Geology* 13: 221–244.

Courtney-Davies L, Ciobanu CL, Verdugo-Ihl MR, Dmitrijeva M, Cook NJ, Ehrig K, and Wade BP (2019) Hematite geochemistry and geochronology resolve genetic and temporal links among iron-oxide copper gold systems, Olympic Dam district, South Australia. *Precambrian Research* 335: 105480.

Coplen TB, De Bièvre P, Krouse HR, Vocke RD Jr, Gröning M, and Rozanski K (1996) Ratios for light-element isotopes standardized for better interlaboratory comparison. *Eos, Transactions American Geophysical Union* 77(27). 255–255.

Courtney-Davies L, Ciobanu CL, Tapster SR, Cook NJ, Ehrig K, Crowley JL, Verdugo-Ihl MR, Wade BP, and Condon DJ (2020) Opening the magmatic-hydrothermal window: High-precision U-Pb geochronology of the Mesoproterozoic Olympic Dam Cu-U-Au-Ag deposit, South Australia. *Economic Geology* 115: 1855–1870.

Crowley QG, Heron K, Riggs N, Kamber B, Chew D, McConnell B, and Benn K (2014) Chemical abrasion applied to LA-ICP-MS U–Pb zircon geochronology. *Minerals* 4(2): 503–518.

Cumming GL and Richards JR (1975) Ore lead isotope ratios in a continuously changing Earth. *Earth and Planetary Science Letters* 28: 155–171.

Dalrymple GB and Lanphere MA (1974) ^{40}Ar/^{39}Ar age spectra of some undisturbed terrestrial samples. *Geochimica et Cosmochimica Acta* 38(5): 715–738.

Dauphas N, Hopp T, Craig G, Zhang ZJ, Valdes MC, Heck PR, Charlier BLA, Bell EA, Harrison TM, Davis AM, Dussubieux L, Williams PR, Krawczynski MJ, Bouman C, Lloyd NS, Tollstrup D, and Schwieters JB (2022) In situ ^{87}Rb–^{87}Sr analyses of terrestrial and extraterrestrial samples by LA-MC-ICP-MS/MS with double Wien filter and collision cell technologies. *Journal of Analytical Atomic Spectrometry*. https://doi.org/10.1039/d2ja00135g.

de Ronde CEJ, Hannington MD, Stoffers P, Wright IC, Ditchburn RG, Reyes AG, Baker ET, Massoth GJ, Lupton JE, Walker SL, Greene RR, Soong CWR, Ishibashi J, Lebon GT, Bray CJ, and Resing JA (2005) Evolution of a submarine magmatic-hydrothermal system: Brothers Volcano, Southern Kermadec Arc, New Zealand. *Economic Geology* 100(6): 1097–1133.

de Ronde CEJ, Massoth GJ, Butterfield DA, et al. (2011) Submarine hydrothermal activity and gold-rich mineralization at Brothers Volcano, Kermadec Arc, New Zealand. *Mineralium Deposita* 46: 541–584.

Dekov VM, Rouxel O, Asael D, Hålenius U, and Munnik F (2013) Native Cu from the oceanic crust: Isotopic insights into native metal origin. *Chemical Geology* 359: 136–149.

Deloule E, Allegre CJ, and Doe BR (1986) Lead and sulfur isotope microstratigraphy in galena crystals from Mississippi Valley-type deposits. *Economic Geology* 81(6): 1307–1321.

Dendas M (2011) *Copper Isotopes Tracers of Fluid Flow at Bingham Canyon, Utah.* MSc Thesis, University of Arizona. 36 p.

Dennis PF, Myhill DJ, Marca A, and Kirk R (2019) Clumped isotope evidence for episodic, rapid flow of fluids in a mineralized fault system in the Peak District, UK. *Journal of the Geological Society* 176(3): 447–461.

Dewaele S, Muchez P, Vets J, Fernandez-Alonzo M, and Tack L (2006) Multiphase origin of the Cu-Co ore deposits in the western part of the Lufilian fold-and-thrust belt Katanga (Democratic Republic of Congo). *Journal of African Earth Sciences* 46: 455–469.

Dickin AP (2005) *Radiogenic Isotope Geology*, 2nd edn. Cambridge. 492 pp.

Dodson MH (1973) Closure temperature in cooling geochronological and petrological systems. *Contributions to Mineralogy and Petrology* 40: 259–274.

Dótor-Almazán A, Armienta-Hernández MA, Talavera-Mendoza O, and Ruiz J (2017) Geochemical behavior of Cu and sulfur isotopes in the tropical mining region of Taxco, Guerrero (southern Mexico). *Chemical Geology* 471: 1–12.

Duan J, Tang J, Li Y, Liu S-A, Wang Q, Yang C, and Wang Y (2016a) Copper isotopic signature of the Tiegelongnan high-sulfidation copper deposit, Tibet: Implications for its origin and mineral exploration. *Mineralium Deposita* 51(5): 591–602.

Duan J, Tang J, and Lin B (2016b) Zinc and lead isotope signatures of the Zhaxikang PbZn deposit, South Tibet: Implications for the source of the ore-forming metals. *Ore Geology Reviews* 78: 58–68.

Ducher M, Blanchard M, and Balan E (2018) Equilibrium isotopic fractionation between aqueous Zn and minerals from first-principles calculations. *Chemical Geology* 483: 342–350.

Eichhorn R, Höll R, Jagout E, and Schärer U (1997) Dating scheelite stages: A strontium, neodymium, lead approach from the Felhertal tungsten deposit, Central Alps, Austria. *Geochimica et Cosmochimica Acta* 61: 5005–5022.

Eiler JM (2007) "Clumped-isotope" geochemistry—The study of naturally-occurring, multiply-substituted isotopologues. *Earth and Planetary Science Letters* 262(3-4): 309–327.

El Desouky HA, Muchez P, and Cailteux J (2009) Two Cu–Co sulfide phases and contrasting fluid systems in the Katanga Copperbelt, Democratic Republic of Congo. *Ore Geology Reviews* 36(4): 315–332.

El Desouky HA, Muchez P, Boyce AJ, Schneider J, Cailteux JL, Dewaele S, and von Quadt A (2010) Genesis of sediment-hosted stratiform copper–cobalt mineralization at Luiswishi and Kamoto, Katanga Copperbelt (Democratic Republic of Congo). *Mineralium Deposita* 45: 735–763.

Fariña AO, Peacock CL, Fiol S, Antelo J, and Carvin B (2018) A universal adsorption behaviour for Cu uptake by iron (hydr)oxide organo-mineral composites. *Chemical Geology* 479: 22–35.

Farquhar J, Bao H, and Thiemens M (2000) Atmospheric influence of Earth's earliest sulfur cycle. *Science* 289(5480): 756–758.

Faure G and Mensing TM (2005) *Isotopes: Principles and Applications*. Hoboken: Wiley. 897 pp.

Fekiacova Z, Cornu S, and Pichat S (2015) Tracing contamination sources in soils with Cu and Zn isotopic ratios. *Science of the Total Environment* 517: 96–105.

Field CW and Gustafson LB (1976) Sulfur isotopes in the porphyry copper deposit at El Salvador, Chile. *Economic Geology* 71: 1533–1548.

Field CW, Zhang L, Dilles JH, Rye RO, and Reed MH (2005) Sulfur and oxygen isotopic record in sulfate and sulfide minerals of early, deep, pre-main stage porphyry Cu–Mo and late main stage base-metal mineral deposits, Butte district, Montana. *Chemical Geology* 215: 61–93.

Fielding IOH, Johnson SP, Zi J-W, Rasmussen B, Muhling JR, Dunkley DJ, Sheppard S, Wingate MTD, and Rogers JR (2017) Using in Situ SHRIMP U-Pb monazite and xenotime geochronology to determine the age of orogenic gold mineralization: An example from the Paulsens Mine, Southern Pilbara Craton. *Economic Geology* 112: 1205–1230.

Frei R and Kamber BS (1995) Single mineral Pb-Pb dating. *Earth and Planetary Science Letters* 129: 261–268.

Frimmel HE (2005) Archaean atmospheric evolution: Evidence from the Witwatersrand gold fields, South Africa. *Earth-Science Reviews* 70: 1–46.

Fujii T, Moynier F, Pons M-L, and Albarède F (2011) The origin of Zn isotope fractionation in sulfides. *Geochimica et Cosmochimica Acta* 75(23): 7632–7643.

Fujii T, Moynier F, Abe M, Nemoto K, and Albarède F (2013) Copper isotope fractionation between aqueous compounds relevant to low temperature geochemistry and biology. *Geochimica et Cosmochimica Acta* 110: 29–44.

Gao Z, Zhu X, Sun J, Luo Z, Bao C, Tang C, and Ma J (2018) Spatial evolution of Zn-Fe-Pb isotopes of sphalerite within a single ore body: A case study from the Dongshengmiao ore deposit, Inner Mongolia, China. *Mineralium Deposita* 53(1): 55–65.

Gaynor SP, Ruiz M, and Schaltegger U (2022) The importance of high precision in the evaluation of U-Pb zircon age spectra. *Chemical Geology* 603: 120913.

Giggenbach WF (1997) The origin and evolution of fluids in magmatic-hydrothermal systems. In: Barnes HL (ed.) *Geochemistry of Hydrothermal Ore Deposits*, 3rd edn., pp. 737–795. John Wiley's and Sons.

Goldfarb RJ, Groves DI, and Gardoll S (2001) Orogenic gold and geologic time: A global synthesis. *Ore Geology Reviews* 18: 1–75.

Goldhaber MB (2003) Sulfur-rich sediments. In: Holland HD and Turekian KK (eds.) *Treatise on Geochemistry*, pp. 257–288. Oxford: Elsevier Pergamon.

Goldhaber MB and Kaplan IR (1974) The sulfur cycle. *The Sea: Marine Chemistry* 5: 569–655.

Graham S, Pearson N, Jackson S, Griffin W, and O'Reilly SY (2004) Tracing Cu and Fe from source to porphyry; in situ determination of Cu and Fe isotope ratios in sulfides from the Grasberg Cu-Au deposit. *Chemical Geology* 207(3–4): 147–169.

Grandia F, Asmerom Y, Getty S, Cardellach E, and Canals À (2000) Pb dating of MVT ore-stage calcite: Implications for fluid flow in a Mesozoic extensional basin from Iberian Peninsula. *Journal of Geochemical Exploration* 69: 377–380.

Gregory MJ and Mathur R (2017) Understanding copper isotope behavior in the high temperature magmatic-hydrothermal porphyry environment. *Geochemistry, Geophysics, Geosystems* 18(11): 4000–4015.

Guinoiseau D, Bouchez J, Gélabert A, Louvat P, Moreira-Turcq P, Filizola N, and Benedetti MF (2018) Fate of particulate copper and zinc isotopes at the Solimões-Negro river confluence, Amazon Basin, Brazil. *Chemical Geology* 489: 1–15.

Gulson BL (1986) *Lead Isotopes in Mineral Exploration*. Amsterdam: Elsevier. 245 p.

Guo H, Xia Y, Bai R, Zhang X, and Huang F (2020) Experiments on Cu-isotope fractionation between chlorine-bearing fluid and silicate magma: Implications for fluid exsolution and porphyry Cu deposits. *National Science Review* 7(8): 1319–1330.

Guo Z, Tian H-C, Liu Y, Peng X, Qin G, and Lv Y (2022) Copper isotopic fractionation during seafloor alteration: Insights from altered basalts in the Mariana and yap trenches. *Journal of Geophysical Research - Solid Earth* 127(1): e2021JB023597.

Haest M, Muchez P, Petit JCJ, and Vanhaecke F (2009) Cu isotope ratio variations in the Dikulushi Cu-Ag deposit, DRC: Of primary origin or induced by supergene reworking. *Economic Geology* 104(7): 1055–1064.

Hames W, Unger D, Saunders J, and Kamenov G (2009) Early Yellowstone hotspot magmatism and gold metallogeny. *Journal of Volcanology and Geothermal Research* 188: 214–224.

Harris C, Pronost JMJ, Ashwal LD, and Cawthorn RG (2005) Oxygen and hydrogen isotope stratigraphy of the Rustenburg layered suite, bushveld complex: Constraints on crustal contamination. *Journal of Petrology* 46: 579–601.

Hart SR, Shimizu N, and Sverjensky DA (1981) Lead isotope zoning in galena; an ion microprobe study of a galena crystal from the Buick Mine, Southeast Missouri. *Economic Geology* 76(7): 1873–1878.

Hedenquist JW (1987) Mineralization associated with volcanic-related hydrothermal systems in the Circum-Pacific basin. In: Horn MK (ed.) *Transactions of the Fourth Circum-Pacific Energy and Mineral Resources Conference*, pp. 513–524. Tulsa, Oklahoma: American Association of Petroleum Geologists. August, 1986, Singapore.

Hedenquist JW, Arribas AR, and Gonzalez-Urien E (2000) Exploration for epithermal gold deposits. *Reviews in Economic Geology* 13: 245–277.

Heimann A, Beard BL, and Johnson CM (2008) The role of volatile exsolution and sub-solidus fluid/rock interactions in producing high ^{56}Fe/^{54}Fe ratios in siliceous igneous rocks. *Geochimica et Cosmochimica Acta* 72(17): 4379–4396.

Heinrich CA (2015) Witwatersrand gold deposits formed by volcanic rain, anoxic rivers and Archaean life. *Nature Geoscience* 8: 206–209.

Henry CD, Elson HB, McIntosh WC, Heizler MT, and Castor SB (1997) Brief duration of hydrothermal activity at Round Mountain, Nevada, determined from ^{40}Ar/^{39}Ar geochronology. *Economic Geology* 92: 807–826.

Hitzman MW and Broughton DW (2017) Discussion: "Age of the Zambian Copperbelt" by Sillitoe et al.(2017) Mineralium Deposita. *Mineralium Deposita* 52(8): 1273–1275.

Hitzman MW, Selley D, and Bull S (2010) Formation of sedimentary rock-hosted stratiform copper deposits through Earth history. *Economic Geology* 105(3): 627–639.

Hoefs J (2015) *Stable Isotope Geochemistry*, 7th edn, p. 389. Switzerland: Springer.

Holmes A (1946) An estimate of the age of the Earth. *Nature* 157(3995): 680–684.

Hou Q, Zhou L, Gao S, Zhang T, Feng L, and Yang L (2016) Use of Ga for mass bias correction for the accurate determination of copper isotope ratio in the NIST SRM 3114 Cu standard and geological samples by MC-ICPMS. *Journal of Analytical Atomic Spectrometry* 31(1): 280–287.

Houtermans FG (1946) Die Isotopenhäufigkeiten im natürlichen Blei und das Alter des Urans. *Naturwissenschaften* 33(6): 185–186.

Huang J, Liu S-A, Wörner G, Yu H, and Xiao Y (2016a) Copper isotope behavior during extreme magma differentiation and degassing: A case study on Laacher See phonolite tephra (East Eifel, Germany). *Contributions to Mineralogy and Petrology* 171(8): 76.

Huang J, Liu SA, Gao Y, Xiao Y, and Chen S (2016b) Copper and zinc isotope systematics of altered oceanic crust at IODP Site 1256 in the eastern equatorial Pacific. *Journal of Geophysical Research - Solid Earth* 121(10): 7086–7100.

Huston DL (1999) Stable isotopes and their significance for understanding the genesis of volcanic-hosted massive sulfide deposits: A review. *Reviews in Economic Geology* 10: 151–180.

Huston DL, Champion DC, Mernagh TP, Downes PM, Jones P, Carr G, Forster D, and David V (2016) Metallogenesis and geodynamics of the Lachlan Orogen: New (and old) insights from spatial and temporal variations in lead isotopes. *Ore Geology Reviews* 76: 257–267.

Ikehata K and Hirata T (2012) Copper isotope characteristics of copper-rich minerals from the Horoman peridotite complex, Hokkaido, Northern Japan. *Economic Geology* 107(7): 1489–1497.

Ikehata K, Notsu K, Hirata T, Navarrete JU, Borrok DM, Viveros M, and Ellzey JT (2011) Copper isotope characteristics of copper-rich minerals from Besshi-type volcanogenic massive sulfide deposits, Japan, determined using a femtosecond LA-MC-ICM-MS. *Economic Geology* 106(2): 307–316.

Jiang SY, Slack JF, and Palmer MR (2000) Sm-Nd dating of the giant Sullivan Pb-Zn-Ag deposit, British Columbia. *Geology* 28(8): 751–754.

John SG, Rouxel OJ, Craddock PR, Engwall AM, and Boyle EA (2008) Zinc stable isotopes in seafloor hydrothermal vent fluids and chimneys. *Earth and Planetary Science Letters* 269(1-2): 17–28.

Johnson CM, Beard BL, and Albarède F (2004) Geochemistry of non-traditional stable isotopes. *Reviews in Mineralogy and Geochemistry* 55. 454 pp.

Johnson C, Beard B, and Weyer S (2020) *Iron Geochemistry: An Isotopic Perspective*. Springer.

Kampunzu AB, Cailteux JLH, Kamona AF, Intiomale MM, and Melcher F (2009) Sediment-hosted Zn–Pb–Cu deposits in the central African copperbelt. *Ore Geology Reviews* 35(3-4): 263–297.

Kanasewich ER (1962) Approximate age of tectonic activity using anomalous lead isotopes. *Geophysical Journal of the Royal Astronomical Society* 7(2): 158–168.

Kanasewich ER and Farquhar RM (1965) Lead isotope ratios from the Cobalt–Noranda area, Canada. *Canadian Journal of Earth Sciences* 2(4): 361–384.

Kelley KD, Wilkinson JJ, Chapman JB, Crowther HL, and Weiss DJ (2009) Zinc isotopes in sphalerite from base metal deposits in the Red Dog district, Northern Alaska. *Economic Geology* 104(6): 767–773.

Kempton PD, Mathur R, Harmon RS, Bell A, Hoefs J, and Shaulis B (2022) Cu-isotope evidence for subduction modification of lithospheric mantle. *Geochemistry, Geophysics, Geosystems* 23(8): e2022GC010436.

Kendrick MA, Burgess R, Pattrick RAD, and Turner G (2001) Halogen and Ar-Ar age determinations of inclusions within quartz veins from porphyry copper deposits using complementary noble gas extraction techniques. *Chemical Geology* 177: 351–370.

Kesler SE, Jones LM, and Ruiz J (1988) Strontium isotopic geochemistry of Mississippi Valley-type deposits, East Tennessee: Implications for age and source of mineralizing brines. *Geological Society of America Bulletin* 100: 1300–1307.

Kesler SE, Cumming GL, Krstic D, and Appold MS (1994) Lead isotope geochemistry of Mississippi Valley-type deposits of the Southern Appalachians. *Economic Geology* 89: 307–321.

Kesler SE, Vennemann TW, Frederickson C, Breithaupt A, Vazquez R, and Furman FC (1997) Hydrogen and oxygen isotope evidence for origin of MVT-forming brines, Southern Appalachians. *Geochimica et Cosmochimica Acta* 61: 1513–1523.

Kidder JA, Voinot A, Sullivan KV, Chipley D, Valentino M, Layton-Matthews D, and Leybourne M (2020) Improved ion-exchange column chromatography for Cu purification from high-Na matrices and isotopic analysis by MC-ICPMS. *Journal of Analytical Atomic Spectrometry* 35(4): 776–783.

Kidder J, Voinot A, Leybourne M, Layton-Matthews D, and Bowell R (2021) Using stable isotopes of Cu, Mo, S, and $^{87}Sr/^{86}Sr$ in hydrogeochemical mineral exploration as tracers of porphyry and exotic copper deposits. *Applied Geochemistry* 128: 104935.

Kimball BE, Mathur R, Dohnalkova AC, Wall AJ, Runkel RL, and Brantley SL (2009) Copper isotope fractionation in acid mine drainage. *Geochimica et Cosmochimica Acta* 73(5): 1247–1263.

Knipping JL, Bilenker LD, Simon AC, Reich M, Barra F, Deditius AP, Lundstrom C, Bindeman I, and Munizaga R (2015a) Giant Kiruna-type deposits form by efficient flotation of magmatic magnetite suspensions. *Geology* 43(7): 591–594.

Knipping JL, Bilenker LD, Simon AC, Reich M, Barra F, Deditius AP, Wälle M, Heinrich CA, Holtz F, and Munizaga R (2015b) Trace elements in magnetite from massive iron oxide-apatite deposits indicate a combined formation by igneous and magmatic-hydrothermal processes. *Geochimica et Cosmochimica Acta* 171: 15–38.

Knipping JL, Fiege A, Simon AC, Oeser M, Reich M, and Bilenker LD (2019) In-situ iron isotope analyses reveal igneous and magmatic-hydrothermal growth of magnetite at the Los Colorados Kiruna-type iron oxide-apatite deposit, Chile. *American Mineralogist: Journal of Earth and Planetary Materials* 104(4): 471–484.

Kouzmanov K and Pokrovski G (2012) Hydrothermal controls on metal distribution in porphyry Cu (-Mo-Au) systems. *Geology and Genesis of Major Copper Deposits and Districts of the World: A Tribute to Richard H. Sillitoe.* Hedenquist J, Harris M, and Camus F (eds.). *Special Publications of the Society of Economic Geologists.* , 16, pp. 573–618. Littleton, CO: SEG.

Kramers JD and Tolstikhin IN (1997) Two terrestrial lead isotope paradoxes, forward transport modelling, core formation and the history of the continental crust. *Chemical Geology* 139(1-4): 75–110.

Krogh TE (1982) Improved accuracy of U-Pb zircon ages by the creation of more concordant systems using an air abrasion technique. *Geochimica et Cosmochimica Acta* 46(4): 637–649.

Kruger FJ (1994) The Sr-isotope stratigraphy of the Western Bushveld Complex. *South African Journal of Geology* 97: 393–398.

Kruger FJ and Marsh JS (1982) The significance of $^{87}Sr/^{86}Sr$ ratios in the Merensky cycle of the bushveld complex. *Nature* 298: 53–55.

Kuhlemann J, Vennemann TW, Herlec U, Zeeh S, and Bechstädt T (2001) Variations of sulfur isotopes, trace element compositions and cathodoluminescence of Mississippi Valley-type Pb-Zn ores from the Drau Range, Eastern Alps (Slovenia-Austria): Implications for ore deposition on a regional versus micro-scale. *Economic Geology* 96: 1931–1941.

Kurtz AC, Kay SM, Charrier R, and Farrar E (1997) Geochronology of Miocene plutons and exhumation history of the El Teniente region, Central Chile (34-35 8). *Andean Geology* 24(1): 75–90.

Kusonwiriyawong C, Bigalke M, Abgottspon F, Lazarov M, Schuth S, Weyer S, and Wilcke W (2017) Isotopic variation of dissolved and colloidal iron and copper in a carbonatic floodplain soil after experimental flooding. *Chemical Geology* 459: 13–23.

Lambert DD, Foster JG, and Frick LR (1999) Re-Os isotope geochemistry of magmatic sulfide ore systems. *Reviews in Economic Geology* 12: 29–57.

Lange S, Chaudhuri S, and Clauer N (1983) Strontium isotopic evidence for the origin of barites and sulfides from the Mississippi Valley-type ore deposits in southeast Missouri. *Economic Geology* 78(6): 1255–1261.

Large SJ, Buret Y, Wotzlaw JF, Karakas O, Guillong M, von Quadt A, and Heinrich CA (2021) Copper-mineralised porphyries sample the evolution of a large-volume silicic magma reservoir from rapid assembly to solidification. *Earth and Planetary Science Letters* 563: 116877.

Larner F, Rehkämper M, Coles BJ, Kreissig K, Weiss DJ, Sampson B, Unsworth C, and Strekopytov S (2011) A new separation procedure for Cu prior to stable isotope analysis by MC-ICP-MS. *Journal of Analytical Atomic Spectrometry* 26(8): 1627–1632.

Larson PB, Maher K, Ramos FC, Chang Z, Gaspar M, and Meinert LD (2003) Copper isotope ratios in magmatic and hydrothermal ore-forming environments. *Chemical Geology* 201(3-4): 337–350.

Leach DL, Sangster DF, Kelley KD, Large RR, Garven G, Allen CR, Gutzmer J and Walters S (2005) *Sediment-Hosted Lead–Zinc Deposits: A Global Perspective.* Economic Geology 100th Anniversary Volume, 561–607.

Leach DL, Bradley DC, Huston D, Pisarevsky SA, Taylor RD, and Gardoll SJ (2010) Sediment-hosted lead-zinc deposits in Earth history. *Economic Geology* 105(3): 593–625.

Lee JKW, Onstott TC, Cashman KV, Cumbest RJ, and Johnson D (1991) Incremental heating of hornblende in vacuo: Implications for ^{40}Ar/^{39}Ar geochronology and the interpretation of thermal histories. *Geology* 19(9): 872–876.

Li D and Liu S-A (2022) Copper Isotope Fractionation during Basalt Leaching at 25° C and pH = 0.3, 2. *Journal of Earth Science* 33(1): 82–91.

Li Q-L, Chen F, Yang J-H, and Fan H-R (2008) Single grain pyrite Rb-Sr dating of the Linglong gold deposit, eastern China. *Ore Geology Reviews* 34: 263–270.

Li W, Jackson SE, Pearson NJ, and Graham S (2010) Copper isotopic zonation in the Northparkes porphyry Cu-Au deposit, SE Australia. *Geochimica et Cosmochimica Acta* 74(14): 4078–4096.

Li Y, Selby D, Feely M, Costanzo A, and Li X-H (2017) Fluid inclusion characteristics and molybdenite Re-Os geochronology of the Qulong porphyry copper-molybdenum deposit, Tibet. *Mineralium Deposita* 52: 137–158.

Li Y, Li XH, Selby D, and Li JW (2018) Pulsed magmatic fluid release for the formation of porphyry deposits: Tracing fluid evolution in absolute time from the Tibetan Qulong Cu-Mo deposit. *Geology* 46(1): 7–10.

Li Y, Zhang RQ, He S, Chiaradia M, and Li XH (2022) Pulsed exsolution of magmatic ore-forming fluids in tin-tungsten systems: A SIMS cassiterite oxygen isotope record. *Mineralium Deposita* 57(3): 343–352.

Lide DR and Frederikse HPR (1995) *CRC Handbook of Chemistry and Physics*, 76th edn. Boca Raton, FL: CRC.

Little SH, Vance D, Walker-Brown C, and Landing WM (2014) The oceanic mass balance of copper and zinc isotopes, investigated by analysis of their inputs, and outputs to ferromanganese oxide sediments. *Geochimica et Cosmochimica Acta* 125: 673–693.

Liu S-A, Li D, Li S, Teng F-Z, Ke S, He Y, and Lu Y (2014a) High-precision copper and iron isotope analysis of igneous rock standards by MC-ICP-MS. *Journal of Analytical Atomic Spectrometry* 29(1): 122–133.

Liu S-A, Teng F-Z, Li S, Wei G-J, Ma J-L, and Li D (2014b) Copper and iron isotope fractionation during weathering and pedogenesis: Insights from saprolite profiles. *Geochimica et Cosmochimica Acta* 146: 59–75.

Liu Y, Qi L, Gao J, Ye L, Huang Z, and Zhou J (2015a) Re-Os dating of galena and sphalerite from lead-zinc sulfide deposits in Yunnan Province, SW China. *Journal of Earth Science* 26: 343–351.

Liu S-A, Huang J, Liu J, Wörner G, Yang W, Tang Y-J, Chen Y, Tang L, Zheng J, and Li S (2015b) Copper isotopic composition of the silicate Earth. *Earth and Planetary Science Letters* 427: 95–103.

Liu S, Li Y, Liu J, Yang Z, Liu J, and Shi Y (2021) Equilibrium Cu isotope fractionation in copper minerals: A first-principles study. *Chemical Geology* 564: 120060.

Liu J-H, Cheng J, Zhou L, Feng L-P, Hu Y-T, and Algeo TJ (2022) Copper and gallium isotopic behavior in highly weathered soils. *Chemical Geology* 594: 120757.

Luczaj J and Huang H (2018) Copper and sulfur isotope ratios in Paleozoic-hosted Mississippi Valley-type mineralization in Wisconsin, USA. *Applied Geochemistry* 89: 173–179.

Ludwig KR (2001) *Isoplot v. 2.2—A Geochronological Toolkit for Microsoft Excel.* Berkeley Geochronology Center. Special Publication 1a, 53 pp.

Macfarlane AW, Marcet P, LeHuray AP, and Petersen U (1990) Lead isotope provinces of the Central Andes inferred from ores and crustal rocks. *Economic Geology* 85(8): 1857–1880.

Maher KC (2005) *Analysis of Copper Isotope Ratios by Multi-Collector Inductively Coupled Plasma Mass Spectrometry and Interpretation of Copper Isotope Ratios From Copper Mineralization*. Washington State University.

Maher KC, Ramos FC, Larson PB, et al. (2003) Copper isotope characteristics of the Cu (+Au, Ag) skarn at Coroccohuayco, Peru. *Abstracts with Programs - Geological Society of America* 35(6): 518.

Maher KC, Jackson S, and Mountain B (2011) Experimental evaluation of the fluid–mineral fractionation of Cu isotopes at 250°C and 300°C. *Chemical Geology* 286(3-4): 229–239.

Maier WD, Arndt NT, and Curl EA (2000) Progressive crustal contamination of the Bushveld Complex: Evidence from Nd isotopic analyses of the cumulate rocks. *Contributions to Mineralogy and Petrology* 140: 316–327.

Malitch KN, Latypov RM, Badanina IY, and Sluzhenikin SF (2014) Insights into ore genesis of Ni-Cu-PGE sulfide deposits of the Noril'sk Province (Russia): Evidence from copper and sulfur isotopes. *Lithos* 204: 172–187.

Mamani M, Wörner G, and Sempere T (2010) Geochemical variations in igneous rocks of the Central Andean orocline (13 S to 18 S): Tracing crustal thickening and magma generation through time and space. *Geological Society of America Bulletin* 122(1-2): 162–182.

Marechal C and Albarede F (2002) Ion-exchange fractionation of copper and zinc isotopes. *Geochimica et Cosmochimica Acta* 66(9): 1499–1509.

Marechal CN, Telouk P, and Albarede F (1999) Precise analysis of copper and zinc isotopic compositions by plasma-source mass spectrometry. *Chemical Geology* 156(1-4): 251–273.

Maréchal CN, Nicolas E, Douchet C, and Albarède F (2000) Abundance of zinc isotopes as a marine biogeochemical tracer. *Geochemistry, Geophysics, Geosystems* 1(5).

Markey R, Hannah JL, Morgan JW, and Stein HJ (2003) A double spike for osmium analysis of highly radiogenic samples. *Chemical Geology* 200: 395–406.

Markl G, Lahaye Y, and Schwinn G (2006) Copper isotopes as monitors of redox processes in hydrothermal mineralization. *Geochimica et Cosmochimica Acta* 70(16): 4215–4228.

Marsh TM, Einaudi MT, and McWilliams M (1997) ^{40}Ar/^{39}Ar geochronology of Cu-Au and Au-Ag mineralization in the Potrerillos district, Chile. *Economic Geology* 92: 784–806.

Martin AJ, Keith M, Parvaz DB, McDonald I, Boyce AJ, McFall KA, et al. (2020) Effects of magmatic volatile influx in mafic VMS hydrothermal systems: Evidence from the Troodos ophiolite, Cyprus. *Chemical Geology* 531: 119325.

Mason TFD, Weiss DJ, Horstwood M, Parrish RR, Russell SS, Mullane E, and Coles BJ (2004) High-precision Cu and Zn isotope analysis by plasma source mass spectrometry Part 1. Spectral interferences and their correction. *Journal of Analytical Atomic Spectrometry* 19(2): 209–217.

Mason TFD, Weiss DJ, Chapman JB, Wilkinson JJ, Tessalina SG, Spiro B, Horstwood MSA, Spratt J, and Coles BJ (2005) Zn and Cu isotopic variability in the Alexandrinka volcanic-hosted massive sulphide (VHMS) ore deposit, Urals, Russia. *Chemical Geology* 221(3-4): 170–187.

Mathur R and Fantle MS (2015) Copper isotopic perspectives on supergene processes: Implications for the Global Cu cycle. *Elements* 11(5): 323–329.

Mathur R, Ruiz J, and Munizaga F (2000) Relationship between copper tonnage of Chilean base-metal porphyry deposits and Os isotope ratios. *Geology* 28(6): 555–558.

Mathur R, Ruiz J, Titley S, Liermann L, Buss H, and Brantley SL (2005) Cu isotopic fractionation in the supergene environment with and without bacteria. *Geochimica et Cosmochimica Acta* 69(22): 5233–5246.

Mathur R, Titley S, Barra F, Brantley S, Wilson M, Phillips A, Munizaga F, Maksaev V, Vervoort J, and Hart G (2009) Exploration potential of Cu isotope fractionation in porphyry copper deposits. *Journal of Geochemical Exploration* 102(1): 1–6.

Mathur R, Dendas M, Titley S, and Phillips A (2010) Patterns in the copper isotope composition of minerals in porphyry copper deposits in Southwestern United States. *Economic Geology* 105(8): 1457–1467.

Mathur R, Jin L, Prush V, Paul J, Ebersole C, Fornadel A, Williams JZ, and Brantley S (2012a) Cu isotopes and concentrations during weathering of black shale of the Marcellus Formation, Huntingdon County, Pennsylvania (USA). *Chemical Geology* 304–305: 175–184.

Mathur R, Ruiz J, Casselman MJ, Megaw P, and van Egmond R (2012b) Use of Cu isotopes to distinguish primary and secondary Cu mineralization in the Cañariaco Norte porphyry copper deposit, Northern Peru. *Mineralium Deposita* 47(7): 755–762.

Mathur R, Munk L, Nguyen M, Gregory M, Annell H, and Lang J (2013) Modern and paleofluid pathways revealed by Cu isotope compositions in surface waters and ores of the pebble porphyry Cu-Au-Mo deposit, Alaska. *Economic Geology* 108(3): 529–541.

Mathur R, Munk LA, Townley B, Gou KY, Gómez MN, Titley S, Chen GG, Song S, Reich M, Tornos F, and Ruiz J (2014) Tracing low-temperature aqueous metal migration in mineralized watersheds with Cu isotope fractionation. *Applied Geochemistry* 51: 109–115.

Mathur R, Falck H, Belogub E, Milton J, Wilson M, Rose A, and Powell W (2018) Origins of chalcocite defined by copper isotope values. *Geofluids* 2018: 9.

Matt P, Powell W, Mathur R, and deLorraine WF (2020) Zn-isotopic evidence for fluid-assisted ore remobilization at the Balmat Zinc Mine, NY. *Ore Geology Reviews* 116: 103227.

Matt P, Peck WH, Mathur R, Hurtgen MR, and Godfrey L (2022) Zinc Isotope Constraints on the Formation of Sedimentary Exhalative (SEDEX) ore deposits: New Evidence from the Franklin, NJ Mining District. *Ore Geology Reviews*: 104970.

Mattinson JM (2005) Zircon U-Pb chemical abrasion ("CA-TIMS") method: Combined annealing and multi-step partial dissolution analysis for improved precision and accuracy of zircon ages. *Chemical Geology* 220: 47–66.

McKibben MA and Hardie LA (1997) Ore-forming brines in active continental rifts. In: Barnes HL (ed.) *Geochemistry of Hydrothermal Ore Deposits*, 3rd edn., pp. 877–935. John Wiley's and Sons.

Merino ND (2009) *Petrology, geochemistry and geochronology of intrusive rocks from the Yanacocha gold district, Northern Peru (Unpublished MSc. Thesis)*, pp. 1–136. Switzerland: University of Geneva.

Mihaljevič M, Jarošíková A, Ettler V, Vaněk A, Penížek V, Křibek B, Chrastný V, Sracek O, Trubač J, Svoboda M, and Nyambe I (2018) Copper isotopic record in soils and tree rings near a copper smelter, Copperbelt, Zambia. *Science of the Total Environment* 621: 9–17.

Miliszkiewicz N, Walas S, and Tobiasz A (2015) Current approaches to calibration of LA-ICP-MS analysis. *Journal of Analytical Atomic Spectrometry* 30: 327–338.

Mirnejad H, Mathur R, Einali M, Dendas M, and Alirezaei S (2010) A comparative copper isotope study of porphyry copper deposits in Iran. *Geochemistry: Exploration, Environment, Analysis* 10(4): 413–418.

Mondillo N, Wilkinson JJ, Boni M, Weiss DJ, and Mathur R (2018) A global assessment of Zn isotope fractionation in secondary Zn minerals from sulfide and non-sulfide ore deposits and model for fractionation control. *Chemical Geology* 500: 182–193.

Morelli RM, Creaser RA, Seltmann R, Stuart FM, Selby D, and Graupner T (2007) Age and source constraints for the giant Muruntau gold deposit, Uzbekistan, from coupled Re-Os-He isotopes in arsenopyrite. *Geology* 35: 795–798.

Moynier F, Rushmer T, Albarede F, et al. (2005) Zn isotopic mass fractionation during high temperature segregation of metal from silicate. *Meteoritics & Planetary Science* 40(Suppl): A107.

Moynier F, Albarede F, and Herzog GF (2006) Isotopic composition of zinc, copper, and iron in lunar samples. *Geochimica et Cosmochimica Acta* 70(24): 6103–6117.

Moynier F, Vance D, Fujii T, and Savage P (2017) The isotope geochemistry of zinc and copper. *Reviews in Mineralogy and Geochemistry* 82(1): 543–600.

Muchez P, Brems D, Clara E, De Cleyn A, Lammens L, Boyce A, et al. (2010) Evolution of Cu–Co mineralizing fluids at Nkana mine, central African copperbelt, Zambia. *Journal of African Earth Sciences* 58(3): 457–474.

Muchez P, André-Mayer AS, El Desouky HA, and Reisberg L (2015) Diagenetic origin of the stratiform Cu–Co deposit at Kamoto in the Central African Copperbelt. *Mineralium Deposita* 50: 437–447.

Muchez P, André-Mayer AS, Dewaele S, and Large R (2017) Discussion: Age of the Zambian Copperbelt. *Mineralium Deposita* 52: 1269–1271.

Munhá J, Relvas JMRS, Barriga FJAS, Conceição P, Jorge RCGS, Mathur R, et al. (2005) Osmium isotope systematics in the Iberian Pyrite Belt. In: *Mineral Deposit Research: Meeting the Global Challenge*, pp. 663–666. Berlin, Heidelberg: Springer.

Nakai S, Halliday AN, Kesler SE, Jones HD, Kyle JR, and Lane TE (1993) Rb-Sr dating of sphalerites from Mississippi valley-type (MVT) ore deposits. *Geochimica et Cosmochimica Acta* 57: 417–427.

Navarrete JU, Borrok DM, Viveros M, and Ellzey JT (2011) Copper isotope fractionation during surface adsorption and intracellular incorporation by bacteria. *Geochimica et Cosmochimica Acta* 75(3): 784–799.

Neumann W and Huster E (1974) The half-life of ^{87}Rb measured as difference between the isotopes ^{87}Rb and ^{85}Rb. *Zeitschrift für Physik* 270: 121–127.

Nier AO (1940) A mass spectrometer for routine isotope abundance measurements. *Review of Scientific Instruments* 11(7): 212–216.

Nozaki T, Kato Y, and Suzuki K (2014) Re-Os geochronology of the Hitachi volcanogenic massive sulfide deposit: The Oldest Ore Deposit in Japan. *Economic Geology* 109: 2023–2034.

O'Neil JR (1986) Theoretical and experimental aspects of isotopic fractionation. In: Valley JW, Taylor HP Jr, and O'Neil JR (eds.) *Stable Isotopes in High Temperature Geological Processes. Reviews in Mineralogy*, vol. 16, pp. 1–40. Washington, DC: Mineralogical Society of America.

Ohmoto H (1986) Stable isotope geochemistry of ore deposits. In: Valley JW, Taylor HP Jr, and O'Neil JR (eds.) *Stable Isotopes in High Temperature Geological Processes. Reviews in Mineralogy*, vol. 16, pp. 491–559. Washington, DC: Mineralogical Society of America.

Ohmoto H and Goldhaber MB (1997) Sulfur and carbon isotopes. In: Barnes H (ed.) *Geochemistry of Hydrothermal Ore Deposits*, pp. 517–612. Wiley: New York, NY.

Orgeval JJ, Guerrot C, Tessalina SG, Bourdon B, Zaykov V, Buley C, et al. (2005) Lead isotopic systematics of Urals massive sulphide deposits. In: *Mineral Deposit Research: Meeting the Global Challenge*, pp. 667–670. Berlin, Heidelberg: Springer.

Otake T, Yamada R, Suzuki R, Nakamura S, Ito A, Shin K-C, and Sato T (2021) Large Fe isotope fractionations in sulfide ores and ferruginous sedimentary rocks from the Kuroko volcanogenic massive sulfide deposits in the Hokuroku district, northeast Japan. *Geochimica et Cosmochimica Acta* 295: 49–64.

Palacios C, Rouxel O, Reich M, Cameron E, and Leybourne M (2011) Pleistocene recycling of copper at a porphyry system, Atacama Desert, Chile: Cu isotope evidence. *Mineralium Deposita* 46(1): 1–7.

Pan H, Symons DTA, and Sangster DF (1990) Paleomagnetism of the Mississippi Valley-type ores and host rocks in the northern Arkansas and Tri-State districts. *Canadian Journal of Earth Sciences* 27(7): 923–931.

Patterson C (1956) Age of meteorites and the earth. *Geochimica et Cosmochimica Acta* 10(4): 230–237.

Peel K, Weiss D, Chapman J, Arnold T, and Coles B (2008) A simple combined sample-standard bracketing and inter-element correction procedure for accurate mass bias correction and precise Zn and Cu isotope ratio measurements. *Journal of Analytical Atomic Spectrometry* 23(1): 103–110.

Pękala M, Asael D, Butler IB, Matthews A, and Rickard D (2011) Experimental study of Cu isotope fractionation during the reaction of aqueous Cu(II) with Fe(II) sulphides at temperatures between 40 and 200°C. *Chemical Geology* 289(1): 31–38.

Pérez LJ (2012) *Chlorine and Strontium Isotopic Compositions of Magmatic Fluids Associated With Porphyry-Type Deposits: A Latitudinal Along-Arc Study of Porphyry Systems of the Chilean, Peruvian and Ecuadorian Andes*. Unpublished MSc Thesis, University of Geneva. 63 p.

Petit JC, De Jong J, Chou L, and Mattielli N (2008) Development of Cu and Zn isotope MC-ICP-MS measurements: Application to suspended particulate matter and sediments from the Scheldt estuary. *Geostandards and Geoanalytical Research* 32(2): 149–166.

Pettke T, Oberli F, and Heinrich CA (2010) The magma and metal source of giant porphyry-type ore deposits, based on lead isotope microanalysis of individual fluid inclusions. *Earth and Planetary Science Letters* 296(3-4): 267–277.

Piercey SJ (2011) The setting, style, and role of magmatism in the formation of volcanogenic massive sulfide deposits. *Mineralium Deposita* 46(5): 449–471.

Plumhoff AM, Mathur R, Milovský R, and Majzlan J (2021) Fractionation of the copper, oxygen and hydrogen isotopes between malachite and aqueous phase. *Geochimica et Cosmochimica Acta* 300: 246–257.

Pokrovsky OS, Viers J, Emnova EE, Kompantseva EI, and Freydier R (2008) Copper isotope fractionation during its interaction with soil and aquatic microorganisms and metal oxy(hydr) oxides: Possible structural control. *Geochimica et Cosmochimica Acta* 72(7): 1742–1757.

Ponzevera E, Quétel CR, Berglund M, Taylor PDP, Evans P, Loss RD, and Fortunato G (2006) Mass Discrimination During MC-ICPMS Isotopic Ratio Measurements: Investigation by Means of Synthetic Isotopic Mixtures (IRMM-007 Series) and Application to the Calibration of Natural-Like Zinc Materials (Including IRMM-3702 and IRMM-651). *Journal of the American Society for Mass Spectrometry* 17(10): 1413–1428.

Potra A and Macfarlane AW (2014) Lead isotope studies of the Guerrero composite terrane, west-central Mexico: Implications for ore genesis. *Mineralium Deposita* 49(1): 101–117.

Potra A, Garmon WT, Samuelsen JR, Wulff A, and Pollock ED (2018) Lead isotope trends and metal sources in the Mississippi Valley-type districts from the mid-continent United States. *Journal of Geochemical Exploration* 192: 174–186.

Potter EG, Sharpe R, Girard I, Fayek M, Gammon P, Quirt D, and Robbins J (2015) Fe and Mg signatures of the bong uranium deposit, Thelon Basin, Nunavut. *Targeted Geoscience Initiative* 4: 52–60.

Qiu H-N and Jiang Y-D (2007) Sphalerite ^{40}Ar/^{39}Ar progressive crushing and stepwise heating techniques. *Earth and Planetary Science Letters* 256: 224–232.

Reed MH (1997) Hydrothermal alteration and its relationship to ore fluid composition. In: Barnes HL (ed.) *Geochemistry of Hydrothermal Ore Deposits*, 3rd edn., pp. 303–365. John Wiley's and Sons.

Reich M, Deditius A, Chryssoulis S, Li J-W, Ma C-Q, Parada MA, Barra F, and Mittermayr F (2013) Pyrite as a record of hydrothermal fluid evolution in a porphyry copper system: A SIMS/EMPA trace element study. *Geochimica et Cosmochimica Acta* 104: 42–62.

Reich M, Simon AC, Barra F, Palma G, Hou T, and Bilenker LD (2022) Formation of iron oxide–apatite deposits. *Nature Reviews Earth & Environment*: 1–18.

Relvas JM, Tassinari CC, Munhá J, and Barriga FJ (2001) Multiple sources for ore-forming fluids in the Neves Corvo VHMS Deposit of the Iberian Pyrite Belt (Portugal): Strontium, neodymium and lead isotope evidence. *Mineralium Deposita* 36(5): 416–427.

Renne PR, Mundil R, Balco G, Min K, and Ludwig KR (2010) Joint determination of ^{40}K decay constants and ^{40}Ar*/^{40}K for the Fish Canyon sanidine standard, and improved accuracy for ^{40}Ar/^{39}Ar geochronology. *Geochimica et Cosmochimica Acta* 74(18): 5349–5367.

Requia K, Stein H, Fonboté L, and Chiaradia M (2003) Re-Os and Pb- Pb geochronology in the Archean Salobo iron oxide copper-gold deposit, Carajás mineral province, northern Brazil. *Mineralium Deposita* 38: 727–738.

Richards JP and Noble SR (1998) Applications of radiogenic isotope systems to the timing and origin of hydrothermal processes. *Reviews in Economic Geology* 10: 195–233.

Richards JP, McCulloch MT, Chappell BW, and Kerrich R (1991) Sources of metals in the Porgera gold deposit, Papua New Guinea: Evidence from alteration, isotope, and noble metal geochemistry. *Geochimica et Cosmochimica Acta* 55: 565–580.

Ripley EM and Li C (2003) Sulfur isotope exchange and metal enrichment in the formation of magmatic Cu-Ni-(PGE) deposits. *Economic Geology* 98(3): 635–641.

Ripley EM, Dong S, Li C, and Wasylenki LE (2015) Cu isotope variations between conduit and sheet-style Ni–Cu–PGE sulfide mineralization in the Midcontinent Rift System, North America. *Chemical Geology* 414: 59–68.

Rodriguez-Mustafa MA, Simon AC, Bilenker LD, Bindeman I, Mathur R, and Machado EL (2022) The Mina Justa Iron Oxide Copper-Gold (IOCG) Deposit, Peru: Constraints on metal and ore fluid sources. *Economic Geology* 117(3): 645–666.

Rottier B (2017) *Magmatic and Hydrothermal Fluid Processes at the Origin of the Giant Porphyry-Related Epithermal Polymetallic Deposit of Cerro de Pasco (Central Peru)*. PhD Thesis, University of Geneva. 431 p. http://archive-ouverte.unige.ch/unige:95569.

Rouxel O, Fouquet Y, and Ludden JN (2004) Copper isotope systematics of the lucky strike, rainbow, and Logatchev sea-floor hydrothermal fields on the mid-Atlantic ridge. *Economic Geology* 99(3): 585–600.

Ruiz J and Mathur R (1999) Metallogenesis in continental margins: Re-Os evidence from porphyry copper deposits in Chile. *Reviews in Economic Geology* 12: 59–72.

Ruiz J, Kesler SE, and Jones LM (1985) Strontium isotope geochemistry of fluorite mineralization associated with fluorine-rich igneous rocks from the Sierra Madre Occidental, Mexico; possible exploration significance. *Economic Geology* 80(1): 33–42.

Rutherford E and Soddy F (1902a) The cause and nature of radioactivity.–Part I. *Philosophical Magazine* 4(Ser 6): 370–396.

Rutherford E and Soddy F (1902b) The cause and nature of radioactivity.–Part II. *Philos Mag* 4(Ser 6): 569–585.

Rye RO (2005) A review of the stable-isotope geochemistry of sulfate minerals in selected igneous environments and related hydrothermal systems. *Chemical Geology* 215: 5–36.

Saintilan NJ, Selby D, Creaser RA, et al. (2018) Sulphide Re-Os geochronology links orogenesis, salt and Cu-Co ores in the Central African Copperbelt. *Scientific Reports* 8: 14946.

Saintilan NJ, Sproson AD, Selby D, Rottier B, Casanova V, Creaser RA, et al. (2021) Osmium isotopic constraints on sulphide formation in the epithermal environment of magmatic-hydrothermal mineral deposits. *Chemical Geology* 564: 120053.

Saunders JA, Mathur R, Kamenov GD, Shimizu T, and Brueseke ME (2015) New isotopic evidence bearing on bonanza (Au-Ag) epithermal ore-forming processes. *Mineralium Deposita* 51(1): 1–11.

Savag PS, Moynier F, Chen H, Shofner G, Siebert J, Badro J, and Puchtel I (2015) Copper isotope evidence for large-scale sulphide fractionation during Earth's differentiation. *Geochemical Perspectives Letters* 1. https://doi.org/10.7185/geochemlet.1506.

Schaltegger U (2007) Hydrothermal zircon. *Elements* 3(1): 51–79.

Schauble EA, Ghosh P, and Eiler JM (2006) Preferential formation of ^{13}C–^{18}O bonds in carbonate minerals, estimated using first-principles lattice dynamics. *Geochimica et Cosmochimica Acta* 70(10): 2510–2529.

Schauble E, Meheut M, and Hill PS (2009) Combining metal stable isotope fractionation theory with experiments. *Elements* 5: 369–374.

Schirra M and Laurent O (2021) Petrochronology of hydrothermal rutile in mineralized porphyry Cu systems. *Chemical Geology* 581: 120407.

Schmandt D, Broughton D, Hitzman MW, Plink-Bjorklund P, Edwards D, and Humphrey J (2013) The Kamoa copper deposit, Democratic Republic of Congo: Stratigraphy, diagenetic and hydrothermal alteration, and mineralization. *Economic Geology* 108(6): 1301–1324.

Schoene B, Crowley JL, Condon DJ, Schmitz MD, and Bowring SA (2006) Reassessing the uranium decay constants for geochronology using ID-TIMS U–Pb data. *Geochimica et Cosmochimica Acta* 70(2): 426–445.

Scott SD (1997) Submarine hydrothermal systems and deposits. In: Barnes HL (ed.) *Geochemistry of Hydrothermal Ore Deposits*, 3rd edn., pp. 797–875. John Wiley's and Sons.

Seal RRII (2006) Sulfur isotope geochemistry of sulfide minerals. *Reviews in Mineralogy and Geochemistry* 61: 633–677.

Seal RRII, Alpers CN, and Rye RO (2000) Stable isotope systematics of sulfate minerals. *Reviews in Mineralogy and Geochemistry* 40: 541–602.

Selby D, Creaser RA, Stein HJ, Markey RJ, and Hannah JL (2007) Assessment of the 187Re decay constant by cross calibration of Re–Os molybdenite and U–Pb zircon chronometers in magmatic ore systems. *Geochimica et Cosmochimica Acta* 71(8): 1999–2013.

Seo JH, Lee SK, and Lee I (2007) Quantum chemical calculations of equilibrium copper (I) isotope fractionations in ore-forming fluids. *Chemical Geology* 243(3-4): 225–237.

Seward TM and Barnes HL (1997) Metal transport by hydrothermal ore fluids. In: Barnes HL (ed.) *Geochemistry of Hydrothermal Ore Deposits*, 3rd edn., pp. 435–485. John Wiley's and Sons.

Shanks WC III (2001) Stable isotopes in seafloor hydrothermal systems: Vent fluids, hydrothermal deposits, hydrothermal alteration, and microbial processes. *Reviews in Mineralogy and Geochemistry* 43(1): 469–525.

Shanks WC III (2014) Stable isotope geochemistry of mineral deposits. In: *Treatise on Geochemistry*, 2nd edn, vol. 13, pp. 59–85. Netherlands: Amsterdam.

Sharp ZD (2017) *Principles of Stable Isotope Geochemistry*, p. 344. Upper Saddle River, NJ: Pearson Prentiss Hall.

Sheppard SMF (1986) Characterization and isotopic variations in natural waters. In: Valley J. W., O'Neil J. W., and Taylor H. P. Jr. (eds.) Stable Isotopes in High Temperature Geological Processes. Washington, DC: Mineralogical Society of America. *Reviews in Mineralogy* 16: 165–184.

Shields W, Goldich S, Garner E, and Murphy T (1965) Natural variations in the abundance ratio and the atomic weight of copper. *Journal of Geophysical Research* 70(2): 479–491.

Sillitoe RH (2010) Porphyry copper systems. *Economic Geology* 105: 3–41.

Sillitoe RH and Hart SR (1984) Lead-isotopic signatures of porphyry copper deposits in oceanic and continental settings, Colombian Andes. *Geochimica et Cosmochimica Acta* 48(10): 2135–2142.

Sillitoe RH, Hannington MD, and Thompson JFH (1996) High-sulfidation deposits in the volcanogenic massive sulfide environment. *Economic Geology* 91: 204–212.

Sillitoe RH, Perelló J, Creaser RA, Wilton J, Wilson AJ, and Dawborn T (2017) Age of the Zambian Copperbelt. *Mineralium Deposita* 52(8): 1245–1268.

Simon J, Jordan M, Tappa M, Schauble E, Kohl I, and Young E (2017) Calcium and titanium isotope fractionation in refractory inclusions: Tracers of condensation and inheritance in the early solar protoplanetary disk. *Earth and Planetary Science Letters* 472: 277–288.

Skinner BJ (1997) Hydrothermal mineral deposits: What we do and don't know. In: Barnes HL (ed.) *Geochemistry of Hydrothermal Ore Deposits*, 3rd edn., pp. 1–29. John Wiley's and Sons.

Smith PE, Evensen NM, York D, Szatmari P, and de Oliveira DC (2001) Single-crystal ^{40}Ar-^{39}Ar dating of pyrite: No fool's clock. *Geology* 29: 403–406.

Smith JM, Ripley EM, Li C, and Wasylenki LE (2022) Cu and Ni isotope variations of country rock-hosted massive sulfides located near midcontinent rift intrusions. *Economic Geology* 117(1): 195–211.

Smoliar MI, Walker RJ, and Morgan JW (1996) Re-Os ages of group IIA, IIIA, IVA, and IVB iron meteorites. *Science* 271(5252): 1099–1102.

Song S, Mathur R, Ruiz J, Chen D, Allin N, Guo K, and Kang W (2016) Fingerprinting two metal contaminants in streams with Cu isotopes near the Dexing Mine, China. *Science of the Total Environment* 544: 677–685.

Sossi PA, Halverson GP, Nebel O, and Eggins SM (2015) Combined separation of Cu, Fe and Zn from rock matrices and improved analytical protocols for stable isotope determination. *Geostandards and Geoanalytical Research* 39(2): 129–149.

Spry PG, Mathur RD, Teale GS, and Godfrey LV (2022) Zinc, sulfur and cadmium isotopes and Zn/Cd ratios as indicators of the origin of the supergiant Broken Hill Pb–Zn–Ag deposit and other Broken Hill-type deposits, New South Wales, Australia. *Geological Magazine* 159: 1–22.

Stacey JS and Kramers JD (1975) Approximation of terrestrial lead isotope evolution by a two-stage model. *Earth and Planetary Science Letters* 26: 207–221.

Steiger RH and Jaeger E (1977) Sub-commission on Geochronology: Convention on the use of decay constants in geo-and cosmochronology. *Earth and Planetary Science Letters* 36(3): 359–362.

Stein HJ, Morgan JW, and Scherstén A (2000) Re-Os dating of low-level highly radiogenic (LLHR) sulfides: The Harnas gold deposit, southwest Sweden, records continental-scale tectonic events. *Economic Geology* 95(8): 1657–1671.

Stein HJ, Markey RJ, Morgan JW, Hannah JL, and Scherstén A (2001) The remarkable Re-Os chronometer in molybdenite: How and why it works. *Terra Nova* 13: 479–486.

Su J, Mathur R, Brumm G, D'Amico P, Godfrey L, Ruiz J, and Song S (2018) Tracing copper migration in the Tongling Area through copper isotope values in soils and waters. *International Journal of Environmental Research and Public Health* 15.

Sullivan K, Layton-Matthews D, Leybourne M, Kidder J, Mester Z, and Yang L (2020) Copper isotopic analysis in geological and biological reference materials by MC-ICP-MS. *Geostandards and Geoanalytical Research* 44(2): 349–362.

Sylvester PJ (2008) LA-(MC)-ICP-MS trends in 2006 and 2007 with particular emphasis on measurement uncertainties. *Geostandards and Geoanalytical Research* 32: 469–488.

Syverson DD, Borrok DM, Niebuhr S, and Seyfried WE (2021) Chalcopyrite-dissolved Cu isotope exchange at hydrothermal conditions: Experimental constraints at 350°C and 50 MPa. *Geochimica et Cosmochimica Acta* 298: 191–206.

Tan Q, Xia Y, Xie Z, Wang Z, Wei D, Zhao Y, Yan J, and Li S (2019) Two Hydrothermal Events at the Shuiyindong Carlin-Type Gold Deposit in Southwestern China: Insight from Sm-Nd Dating of Fluorite and Calcite. *Minerals* 9: 230.

Tang D, Qin K, Su B, Mao Y, Evans NJ, Niu Y, and Kang Z (2020) Sulfur and copper isotopic signatures of chalcopyrite at Kalatongke and Baishiquan: Insights into the origin of magmatic Ni-Cu sulfide deposits. *Geochimica et Cosmochimica Acta* 275: 209–228.

Tardani D, Reich M, Deditius AP, Chryssoulis S, Sánchez-Alfaro P, Wrage J, and Roberts MP (2017) Copper–arsenic decoupling in an active geothermal system: A link between pyrite and fluid composition. *Geochimica et Cosmochimica Acta* 204: 179–204.

Tatsumoto M, Knight RJ, and Allegre CJ (1973) Time differences in the formation of meteorites as determined from the ratio of lead-207 to lead-206. *Science* 180(4092): 1279–1283.

Taylor BE (1987) Stable isotope geochemistry of ore-forming fluids. In: Kyser KT (ed.) *Stable Isotope Geochemistry of Low Temperature Processes, Short Course Notes*, pp. 337–445. Ottawa, ON: Mineralogical Association of Canada.

Taylor BE (2007) Epithermal gold deposits. In: *Mineral Deposits of Canada: A Synthesis of Major Deposit-Types, District Metallogeny, the Evolution of Geological Provinces, and Exploration Methods*, pp. 113–139. Geological Association of Canada, Mineral Deposits Division. Special Publication 5.

Taylor HP Jr (1974) The application of oxygen and hydrogen isotope studies to problems of hydrothermal alteration and ore deposition. *Economic Geology* 69: 843–883.

Taylor HP Jr (1997) Oxygen and hydrogen isotope relationships in hydrothermal mineral deposits. In: Barnes HL (ed.) *Geochemistry of Hydrothermal Ore Deposits*, 3rd edn., pp. 229–302. New York, NY: Wiley.

Thiemens MH and Lin M (2021) Discoveries of mass independent isotope effects in the solar system: Past, present and future. *Reviews in Mineralogy and Geochemistry* 86(1): 35–95.

Tilton GR, Pollak RJ, Clark AH, and Robertson RC (1981) Isotopic composition of Pb in central Andean ore deposits. *Geological Society of America Memoirs* 154: 791–816.

Tosdal RM and Munizaga F (2003) Lead sources in Mesozoic and Cenozoic Andean ore deposits, north-central Chile (30–34 S). *Mineralium Deposita* 38(2): 234–250.

Tosdal RM, Gibson PC, and Noble DC (1995) Metal Source for Miocene Precious-Metal Veins of the Orcopampa, Shila, Cailloma and Arcata Mining Districts, Southern Peru. In: *Volumen Jubilar Alberto Benavides*, pp. 311–326. Sociedad Geológica del Perú.

Tosdal RM, Wooden JL, and Bouse RM (1999) Pb isotopes, ore deposits, and metallogenetic terranes. *Reviews in Economic Geology* 12: 1–28.

Tretbar DR, Arehart GB, and Christensen JN (2000) Dating gold deposition in a Carlin-type gold deposit using Rb/Sr methods on the mineral galkhaite. *Geology* 28: 947–950.

Troll VR, Weis FA, Jonsson E, Andersson UB, Majidi SA, Högdahl K, Harris C, Millet MA, Chinnasamy SS, Kooijman E, and Nilsson KP (2019) Global Fe–O isotope correlation reveals magmatic origin of Kiruna-type apatite-iron-oxide ores. *Nature Communications* 10(1): 1712.

Tunnell BN, Locmelis M, Seeger C, Mathur R, Dunkl I, Sullivan B, and Lori L (2021) The Pilot Knob iron ore deposits in southeast Missouri, USA: A high-to-low temperature magmatic-hydrothermal continuum. *Ore Geology Reviews* 131: 103973.

Vallejo C, Winkler W, Spikings RA, Luzieux L, Heller F, and Bussy F (2009) Mode and timing of terrane accretion in the forearc of the Andes in Ecuador. In: Kay SM, Ramos VA, and Dickinson WR (eds.) *Backbone of the Americas: Shallow Subduction, Plateau Uplift, and Ridge and Terrane Collision*. https://doi.org/10.1130/2009.1204(09). Geological Society of America Memoir 204.

Vance D, Archer C, Bermin J, Perkins J, Statham PJ, Lohan MC, Ellwood MJ, and Mills RA (2008) The copper isotope geochemistry of rivers and the oceans. *Earth and Planetary Science Letters* 274(1–2): 204–213.

Vance D, Matthews A, Keech A, Archer C, Hudson G, Pett-Ridge J, and Chadwick OA (2016) The behaviour of Cu and Zn isotopes during soil development: Controls on the dissolved load of rivers. *Chemical Geology* 445: 36–53.

Vazquez R, Vennemann TW, Kesler SE, and Russell N (1998) Carbon and oxygen isotope halos in the host limestone, El Mochito Zn, Pb (Ag) skarn massive sulfide/oxide deposit, Honduras. *Economic Geology* 93: 15–31.

Veizer J, Laznicka P, and Jansen SL (1989) Mineralization through geologic time: Recycling perspective. *American Journal of Science* 289: 484–524.

Vennemann TW, Muntean JL, Kesler SE, O'Neil JR, Valley JW, and Russell N (1993) Stable isotope evidence for magmatic fluids in the Pueblo Viejo epithermal acid-sulfate Au-Ag deposit, Dominican Republic. *Economic Geology* 88: 55–71.

Vermeesch P (2018) IsoplotR: A free and open toolbox for geochronology. *Geoscience Frontiers* 9: 1479–1493.

Vielreicher NM, Groves DI, Fletcher IR, McNaughton NJ, and Rasmussen B (2003) Hydrothermal monazite and xenotime geochronology: A new direction for precise dating of orogenic gold mineralization. *SEG Newsletter* 53(1): 10–16.

Von Quadt A, Erni M, Martinek K, Moll M, Peytcheva I, and Heinrich CA (2011) Zircon crystallization and the lifetimes of ore-forming magmatic-hydrothermal systems. *Geology* 39: 731–734.

Wafforn S, Seman S, Kyle RJ, Stockli D, Leys C, Sonbait D, and Cloos M (2018) Andradite garnet U-Pb geochronology of the big Gossan skarn, Ertsberg-Grasberg mining district, Indonesia. *Economic Geology* 113: 769–778.

Wall A, Heaney P, Mathur R, Gammons C, and Brantley S (2010) Cu isotope systematics of the Butte Mining District, Montana. In: *Proceedings Geochimica et Cosmochimica Acta 74, Pergamon-Elsevier Science Ltd the Boulevard, Langford Lane, Kidlington, Oxford Ox5 1gb, England*, p. A1093.

Wall AJ, Heaney PJ, Mathur R, Post JE, Hanson JC, and Eng PJ (2011a) A flow-through reaction cell that couples time-resolved X-ray diffraction with stable isotope analysis. *Journal of Applied Crystallography* 44(2): 429–432.

Wall AJ, Mathur R, Post JE, and Heaney PJ (2011b) Cu isotope fractionation during bornite dissolution: An in situ X-ray diffraction analysis. *Ore Geology Reviews* 42(1): 62–70.

Wang Y, Zhu X-K, Mao J-W, Li Z-H, and Cheng Y-B (2011) Iron isotope fractionation during skarn-type metallogeny: A case study of Xinqiao Cu–S–Fe–Au deposit in the Middle–Lower Yangtze valley. *Ore Geology Reviews* 43(1): 194–202.

Wang Z, Zhang P, Li Y, Ishii T, Li W, Ishii T, Li W, Foley S, Wang X, Wang X, and Li M (2021a) Copper recycling and redox evolution through progressive stages of oceanic subduction: Insights from the Izu-Bonin-Mariana forearc. *Earth and Planetary Science Letters* 574: 117178.

Wang D, Zheng Y, Mathur R, Qiu K, Wu H, Ren H, Wang E, Li Y, and Yi J (2021b) Zinc and cadmium isotopic constraints on ore formation and mineral exploration in epithermal system: A reconnaissance study at the Keyue and Zhaxikang Sb–Pb–Zn–Ag deposits in southern Tibet. *Ore Geology Reviews* 139: 104594.

Watson JV (1978) Ore deposits through geological time. *Proceedings of the Royal Society of London Academy* 362: 305–328.

Wawryk CM and Foden JD (2017) Iron-isotope systematics from the Batu Hijau Cu-Au deposit, Sumbawa, Indonesia. *Chemical Geology* 466: 159–172.

Wei Y, Niu Y, Gong H, Duan M, Chen S, Guo P, and Sun P (2020) Geochemistry and iron isotope systematics of coexisting Fe-bearing minerals in magmatic FeTi deposits: A case study of the Damiao titanomagnetite ore deposit, North China Craton. *Gondwana Research* 81: 240–251.

Weis F (2013) *Oxygen and Iron Isotope Systematics of the Grängesberg Mining District (GMD), Central Sweden.* MSc thesis Advanced level, Uppsala University, Disciplinary Domain of Science and Technology, Earth Sciences, Department of Earth Sciences, Solid Earth Geology.

Weis P, Driesner T, and Heinrich CA (2012) Porphyry-copper ore shells form at stable pressure-temperature fronts within dynamic fluid plumes. *Science* 338: 1613–1616.

Wernicke RS and Lippolt HJ (1994) Dating of vein Specularite using internal (U+Th)/^{4}He isochrons. *Geophysical Research Letters* 21: 345–347.

Weyer S, Anbar AD, Brey GP, Muenker C, Mezger K, and Woodland AB (2005) Iron isotope fractionation during planetary differentiation. *Earth and Planetary Science Letters* 240(2): 251–264.

Whitehouse MJ, Schoenberg R, Fedo C, and Kamber B (2015) Does a heavy Fe-isotope composition of Akilia quartz-amphibole-pyroxene rocks necessitate a BIF origin? *Astrobiology* 15(10): 816–824.

Wilkinson J, Weiss D, Mason T, and Coles B (2005) Zinc isotope variation in hydrothermal systems: Preliminary evidence from the Irish Midlands ore field. *Economic Geology* 100(3): 583–590.

Wooden JL and Mueller PA (1988) Pb, Sr, and Nd isotopic compositions of a suite of Late Archean, igneous rocks, eastern Beartooth Mountains: Implications for crust-mantle evolution. *Earth and Planetary Science Letters* 87(1-2): 59–72.

Wooden JL, Stacey JS, Howard KA, Doe BR, and Miller DM (1988) Pb isotopic evidence for the formation of Proterozoic crust in the southwestern United States. In: *Metamorphism and Crustal Evolution of the Western United States*, pp. 69–86. Prentice-Hall.

Wooden JL, DeWitt E, and Karlstrom KE (1991) Pb isotopic evidence for the boundary between the early Proterozoic Mojave and central Arizona crustal provinces in western Arizona. *Arizona Geological Society Digest* 19: 27–50.

Wooden JL, Kistler RW, and Tosdal RM (1998) Pb isotopic mapping of crustal structure in the northern Great Basin and relationships to Au deposit trends. *U.S. Geological Survey Open-File Report* 98(338): 20–33.

Wu L-Y, Hu R-Z, Li X-F, Liu S-A, Tang Y-W, and Tang Y-Y (2017) Copper isotopic compositions of the Zijinshan high-sulfidation epithermal Cu–Au deposit, South China: Implications for deposit origin. *Ore Geology Reviews* 83: 191–199.

Wu C, Chen H, and Lu Y (2022) Crustal structure control on porphyry copper systems in accretionary orogens: Insights from Nd isotopic mapping in the Central Asian Orogenic Belt. *Mineralium Deposita* 57(4): 631–641.

Yang Z, Song W, Wen H, Zhang Y, Fan H, Wang F, Li Q, Yang T, Zhou Z, and Liao S (2022) Zinc, cadmium and sulphur isotopic compositions reveal biological activity during formation of a volcanic-hosted massive sulphide deposit. *Gondwana Research* 101: 103–113.

Yao J, Mathur R, Sun W, Song W, Chen H, Mutti L, Xiang X, and Luo X (2016) Fractionation of Cu and Mo isotopes caused by vapor-liquid partitioning, evidence from the Dahutang W-Cu-Mo ore field. *Geochemistry, Geophysics, Geosystems* 17(5): 1725–1739.

Yuan S, Peng J, Hao S, Li H, Geng J, and Zhang D (2011) In-situ LA-MC-ICP-MS and ID-TIMS U-Pb geochronology of cassiterite in the giant Furong tin deposit, Hunan Province, South China: New constraints on the timing of tin-polymetallic mineralization. *Ore Geology Reviews* 43: 235–242.

Yuan H, Yuan W, Bao Z, Chen K, Huang F, and Liu S (2017) Development of two new copper isotope standard solutions and their copper isotopic compositions. *Geostandards and Geoanalytical Research* 41(1): 77–84.

Zartman RE and Doe BR (1981) Plumbotectonics—The model. *Tectonophysics* 75: 135–162.

Zartman RE and Haines SM (1988) The plumbotectonic model for Pb isotopic systematics among major terrestrial reservoirs—A case for bi-directional transport. *Geochimica et Cosmochimica Acta* 52: 1327–1339.

Zentilli M, Doe BR, Hedge CE, Alverez O, Tidy E, and Daroca JA (1988) Isótopos de plomo en yacimientos de tipo pórfido cuprífero comparados con otros depósitos metalíferos en los Andes del norte de Chile y Argentina (English abstract). *Actas, V Congreso Geológico Chileno Santiago* 1: B331–B369.

Zhang Z, Xie G, Mao J, Liu W, Olin P, and Li W (2019) Sm-Nd Dating and In-Situ LA-ICP-MS Trace Element Analyses of Scheelite from the Longshan Sb-Au Deposit, Xiangzhong Metallogenetic Province, South China. *Minerals* 9: 87.

Zhang Y, Bao Z, Lv N, Chen K, Zong C, and Yuan H (2020) Copper isotope ratio measurements of Cu-dominated minerals without column chromatography using MC-ICP-MS. *Frontiers in Chemistry* 8: 609.

Zhao Y, Xue C, Liu S-A, Symons DTA, Zhao X, Yang Y, and Ke J (2017) Copper isotope fractionation during sulfide-magma differentiation in the Tulaergen magmatic Ni–Cu deposit, NW China. *Lithos* 286: 206–215.

Zhao Y, Xue C, Liu S-A, Mathur R, Zhao X, Yang Y, Dai J, Man R, and Liu X (2019) Redox reactions control Cu and Fe isotope fractionation in a magmatic Ni–Cu mineralization system. *Geochimica et Cosmochimica Acta* 249: 42–58.

Zhao H-X, Li B, Zhou Y-X, Zhu Z-Y, and Chen S-M (2022a) Genesis of the giant Zijinshan epithermal Cu-Au deposit, Fujian Province, southeastern China: Cu-He-Ar isotope perspective. *Ore Geology Reviews* 148: 105047.

Zhao Y, Liu S-A, Xue C, Mathur R, Symons DT, and Ke J (2022b) Copper isotope fractionation in magmatic Ni–Cu mineralization systems associated with the variation of oxygen fugacity in silicate magmas. *Geochimica et Cosmochimica Acta* 338: 250–263.

Zhou J-X, Huang Z-L, Zhou M-F, Zhu X-K, and Muchez P (2014) Zinc, sulfur and lead isotopic variations in carbonate-hosted Pb–Zn sulfide deposits, southwest China. *Ore Geology Reviews* 58: 41–54.

Zhou H, Sun X, Wu Z, Liao J, Fu Y, Li D, Hollings P, Liu Y, Lin H, and Lin Z (2017) Hematite U-Pb geochronometer: Insights from monazite and hematite integrated chronology of the Yaoan gold deposit, Southwest China. *Economic Geology* 112: 2023–2039.

Zhu XK, O'Nions RK, Guo Y, Belshaw NS, and Rickard D (2000) Determination of natural Cu-isotope variation by plasma-source mass spectrometry; implications for use as geochemical tracers. *Chemical Geology* 163(1-4): 139–149.

Zhu XK, Guo Y, Williams RJP, O'Nions RK, Matthews A, Belshaw NS, Canters GW, de Waal EC, Weser U, Burgess BK, and Salvato B (2002) Mass fractionation processes of transition metal isotopes. *Earth and Planetary Science Letters* 200(1-2): 47–62.